PROBING THE ELECTRONIC PROPERTIES OF INTRAMOLECULAR PROTON TRANSFER, TRIPLE RYDBERG ANIONS, AND STABLE RADICALS VIA ANION PHOTOELECTRON SPECTROSCOPY

by
Evan L. Collins

A dissertation submitted to Johns Hopkins University in conformity with the requirements for the degree of Doctor of Philosophy

Baltimore, Maryland

January, 2019

ABSTRACT

Negative ions were studied using gas-phase anion photoelectron spectroscopy. Combining these studies with theoretical calculations allowed for electronic properties, geometries, as well as chemical phenomena to be investigated. A system of triple Rydberg anions was discovered and studied. Intramolecular proton transfer was probed by extensive experimental and theoretical efforts, providing fundamental insights into the phenomena. Additionally, an electrospray ionization source was designed, constructed and integrated into the anion photoelectron spectrometer. This source creates a direct route for transferring species from the solution phase to the gas phase. This source was used to study stable radicals generated from radical scavengers.

Advisor: Dr. Kit Bowen

Readers: Dr. Art Bragg

Dr. Howard Fairbrother

ACKNOWLEDGMENTS

I would first like to thank my advisor Dr. Kit Bowen for the opportunity to work in his laboratory. I've learned a great deal about chemical physics and experimental science during my time in the lab. Working for Kit has made me a better critical thinker and a better scientist, which I will be always be grateful for.

Over the course of my time in the lab, I've had the opportunity to work with a group of competent and affable people, and I've truly enjoyed my time here.

Allyson Buytendyk is a great friend and was a mentor when I first joined the lab. Allyson was always willing to help and offer ideas and advice. Her skills as a problem solver and, almost more importantly, a voice of reason and thoughtful consideration are missed in the lab.

Jacob Graham is another great friend and mentor. Jacob is always interested in learning about a new topic. His infectious curiosity leads him and those around him to learn about a range of diverse subject areas.

I would like to thank Xin Tang for his friendship and all his help and advice over the course of graduate school. Xin always enthusiastically searched for inventive and clever solutions for a range of problems we encountered in the lab. Also, he was always up for an adventure both inside and outside the laboratory.

Colin Zhang is a focused scientist and has always had an inventive approach to chemical problems, I think those qualities will serve him well in his career.

Mary Marshall and Zhaoguo Zhu are both ambitious, hardworking, and a joy to work with. I've watched them quickly pick up a range of skills in a short period of time. I leave the lab confident that they will be able to tackle any obstacle in their path.

Zachary Hicks is always eager to help and offer his thoughts and advice in the laboratory. Zach really enjoys solving problems and has become quite good at it. I'd like to thank Sara Marquez for all her efforts working with me on the ESI source. Linjie Wang is very sharp and easy to work with. Once Nic Blando is engaged in a problem, he attacks it with an impressive and admirable intensity, energy and clever ingenuity. Gaoxiang Liu and Sandy Ciborowski have grown into competent experimentalists during my time in the lab. Mike Denchy is very thoughtful and his attention to detail as well as the pride he takes in his work is refreshing.

Rachel Harris, Chalynette Martinez-Martinez, and Marica Dipalo are recent additions to the lab. Each of them is already contributing and I'm sure all of them will be excellent additions to the lab.

During graduate school I've had the pleasure of mentoring two undergraduates, Ryan Wood and James Damewood. Ryan was always eager to tackle a problem and didn't shy away from difficult challenges. James always approached a problem methodically and his ability to learn quickly allowed him to complete several difficult projects in the lab. I'm impressed by their perseverance in the face of adversity. I know that they will both be successful and wish them the best of luck in their future endeavors.

I would like to thank the high school students that I've mentored, Andrew Frock and Luna Warren. They both showed an eagerness to learn and contribute in enthusiastic ways during their time in the lab.

Past members of the lab Angela Buonaugurio, Yi Wang, and Sarah Stokes have also been very helpful and thoughtful.

I would also like to thank two of mentors from my undergraduate studies, Scott Sibley and Jeffery Read. Both helped prepare me for graduate school and I am grateful for their tutelage.

I would like to thank Xue-bin Wang for hosting me at PNNL and for his advice and help during the construction of the electrospray source. I'd like to thank Mark Johnson for inviting us to visit his laboratory. Lai Sheng-Wang's advice has also been indispensable during this project.

Steve Smee of the Instrument Development Group (IDG) has been an invaluable resource throughout the course of this project and with the renovation and retooling of the Chemistry Student Machine Shop. I would also like to thank Joe Orndorff from the IDG for his help with the temperature controller for the cryostat.

Phil Mortimer is always eager to help and give his advice on any problem we were having in the lab. He's the best lab neighbor you could ask for.

I'm grateful to Boris Steinberg for his consistent enthusiasm and eagerness to help in any capacity. His work ethic, character, and generosity are something to be admired.

I am grateful to my family who has always supported me throughout all my life and pursuits. Their love and support have meant the world to me and I wouldn't be here today without it.

Lastly, I would like to thank my wife Raven for her unconditional love and support. It gives me great joy as I look back on our time together and fills me with more joy, hope and excitement as we embark together on the next chapter of our adventure.

TABLE OF CONTENTS

LIST OF TABLES

LIST OF FIGURES

Chapter I: Introduction

The study of negative ions and clusters allows for the investigation of novel molecular and electronic phenomena. In this work, anion photoelectron spectroscopy allows for the study of electron induced proton transfer occurring between a neutral species and a proton transferred anion in the gas phase. This technique also allows for the study of unique electronic phenomena. Anions with diffusely bound electrons and interesting electronic structures can be created and interrogated allowing for a window into their character and properties.

In addition to being interesting subject matter, negative ions are amenable to being studied spectroscopically for a range of reasons. In Figure I.1, the potential energy diagram for a molecule is presented. Anions are generally stable with respect to the neutral surface by around 2-5 eV. Another way to put this is that most electron affinities of neutral molecules are between 2–5 eV. Neutral molecules on the other hand are generally much more stable relative to their cations, their ionization potentials are generally much higher in magnitude, typically greater than 5 eV. This means that a large majority of negative anions can be photodetached by tabletop laboratory laser systems, whereas for neutral molecules much higher photon energies are required. Also, as they are charged particles, using electromagnetic fields they can be transported and focused, as well as mass selected using conventional mass spectrometers.

Anion photoelectron spectroscopy is conducted by crossing a mass selected ion beam with a fixed frequency laser beam. If the photon energy of the laser is higher than the binding energy of an electron to the anion, photodetachment will occur resulting in a

photodetached electron and a neutral molecule These photodetached electrons are then energy analyzed. The energy of detached photoelectrons are governed by the energy conservation relationship presented in Equation 1, where hν is the photon energy, EBE is the electron binding energy and EKE is the electron kinetic energy.

$$EBE = h\nu - EKE \qquad \text{(Equation 1)}$$

Using the measured EKE and known photon energy, the EBE can be calculated.

Photodetachement from the anion surface to the neutral surface yields information about the neutral molecule. In most cases, the adiabatic electron affinity (AEA) of the neutral can be experimental determined. AEA is shown as the energy difference noted in blue in Figure I.1 and in Equation 2. However, if there is poor Franck-Condon overlap between the anion and neutral potentials this transition can be obscured.

AEA = E(Neutral at Neutral Geom.) – E(Anion at Anion Geom.) (Equation 2)

The vertical detachment energy (VDE) to the neutral ground state can also be calculated.

VDE = E(Neutral at Anion Geom.) – E(Anion at Anion Geom.) (Equation 3)

The VDE, shown in Figure I.1 as the green transition, is the transition between the ground vibrational state of the anion to the vibrational state of the neutral with the highest Franck-Condon overlap. Consequently, this is the most intense observed photoelectron transition. Through the experimental determination of these values and the computational calculation of the geometries of the anion and neutral, a significant amount of information can be gleaned about the system.

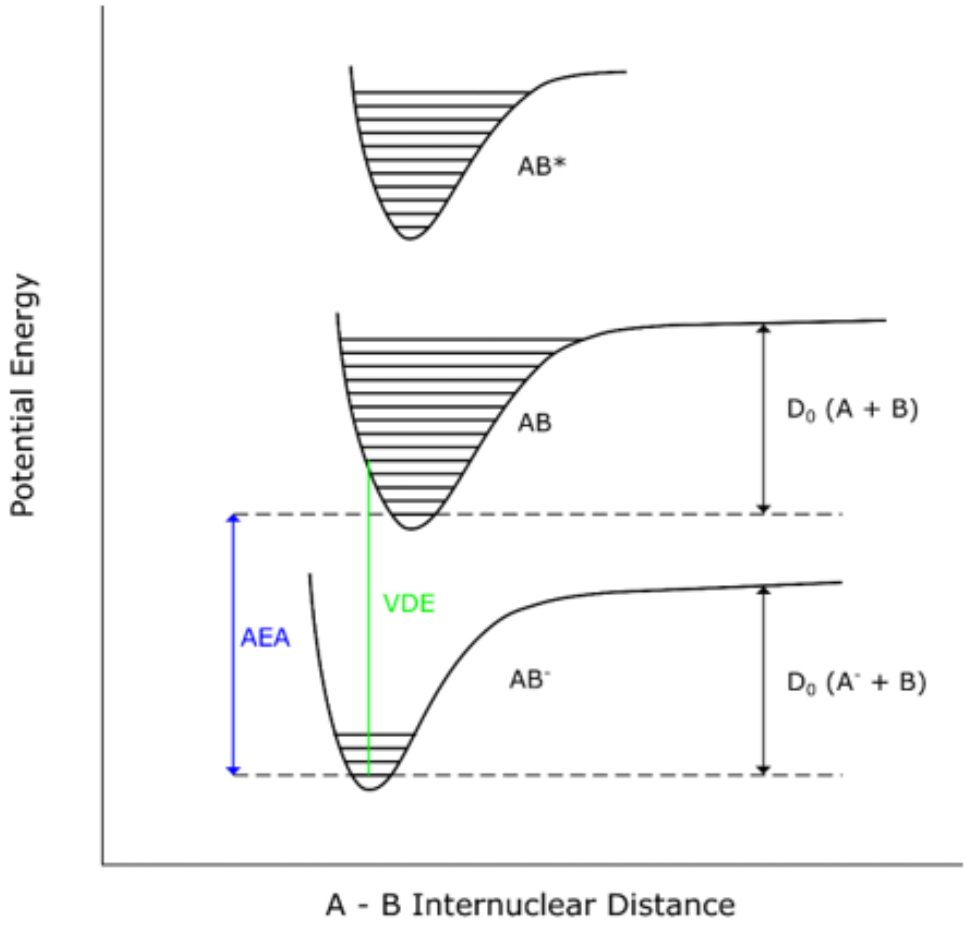

Figure I.1: Potential energy diagram detailing spectroscopic properties gleaned from anion photoelectron spectra.

The next chapter of this thesis, **Chapter II**, will discuss the experimental methods of pulsed anion photoelectron spectroscopy. This will include an introduction to ion sources including a through explanation of the electrospray ionization (ESI) source. It will also include a description of the time of flight mass spectrometer that was heavily modified to integrate with the ESI source, as well as a description of the photoelectron spectrometer.

In **Chapter III** experimental work showing the existence of a triple Rydberg anion will be presented. A triple Rydberg anion is an anion composed of a divalent positive core surrounded by three Rydberg like outer electrons. Anion photoelectron spectra of the

cluster series $Mg(NH_3)^-_{4,5,6}$ will be presented showing behavior characteristic of Rydberg like electrons. This will be compared to work previously done in the group on the double Rydberg anions $NH4^-$ and its cluster series $(N_nH_{3n+1})^-$. Preliminary computational calculations will also be presented.

In **Chapter IV** electron induced intramolecular proton transfer in acetoacetic acid will be discussed. A combined theoretical and experimental investigation will be presented. Anion photoelectron spectra of acetoacetic acid are presented. Combining these results with theoretical calculations will give insight into the factors affecting the process.

Chapter V will present preliminary data on the ascorbate system and other relevant forms of ascorbic acid. Ascorbate is the deprotonated form of ascorbic acid or vitamin C. Ascorbate can act as a radical scavenger or antioxidant neutralizing damaging radical species in biological systems.

Chapter II: Experimental

The general layout of an anion photoelectron spectrometer is presented in Figure II.1. Every anion photoelectron spectrometer requires an ion source that generates negative ions in the gas phase. Examples of such sources are laser vaporization sources, sputtering sources, electron attachment sources, and more novel sources such as electrospray ionization. These sources create a packet of negative ions with a distribution of species present. In order to perform anion photoelectron spectrometry on a species, this distribution must be measured and analyzed to identify and confirm the presence of the species of interest.

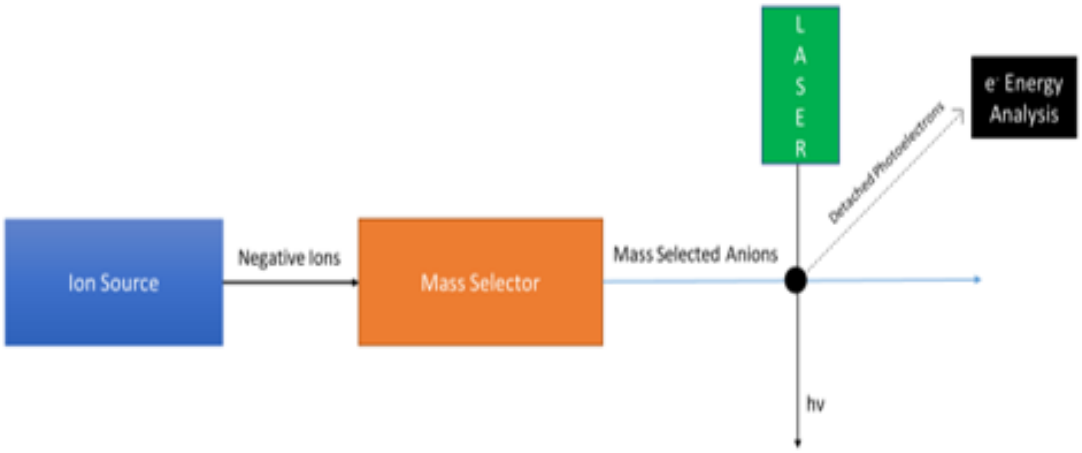

Figure II.1: Generalized diagram of the integral components of an anion photoelectron spectrometer.

The mass selector, some form of mass spectrometer, allows for ions from this distribution to be measured and analyzed according to their mass to charge ratio. Examples of such selectors are magnetic sectors, quadrupole mass spectrometers, and time-of-flight based mass spectrometers. Analysis of the spectrum and its isotope patterns, clustering and solvation patterns, as well as fragmentation pattern allow for one to identify a species of

interest. Once that species has been identified it can be isolated to perform photoelectron spectroscopy on it.

After isolation of a single species in the gas phase, that species is then crossed with a fixed frequency laser beam. If the photon energy of the laser beam is greater than the binding energy of electrons bound to the anion, photoelectrons will be detached. These resultant photoelectrons are collected, and energy analyzed. By measuring the electron kinetic energy (EKE) of these photoelectrons and using the known photon energy of the laser (hν) we can calculate the electron binding energy (EBE) of these detached photoelectrons to the neutral molecule using Equation 1.

$$\mathrm{EBE} = \mathrm{h\nu} - \mathrm{EKE} \qquad \text{(Equation 1)}$$

The anion photoelectron spectrometer used for these experiments is shown below in Figure II.2. This is a pulsed anion photoelectron spectrometer with a time-of-flight mass

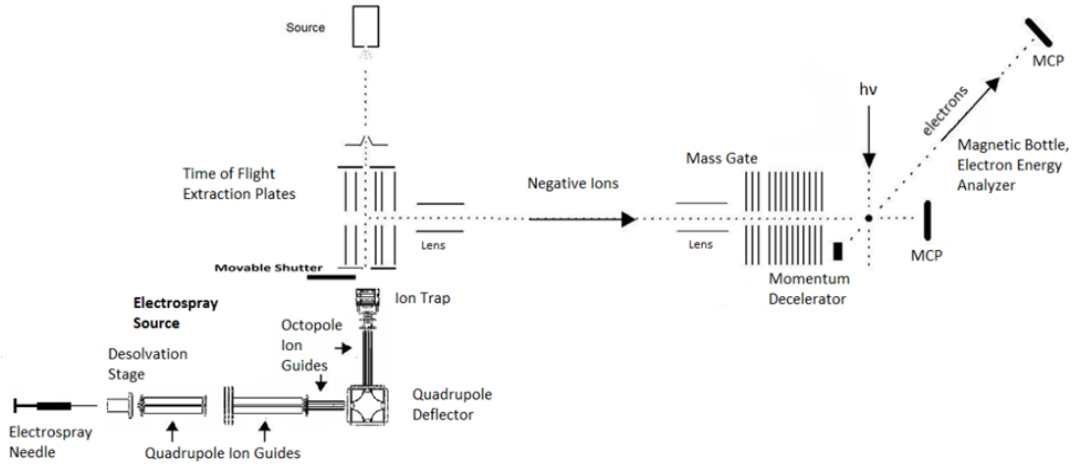

Figure II.2: Diagram of the pulsed anion photoelectron spectrometer. (MCP – Microchannel Plate Detector)

Spectrometer (TOFMS) and a magnetic bottle electron energy analyzer. Ion sources are injected on either side of the mass spectrometer. At the top of Figure II.2 there is a chamber to mount various gas phase supersonic expansion sources, for example a laser vaporization source. On the bottom of Figure II.2 is the newly constructed electrospray ionization source and its associated components.

II.1. ION SOURCES

Anion photoelectron spectroscopy allows one to peer into the electronic structure of neutral species of interest by probing its negative ion. As with most gas phase methods, the range of species available for study is highly dependent on the arsenal of ion sources available. Our group has at its disposal several ion sources (magnetron ion sputtering, pulsed arc cluster ion source (PACIS), laser vaporization, electron gun, infrared desorption, Rydberg electron transfer source, and the newly constructed electrospray ionization source.). Different sources are amenable to producing certain types of ions. The laser vaporization source can produce a wide range of clusters from metal rods, species seeded in carrier gas, or either powder or liquid sample. The PACIS source's strength is producing a wide range of metal clusters in high intensity. The electrospray ionization source connects the solution and the gas phase. Its strength is that if an ion can be produced in solution it can usually be produced by electrospray.

II.1.1 Laser Vaporization Source

Laser vaporization sources allows for the production of metal clusters, clusters from solid samples, and solvated clusters.[1] A typical laser vaporization source consists of a metal target rod, a housing, nozzle, pulsed gas valve, and a focused laser beam (Figure II.3). To make clusters, a pulse of gas is fired over the rod as it rotates and translates. Generally,

this is either pure helium or a gas mixture with a small amount of another gas one would want to incorporate into the ion or cluster. When the density of gas is amenable to

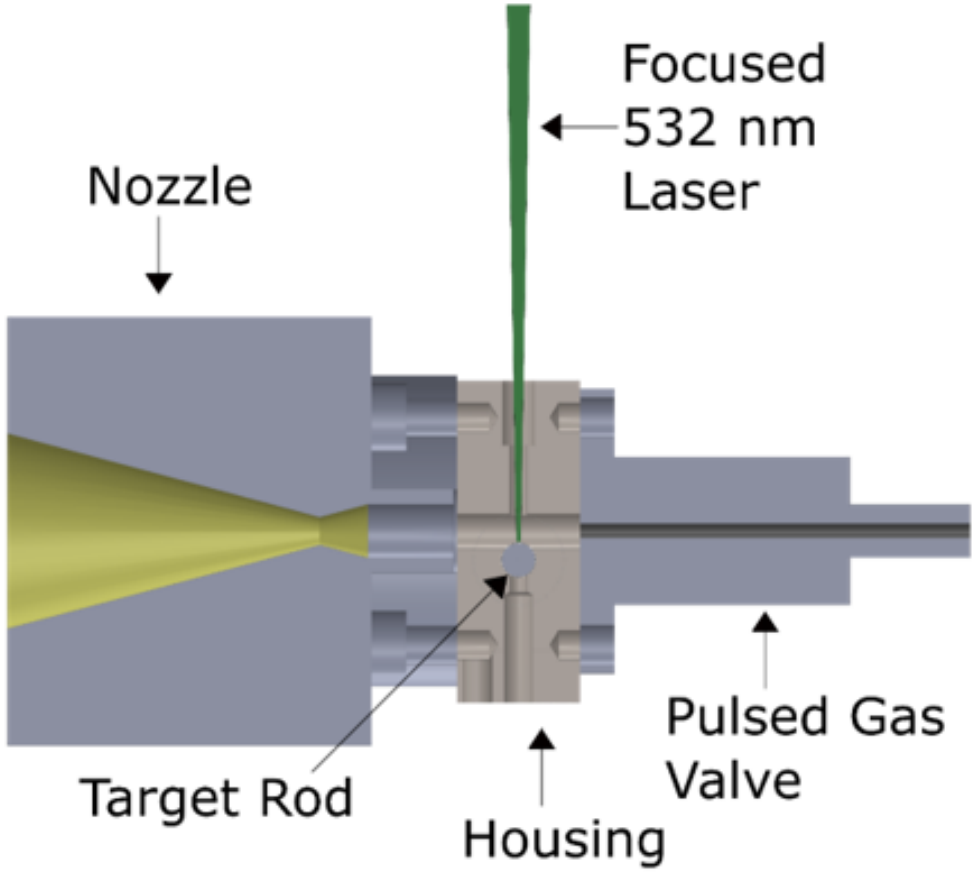

Figure II.3: Laser vaporization source diagram.

making clusters, the laser is fired and vaporizes a small portion of the rod generating a plasma. As the plasma and gas mixture travels through the source and out the nozzle

towards the skimmer, it cools and forms anions and anionic clusters which are transported into the TOFMS.

II.1.2 Pulsed Arc Cluster Ionization Source (PACIS)

The PACIS source produces metal clusters in high intensity.[2, 3] A diagram of the source is presented in Figure II.4. The source consists of a grounded target rod containing the metal or metals one wants to incorporate into a cluster, a copper electrode which supplies pulses from the power supply, a pulsed valve, a cooled quartz block to contain the plasma, and a pulsed valve containing an ionizable carrier gas. This carrier gas is pulsed into the quartz block then shortly after a 30 μs high voltage and high current pulse is applied. This pulse causes both ionization of the gas, and thus sputtering of the target rod, as well as direct ablation via the electric pulse. This produces a large number of cations, which then undergo collisions within the extender tube producing anions. These anions are then transported into the time of flight for mass analysis.[3]

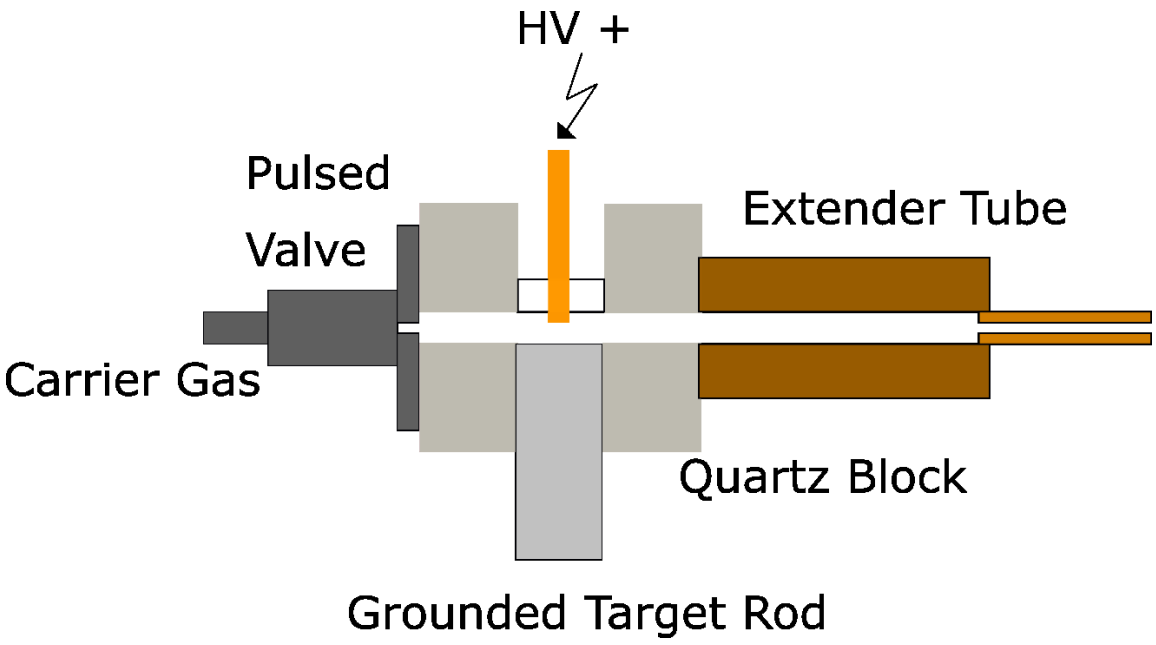

Figure II.4: Diagram of the Pulsed Arc Cluster Ionization Source (PACIS).

II.1.3. Electrospray Ionization

The advent of the electrospray ion source has created a route from the solution phase to the gas phase.[4] Electrospray ionization allows for a solute dissolved in solution to be transferred to the gas phase. Applying a high voltage potential to a solution in a small capillary causes charged species within that capillary to separate (Figure II.5). As charges begin to separate, those of opposite polarity of the applied voltage cross the threshold of

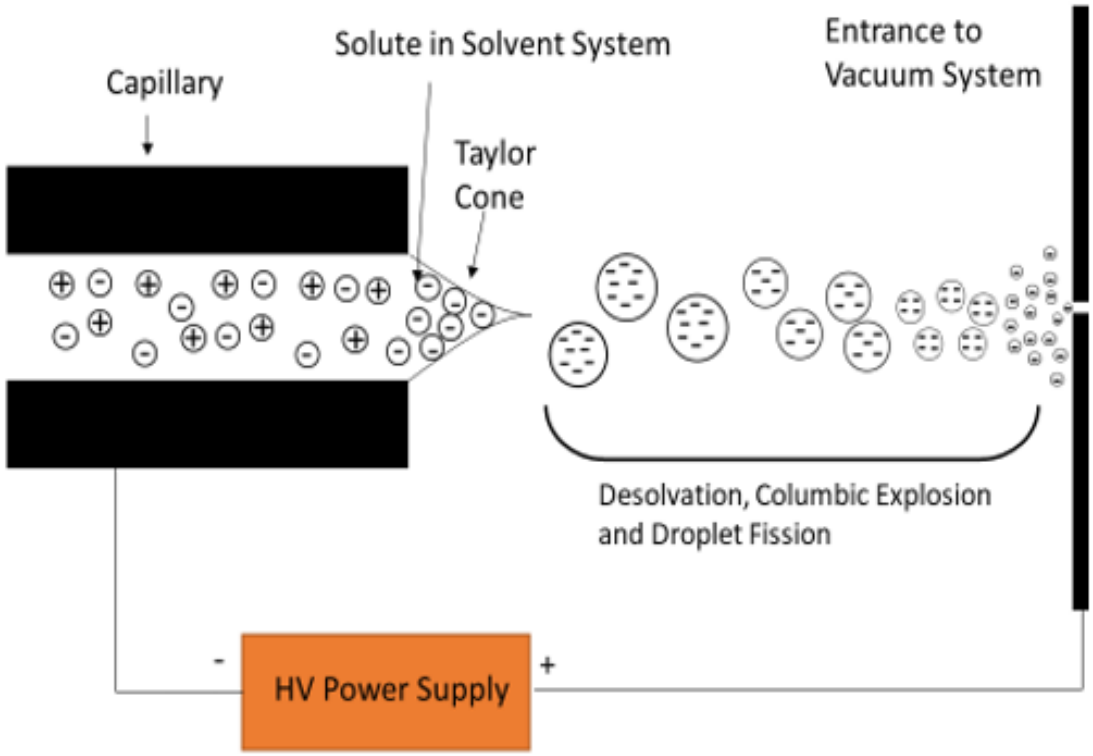

Figure II.5: Diagram of Electrospray Ionization Source (ESI).

the capillary forming a Taylor cone.[5] At the tip of the Taylor cone, highly charged droplets form and bud off. As they travel through the ambient atmosphere towards an anode plate or the entrance of the vacuum system, they begin to desolvate. This causes the droplet to become progressively charged until the surface tension of the droplet can't support any more changes. The droplet then undergoes a process called coulomb

explosion, causing fission into smaller droplets.[6] Desolvation continues and this process in turn occurs in the daughter droplets. Eventually after enough desolvation, either bare ions or discretely solvated ions are produced and travel through atmosphere to the counter anode or in this case the entrance to the vacuum system.

In negative ion mode there are generally three typical types of species produced. For molecules with an acidic hydrogen it's typical to see deprotonated species $[X\text{-}H]^-$, where X is the parent molecule. For salt solutions the bare anion $[X]^-$ is seen in high intensity. In either case it's also possible to see solvated species of both ($[X\text{-}H]^-[S]_n$ or $[X]^-[S]_n$ where n is a discrete number of solvent molecules.

Generally, if one can generate a stable ion in solution, electrospray ionization allows for the facile transfer of that species to the gas phase. Electrospray also has the advantage of being a soft ionization process. Many gas phase ion sources rely on a plasma or high energy environment to generate ions of interest. Electrospray can be thought more of as transferring intact ions from solution to the gas phase as the majority are preformed in solution through either deprotonation of an acidic hydrogen or dissolution of a salt. Due to the gentler nature of this process it's possible to get large molecules, for example inorganic clusters or proteins, into the gas phase without fragmenting them.[7] Additionally in negative ion mode, ESI is able to generate doubly charged negative ions as one bypasses having to surmount the columbic barrier to adding a second electron to an already negatively charged species as they are preformed this way in solution prior to entering the gas phase.

While this ionization method is powerful, there are two challenges to overcome in order to perform spectroscopy on molecules produced by ESI via PES. Since these molecules

are generated in the ambient atmosphere, they are generated at room temperature. These ions are relatively hot compared to ions made in vacuum from supersonic expansion-based sources. To generate well resolved photoelectron spectra of these species, it's necessary to cool them prior to photodetachment. Another challenge is that these ions must be transferred from atmosphere to high-vacuum in high intensity in order to perform anion photoelectron spectroscopy on them. The rest of this section will detail all the components of the electrospray ionization. The design of this source was based on the previous designs of Lai-sheng Wang, Xue-Bin Wang and Mark Johnson.[8-10]

II1.2.1 ESI Needle and Spray Chamber

Electrospray generates ions at ambient room temperature and pressure. In order to stabilize the spray as well as control the humidity in the ambient environment around the electrospray needle a humidity control chamber was developed. Having an ambient humidity around the electrospray needle of less than 20% helped to stabilize as well as increase the intensity of ions transmitted through the ion guide system. This consists of an acrylic box with an extruded aluminum frame. There is an input gas port to flow dry nitrogen gas in order to dry out the chamber. By controlling the flow of dry N_2 into the chamber one can roughly control the humidity.

To run a sample via ESI, the solution of interest is loaded into a 2.5 mL Hamilton syringe (Hamilton PN: 81416). Solutions are generally prepared in the millimolar concentration range. A variety of solvent systems can be used; for most systems a 3:1 methanol:water mixture works well, as well as pure acetonitrile. After loading, a pulled silica emitter tip is attached to the syringe via a Microtight fitting and PEEK sleeve (IDEX PNs: P-720, F-182). This emitter tip is generated in the lab by taking 250 μm OD Peek coated fused

silica tubing and pulling it under a torch (Polymicro Technologies PN: TSP050192). This tip is then opened by cutting it and then mounted in a peek sleeve and attached to the fitting. This needle with fused silica emitter tip is then mounted in a syringe pump (Harvard Apparatus Model 22). The flowrate is generally set at 3.0 μL/min, but can be adjusted for stability and intensity. This syringe pump is mounted on an adjustable platform allowing for optimization of the position of the needle relative to the capillary. A high voltage of - 2 – 3 kV is applied to the needle of the syringe. The position of the needle is optimized by measuring the current on the first skimmer and moving the syringe pump, thus moving the emitter tip, for maximum ion signal. For NaI an excellent ion current on the first skimmer is ~20 nA. The capillary is the entrance into the differential pumping and ion optical system which transmits ions from atmosphere to the ion trap operating at high vacuum.

II.1.2.2 Differentially Pumped Ion Guide System

A differentially pumped ion guide system is used to transfer these ions from atmosphere where they are generated to the mass and anion photoelectron spectrometer operating at high vacuum. This system consists of four differentially pumped stages or chambers with ion guides in them to transfer the ions through these chambers. Ion guides were used due to their high transmission, high transmission across a wide range of pressures, and they are amenable for use with ion beams with low kinetic energies.

II.1.2.2.1 Ion Guides

Ion guides are used to maximize transmission of these ions from atmosphere to high vacuum. Ion guides allow for the application of an oscillating multipolar field to contain ions as they traverse the vacuum system. In order to create this field, a set of circular

stainless-steel rods are arranged on a circle equidistant from one another at a specific inscribed radius (Figure II.6). This simplest ion guide is a quadrupole consisting of four rods. Two radio-frequency (RF) waveforms are then applied to alternating sets of the rods as shown in Figure II.6. These waveforms are generated 180° out of phase by a homemade RF power supply.[11, 12] As these waveforms evolve through time, they generate an oscillating quadrupolar field. The inscribed radius of the rods, frequency of the applied

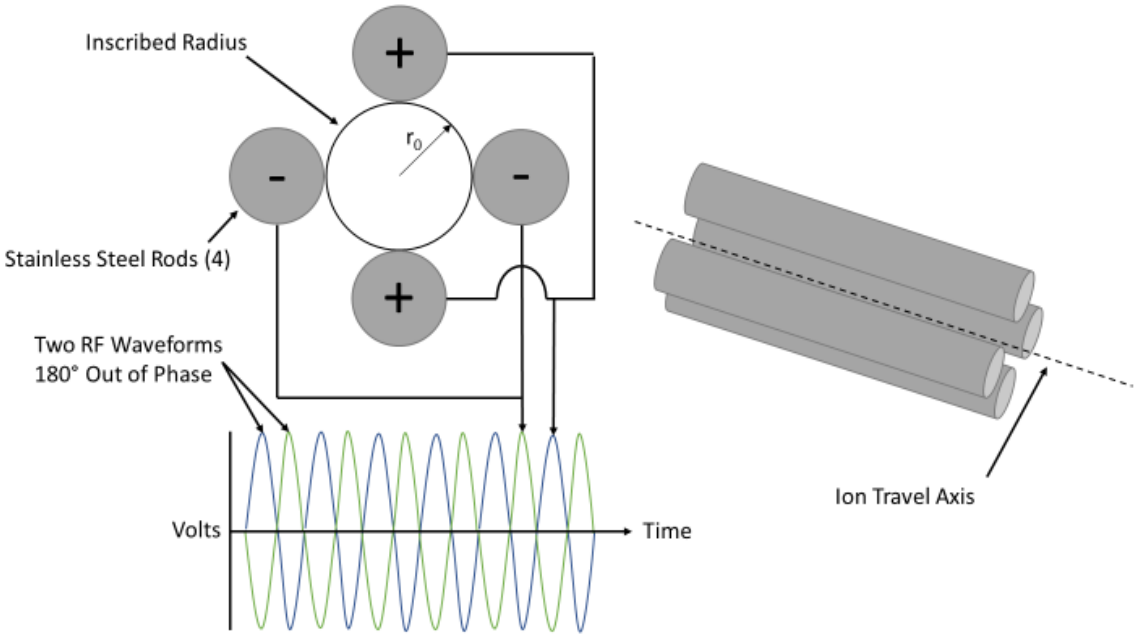

Figure II.6: Diagram of ion guides and RF waveforms placed on them.

waveforms, peak-to-peak voltage of the applied waveforms, and kinetic energy transverse to the axis of the guides of the transmitted ion all determine the mass range of ions that can be passed by the guide.[13, 14] Ions within this mass range will spiral down the length of the guide at a resonant frequency and with high transmission.

As a consequence of the of the effective potential produced by multipole ion guides, there is a significant difference in the potential an ion feels and the focusing provided by

guides based on the number of rods that constitute them.[14] As seen in Figure II.7, the effective potential is plotted based on the reduced radius of the guide. As can be seen quadrupoles have a parabolic potential. In octupole ion guides this potential is flat in the center and becomes steep close to the rods. This means that ions entering a quadrupole vs an octupole are better focused by the quadrupole. Any deviation from the center and ions will feel a restorative force centering them in the guide. In an octupole ions must drift significantly further from the center in order to feel the same restorative force. However, while focusing is better in a quadrupole, transmission is much higher and approaches 100% for octopoles.[15, 13] As a consequence of this, the first two guides in the ESI are quadrupoles and the last two are octopoles. This is to focus the divergent beam with the quadrupoles initially and then to maximize transmission to the trap with the octopoles.

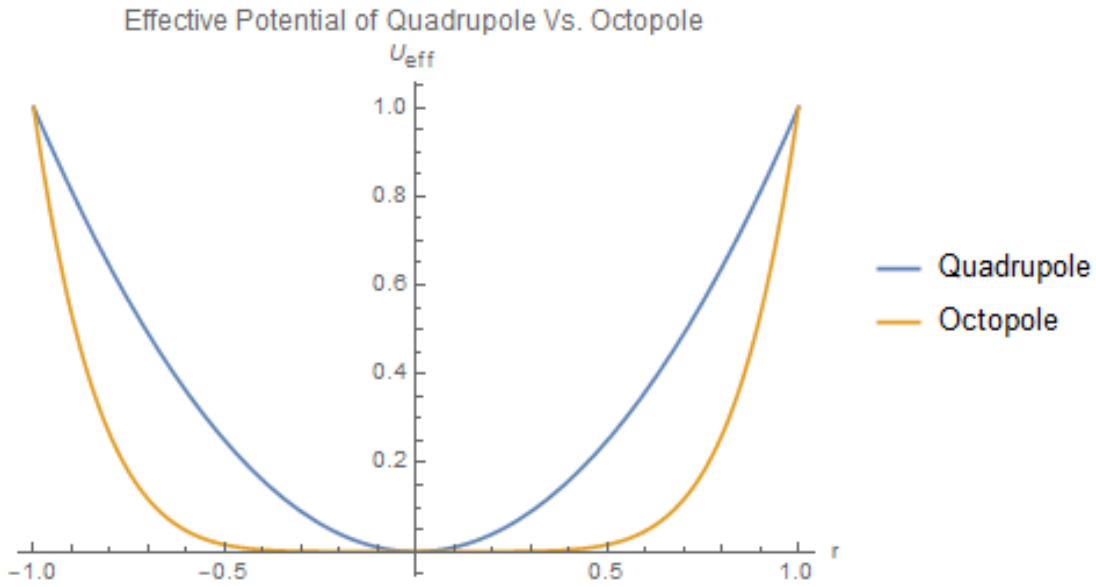

Figure II.7: Comparison of effective potential seen by ions in a quadrupole vs. octupole ion guide.

The differential pumping and ion guide system in this instrument is shown in Figure II.8. Through the course of these four differential pumping stages, ions are transmitted from

atmosphere (760 Torr) to the ion trap operating at high vacuum ($5.0x10^{-6}$ Torr). To guide them through this system, the ion guides and the skimmers are floated at different dc voltages. This float voltage is largest in magnitude on the first skimmer and is typically -30 V. The voltage on the first skimmer sets the kinetic energy of the ions being transported through the ion guide system. The float voltage on optics generally decreases moving from this skimmer towards the ion trap which is held at ground. This potential difference allows ions to be transported from the first skimmer to the ion trap. A diagram of the apparatus and pumping system including the ESI is shown in Figure II.9.

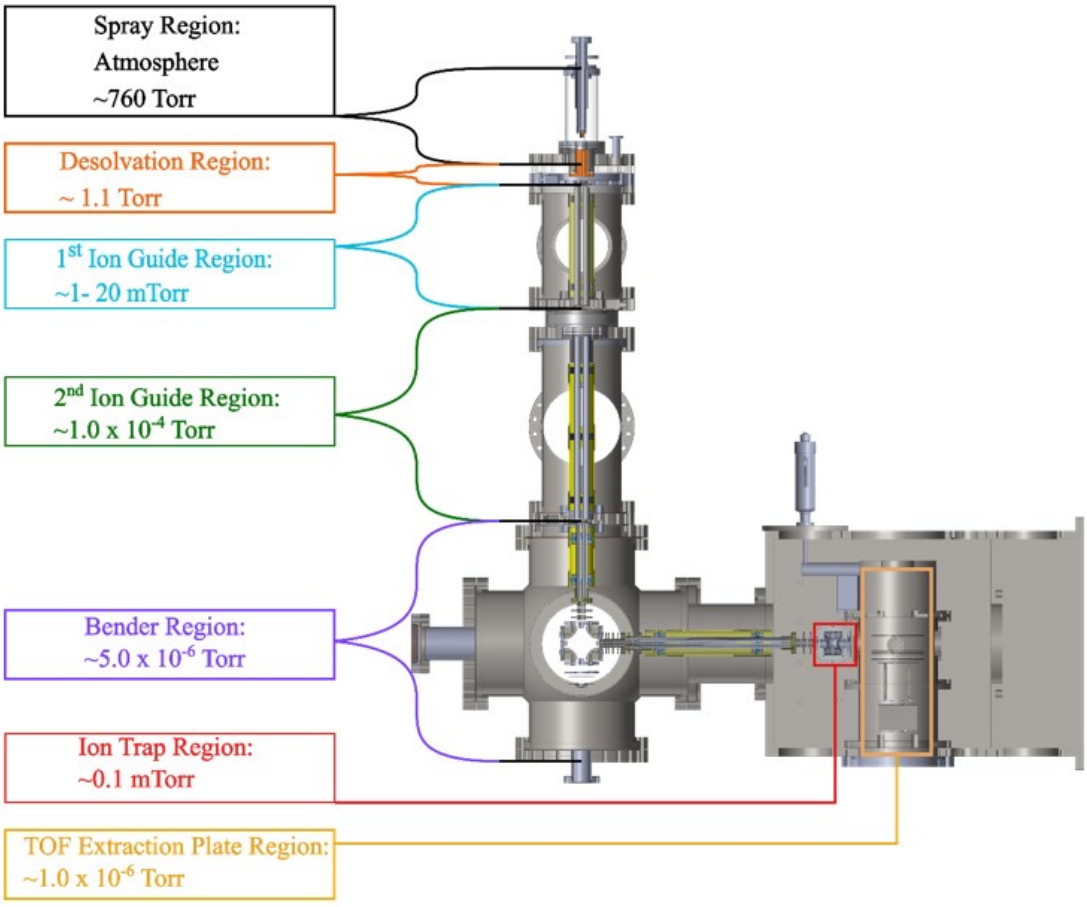

Figure II.8: Diagram of ESI differential pumping system and operating pressures

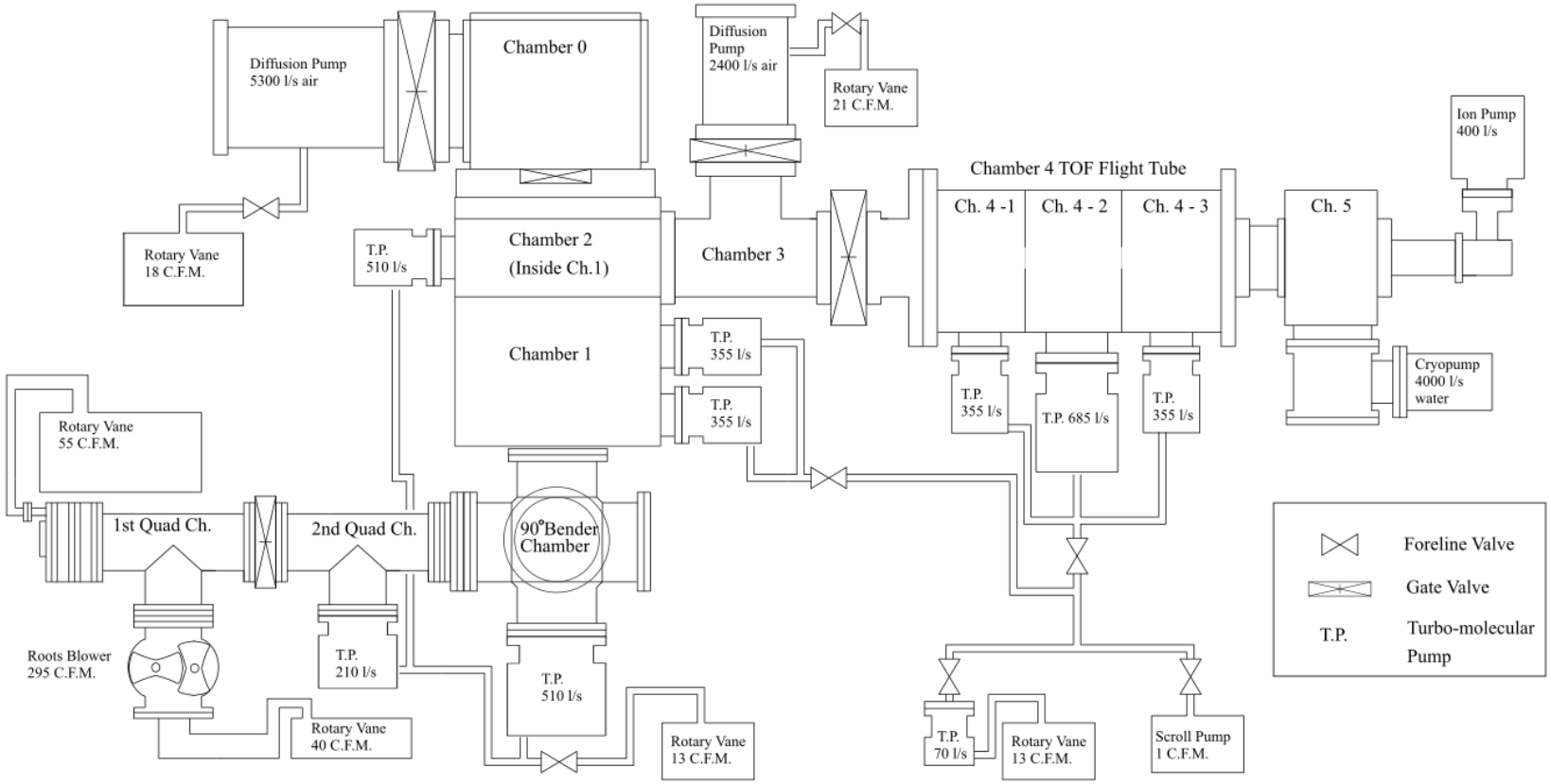

Figure II.9: Diagram of pumping of anion photoelectron spectrometer.

II.1.2.2.2 Desolvation Stage

The ESI ion optical system is shown in Figure II.10. Ions generated by ESI traverse a stainless-steel capillary 1.9 inches in length with an internal diameter (ID) of 30 thousandths of an inch. After exiting the desolvation capillary, ions and droplets enter the desolvation stage which is the first stage of the differential pumping system (Figure II.10). This stage is backed by a rotary vacuum pump (60 CFM) and maintains a pressure of 1.1 Torr. Ions travel a short distance and then traverse a 4 mm ID skimmer and enter the first ion guide chamber. The voltage set on this skimmer defines the kinetic energy of the ions entering the ion guide system. Ions can additionally be guided through this chamber by floating the block assembly.

The desolvation capillary is heated by two cartridge heaters which heat the copper block that holds it. The temperature of the block is varied by controlling the AC voltage going through these two heaters via a Variac autotransformer. The temperature that's optimal for the system of interest depends on the system and solvent system used. As a general guide, temperatures above 50°C and below the boiling point of the highest boiling point solvent in the system tend to work well.

II.1.2.2.3 1st Quadrupole Chamber – Focusing Quadrupole

Once ions traverse the first skimmer, they enter the first ion guide differential pumping chamber. The two quadrupoles in this source are made from 0.5 inch Stainless Steel rods and sit on an inscribed radius of 0.22 inches. The first quad is shaved down to fit as close as possible to the first skimmer in order to maximize transmission. As ions exit the capillary in the previous chamber and traverse the skimmer, they are highly divergent.

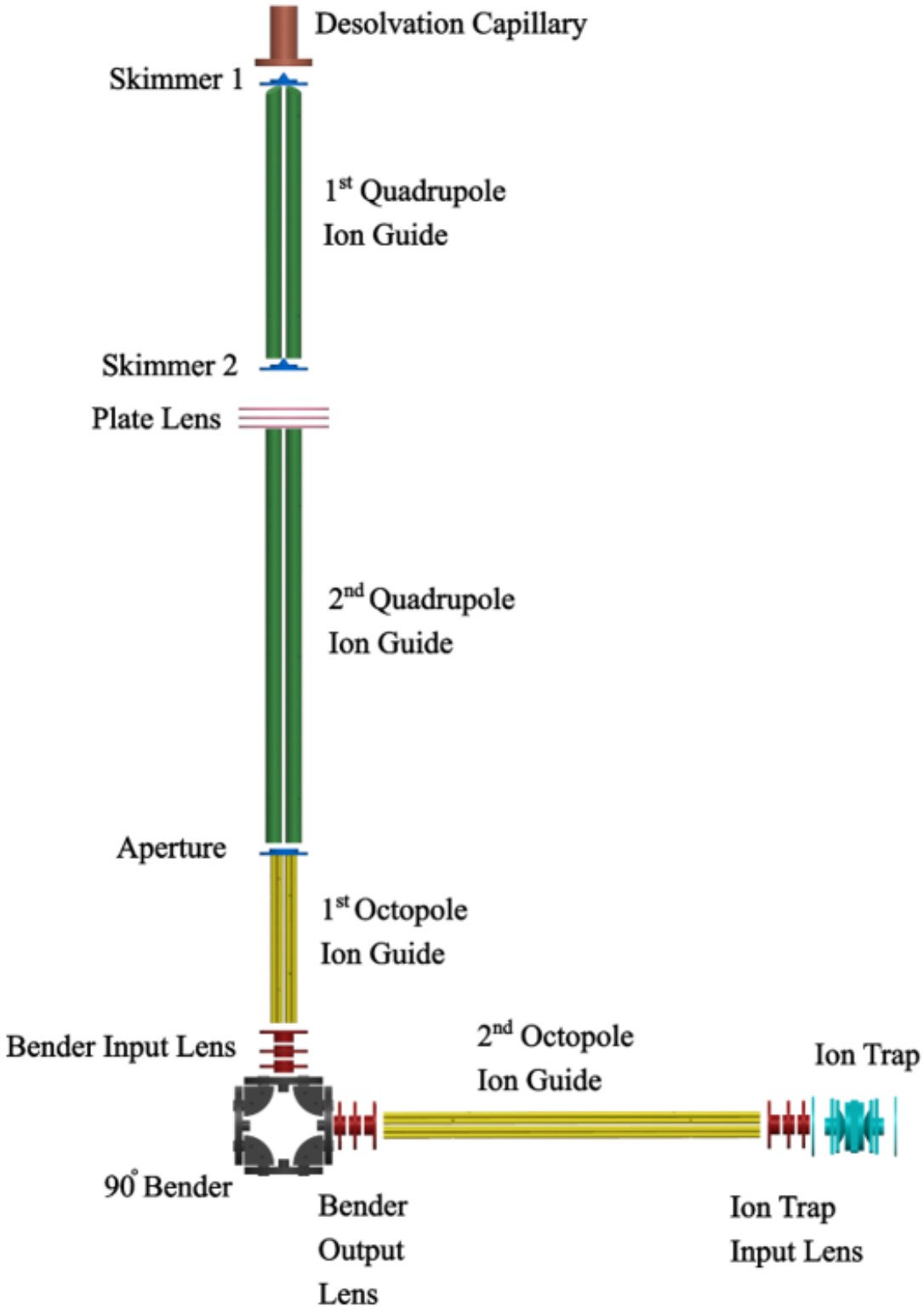

Figure II.10: Ion optics for ESI source.

Due to their divergent nature they have a significant kinetic energy component transverse to the axis of the guide. This would limit the transmission of ions through this chamber, as a large portion of ions would have enough kinetic energy to exit the guiding field. To counteract this, this quad is operated as a focusing quadrupole. The relatively high pressure causes ions in the chamber to have a low mean free path. The combination of a guiding RF field as well as numerous collisions with background gases in the chamber, attenuate the transverse energy of the ions and allows for higher transmission through the chamber.[16, 17] The 1st quadrupole guides ions exiting the first skimmer into the second skimmer.

This chamber's pressure is kept at ~10 mTorr. Its large gas load is pumped by a Roots blower (Leybold-WA500, 300 CFM) which is backed by a rotary vane mechanical pump (Leybold – DB40B, 30 CFM). In order to prevent a vacuum failure in the higher vacuum regions of the machine due to the failure of pumps in this region, a pneumatically actuated gate valve isolates this chamber from the higher vacuum section of the machine. This valve is interlocked to prevent opening the valve when the pressure is high and will also cause the valve to close in the event of vacuum failure.

II.1.2.2.4 Gate Valve Gap and Second Quadrupole Chamber

As ions enter the next chamber, they enter high vacuum. This chamber is pumped by a turbomolecular pump (Pfeiffer 260 l/s) and maintains an operating pressure of ~1.0 x 10^{-4} Torr. An insertable gate valve separates this chamber from the previous chamber. This allows the high vacuum portion of the machine to be isolated from the higher pressure ESI source chambers.

Ions exit the skimmer in the previous chamber and then traverse the valve. As they travel

through the valve these ions are unguided and will diverge. A three-element plate lens is attached to the front of the quadrupole ion guide in this chamber, allowing for the beam to be refocused into the quadrupole to maximize ion transmission. Ions travel down the quadrupole and into an 1/8” aperture (Figure II.10).

II.1.2.2.5 Octopole Ion guides and Quadrupole Bender

After traversing a small aperture, ions enter the first octupole ion guide. All the octopole ion guides in the ESI source are made from 3/16” diameter rods and sit on a radius of 0.375” giving the rods an inscribed radius of 0.275”. After traversing the octupole, a three-element lens focuses the ions into a quadrupole bender. This quadrupole bender allows for ions to be bent 90° while maintaining a high transmission.[18, 19]

After being bent 90°, the ion beam is picked up by another lens and focused into the second and final octupole ion guide. After traversing this guide these ions are focused by another Einzel lens into the cryostat heat shield containing the ion trap. The chamber containing these guides, quadrupole bender and cryostat is pumped by three turbopumps (1.Pfeiffer, 510 l/s 2. Pfeiffer HiPace 300, 260 l/s, ,3. Pfeiffer HiPace 300, 260 l/s) in order to pump away the buffer gas from the ion trap.

II.1.2.2 Ion Trap

An ion trap is used in order to couple the continuous ion signal from the ESI source to the pulsed time-of-flight mass and photoelectron spectrometer (Figure II.11). The ion trap stores ions for a period and then pulses them out at a discrete time. This allows for an intense packet of ions to be injected into the time-of-flight mass spectrometer and for their injection to be synchronized in time with its operation.

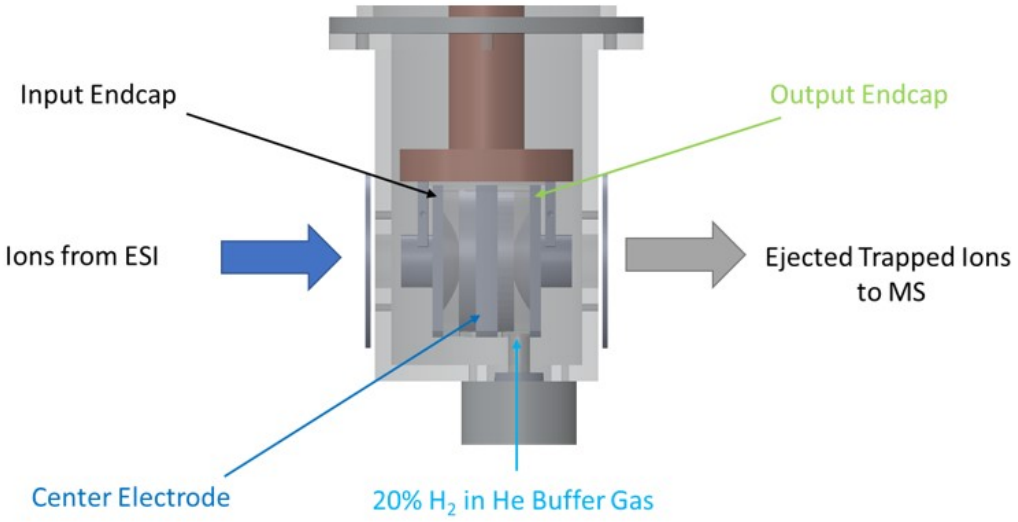

Figure II.11: Diagram of the Ion trap.

The ion trap is 3D Paul Trap, a three-element ion optic consisting of two endcaps and a center electrode with a hyperbolic inner surface.[20] Ions enter the cryostat where the ion trap is held and are focused through the input endcap into the trap. Once inside the trap, ions encounter two forces, collisions with buffer gas molecules which attenuates their kinetic energy and a one MHZ oscillating RF electric field, adjustable from 0 to 4000 V peak to peak, with a stable point within the center of the trap. By leaking buffer gas into the trap, the pressure of the trap is kept ~0.1 mTorr. As ions collide with the buffer gas and lose their kinetic energy, the oscillating RF field guides and traps them towards the center of the trap.

Once ions are trapped, they are then extracted and pulsed into the time-of-flight mass spectrometer. The ion trap and mass spectrometer operate at 10 Hz. Based on this duty cycle, ions are trapped for 100 ms before being ejected out of trap and into the mass spectrometer. The timing scheme for the ion trap is shown in Figure II.12. The trap is in "Trapping Mode" for 100 ms until a signal is sent to its RF power supply. The power

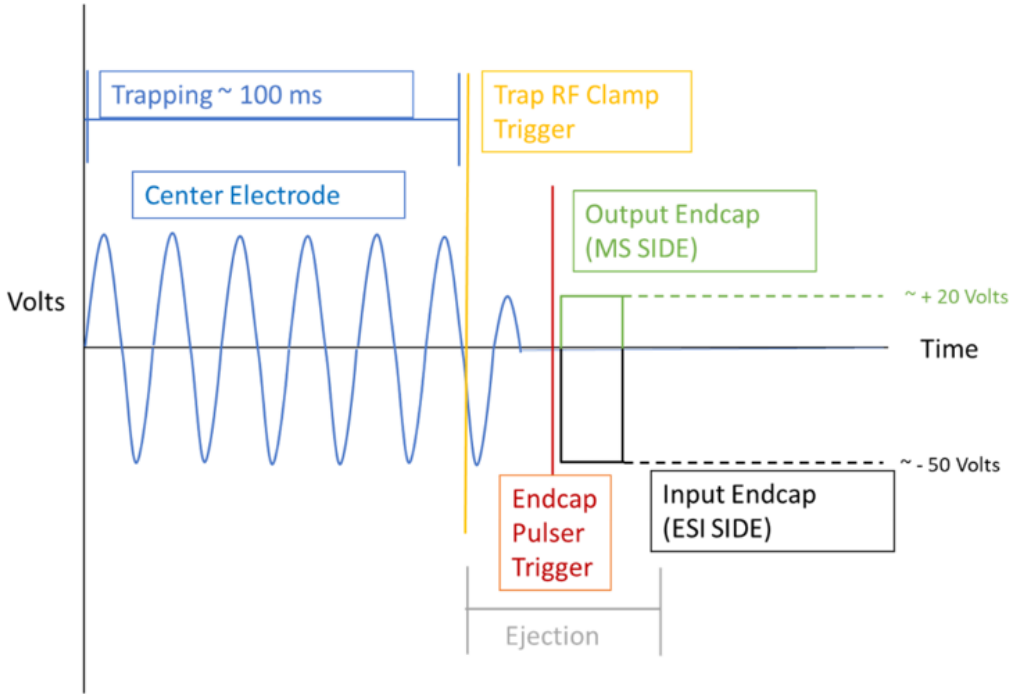

Figure II.12: Extraction scheme for ion trap.

supply then "clamps" the RF and after a few cycles it completely attenuates. The endcaps, held at ground during trapping, are then pulsed in a bipolar arrangement to eject ions out of the trap in a focused ion packet.[10] When the pulser is fired, two opposite polarity pulses are applied to the endcaps. On the input endcap, where ions enter from ESI, a -50 V pulse is applied. Simultaneously a positive 20-volt pulse is applied to the output endcap, on the side near the entrance to the mass spectrometer. This gives the ion packet 10 eV of kinetic energy as they travel into the extraction region.

II.1.2.3 Cryostat

Ions generated by ESI are made at ambient pressure and temperature in the solution and then transferred to the gas phase. The ESI process does not provide any cooling and these ions have a temperature of ~298 K. Ions made by other common gas phase ion sources, such as laser vaporization, are cooled in a supersonic expansion, yielding ions that are 10

K and cooler. Due to ions being hotter and vibrationally excited, the photoelectron spectra become more convoluted (hot bands) and less resolved.[8]

In order to acquire higher resolution and less congested photoelectron spectra, these ions are cooled in the ion trap by attaching it to a cryostat. The cryostat is a custom liquid nitrogen flow cryostat that was fabricated by Advanced Research Systems. This cryostat was specially fitted to have a flanged mount to allow attachment of the ion trap and its mount. In this flange there is both a silicon diode and a cartridge heater. LN2 enters through the top through a pressurized transfer line attached to a dewar. By controlling the pressure of the dewar and the current of the heater, temperature control can be achieved. The current applied to the heater is controlled by a custom temperature controller provided by the Instrument Development Group. This allows for temperature control from 298 K to 77 K.

In addition to the cryostat, several custom and off the shelf parts were added to mount and house the ion trap on the cryostat and to adapt the cryostat to the machine (Figure II.13). A tilt adjuster (UHV Design Part #: PA35) was added to the cryostat in order to allow tilt and slight height adjustment under vacuum. When the cryostat cools, the metal that constitutes it contracts and slightly shifts the alignment of the trap, this tilt adjuster allows for this slight contraction to be compensated for.

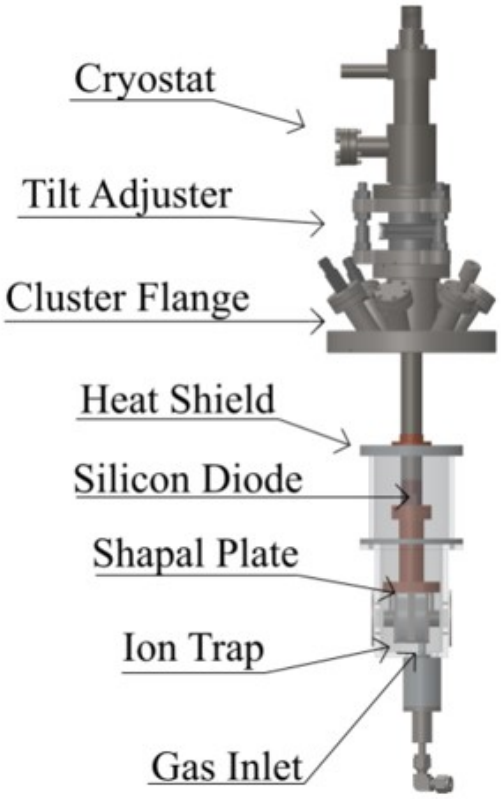

Figure II.13: Cryostat and associated components.

On the cluster flange (Figure II.13), all the feedthroughs for voltages and gas for the ion trap are mounted. The trap is encased in an aluminum heat shield and mounted on a OFHC copper mount. In order to maintain a high thermal conductivity between the trap and the cryostat, a Shapal plate is sandwiched between the trap and it's copper mount. Shapal is a machinable ceramic that has a high thermal conductivity at 77 K but is also an electrical insulator.[21] To facilitate heat transfer, Apeizon N was applied to the surfaces of the Shapal plate and metal interfaces.

On the bottom of the heat shield there is a port for the addition of trap buffer gas. Currently, gas is continuously leaked into the trap and controlled by a regulator and leak

valve. The trap buffer gas is 20% H_2 in a balance of He. This allows efficient cooling of ions held in the trap due to helium rapidly exchanging with the cooled walls of the trap. In addition, it's been found that small diatomics, like H_2, more effectively cool molecules held within a trap. This is likely due to the fact that H_2 has a rotational constant and can, through collisions, transfer vibrational energy from the ions.[8]

II.2 TIME OF FLIGHT MASS SPECTROMETER (TOFMS)

The mass selector in this anion photoelectron spectrometer is a time-of-flight mass spectrometer (TOFMS). Ions from either side of the machine are directed into a differentially pumped chamber containing the extraction plates and the beginning of the TOFMS. The TOFMS separates ions in time based on their mass to charge ratio. In order to separate ions by their mass to charge ratio (m/z), or in the case of singly charged ions their mass, these ions are given the same kinetic energy. The kinetic energy (KE) of an object is given by Equation 2, where m is the mass of the particle, v is the velocity, and d is the distance traveled over time t.

$$KE = \frac{1}{2}mv^2 = \frac{1}{2}m\left(\frac{d}{t}\right)^2 \qquad \text{(Equation 2)}$$

For charged particles of charge q, the application of an electric field E over a distance d, defines their kinetic energy shown in Equation 3.

$$KE = qdE \qquad \text{(Equation 3)}$$

Once ions enter the extraction plate region these plates are pulsed to a voltage. The electric field created by these voltages sends ions traveling towards the detector at a

single kinetic energy. Combining Equations 1 & 2 yields an expression for the ions flight time t, over the distance to the detector, D which is placed on the applied voltage, V.

$$t = \frac{D\sqrt{m}}{\sqrt{2qdE}} = \frac{D\sqrt{m}}{\sqrt{2qV}} \qquad \text{(Equation 4)}$$

The extraction plates in this instrument are a modified Wiley McLaren type consisting of four plates with two separate acceleration zones.[22, 23] This arrangement allows for higher mass resolution and a large extraction volume. Voltages are applied to these plates using two fast Push-Type MOSFET switches. As can be seen in Figure II.14, Region 1 is the extraction volume and the first acceleration region. Ions in this region see a high voltage pulse on the left most plate of -1500V and on the adjacent plate of ~1410V, sending them towards the detector and the right of the diagram. Ions then drift through a field free region, Region 2, as both plates are held at -1410V and then into the second acceleration region, Region 3, where they see a large drop as the final plate is held at ground.

After exiting the extraction region, ions enter horizontal and vertical deflector set (Figure II.14 – Region 4 & 5) and then a large Einzel lens (Figure II.14 - Region 6). To accommodate the ion packet ejected from the ion trap, modification of the existing TOF optics were necessary. Injecting ions in high intensity into the extraction region of the TOF from the trap, necessitates ejecting ions from the trap with a push pull scheme as detailed earlier. Ions are ejected out of the trap with a kinetic energy of ~10 eV. This is about five times as much kinetic energy transverse to the TOF axis than the supersonic expansion sources previously used on the machine. To accommodate this large transverse kinetic energy, the deflector plates needed to be modified. The existing deflectors were

separated into two units and enlarged, both along the TOF axis in order to increase the amount of deflection and perpendicular to that axis to ensure a uniform and ideal field.

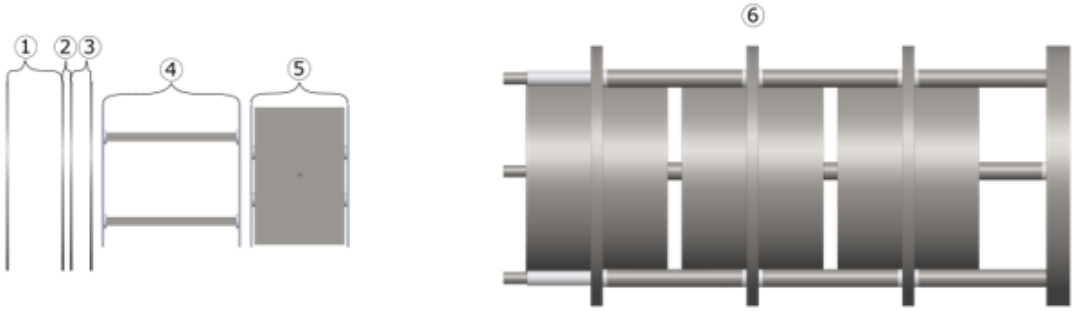

Figure II.14: Diagram of extraction plates, deflectors and first Einzel lens. View is looking down from the top of the instrument. (1 – First acceleration region: Left most plate is pulsed to -1500 V and the next plate is ~1410 V. 2 – Field Free Region – Both of these plates are held at -1410 V. 3 – Second Acceleration Region: Left plate is pulsed to -1410 V and right plate is held at ground. 4 – Horizontal Deflector. 5 – Vertical Deflector. 6 – First Einzel lens.)

In addition to modification of the deflectors the focusing optics needed to be replaced. Due to their significant kinetic energy transverse to the TOF, ions ejected from the TOF were unable to be focused by the initial 2" diameter Einzel Lens. Simulations in SIMION showed that ions would fill the lens and get too close to the internal surfaces of the lens, causing aberrations in the optical focusing of the beam. This caused ions to be scattered rather than being focused onto the microchannel plate (MCP) detector. The lens was replaced with another lens with a 4" inch ID to ensure ions wouldn't fill the lens and these extracted ions could be focused into the MCP.

An additional lens was added in order to further focus ions into the interaction region for photodetachment. This lens is a 1.5" diameter Einzel lens is mounted off the assembly that contains the mass gate and momentum decelerator. The arrangement of these optics

is shown in Figure II.15. This lens takes the beam focused by the first Einzel lens and further focuses it into the interaction region and onto the ion MCP detector.

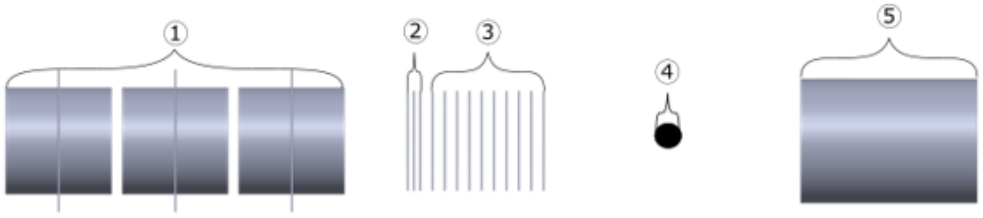

Figure II.15: Diagram of ion optics near photoelectron interaction region. (1 – 2nd Einzel Lens, 2 – Mass Gate, 3 – Momentum Decelerator, 4 – Interaction Region, 5 – Ion microchannel plate detector)

In order to install the first lens a small diameter (0.70" OD) differential pumping tube needed to be removed to provide clearance for the lens, as well as clearance for the ion beam. In order to maintain a pressure less than 5.0 X 10^{-8} Torr in the interaction region for photodetachment, differential pumping sections needed to be added to the TOF flight tube. To add these regions, two large plates with align-able apertures were mounted to tabs already present in the chamber (Figure II.15). This allowed for this empty chamber to be repurposed into three separate differentially pumped chambers. The addition of

turbo-molecular pumps to each of these sections allowed for the pressure in the interaction region to be maintained while incorporating the improved lenses.

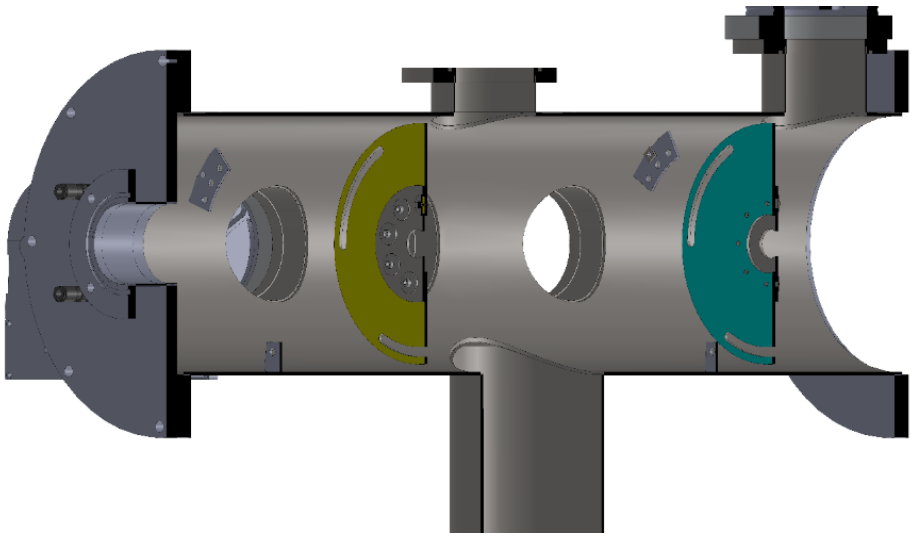

Figure II.16: Vacuum walls added to TOF flight tube**.** Vacuum partitions are shown in yellow and blue.

After exiting the second Einzel lens ions pass through the mass gate (Figure II.15 – Region 2). The mass gate allows one mass to be selected to enter the photoelectron interaction region. The mass gate is composed of three grids. During operation, the first and last grid are held at ground while the center grid is held at a high negative voltage. The voltage is set to be higher than the beam voltage, in order to reject all but the ion of interest. As the ion of interest approaches the mass gate the middle grid is pulsed to ground and after several hundred nanoseconds the grid is pulsed back up to a high negative voltage. This allows for only one mass, or mass to charge ratio, to enter the photoelectron spectrometer.

After exiting the mass gate, ions enter the momentum decelerator (Figure II.15 – Region 4). In order to minimize doppler broadening and thus maximize photoelectron resolution the ions must be decelerated.[24] The momentum decelerator consists of 10 grids connected

by a resistor chain. Ions enter the decelerator and then a large positive pulse, +3000 V, is applied to the decelerators front plate.[25] This pulse is on for several hundred nanoseconds and then pulsed back to ground. This yields a decelerated ion packet that travels into the interaction region.

II.3 PHOTOELECTRON SPECTROMETER

The electron energy analyzer on this instrument is a magnetic bottle. The magnetic bottle is a time-of-flight based electron kinetic energy analyzer. Ions are isolated and decelerated into the center of the magnetic bottle's interaction region. Once in the interaction region (Figure II.14 – Region 4), defined by the crossing of the ion and laser beam, these ions are photodetached by a pulsed laser. These electrons are born in a bottle shaped inhomogeneous magnetic field, the field is strong at the interaction point with a gradual decrease to a lower field that then extends towards the detector.[26, 27, 24] This causes electrons born at this point to travel from areas of high magnetic field towards areas of lower field thus funneling them towards the detector. In practice, this field is generated through the overlap of two separate fields. The field near the interaction region is generated by a strong permanent magnet with a conical tip pointing towards the detector. The less intense guiding field is generated by a solenoid that surrounds the flight tube that electrons traverse on their way to the MCP detector. Based on their flight time, known mass, and fixed distance to the detector their kinetic energy can be determined. Using the known photon energy of the photodetachment laser, the binding energy to the molecule or cluster can then be calculated using Equation 1. This anion photoelectron spectrometer is calibrated from the known atomic transitions of copper, gold and iodine.

II.3.1 Light Baffle

In order to increase the signal to noise ratio for the photoelectron spectrometer and to extend its useable range for non-metals to 266 nm and 193 nm, a new light baffle was constructed and installed. The principle source of noise in the photoelectron spectrometer is stray high energy photons, higher than the work function of the material, striking surfaces within the interaction region and generating electrons. In order to limit the generation of these electrons, the light baffle was redesigned to further limit stray photons from entering the interaction region.

The new light baffle consists of two sections, one input and one output section. Each section contains three 0.18" apertures. Each assembly, input and output, is 18" long and the apertures are equally spaced along their length. This arrangement allows for a significant reduction in stray light as photons must pass straight through these three apertures and are unlikely to be reflected by the internal surfaces into the interaction region. In order to minimize any reflections off the internal walls of the baffle, the internal tubes holding the middle spacer were designed to maximize the ID of surfaces inside the light baffle. The apertures and spacing tube were fabricated from stainless steel (spacers – S.S.316L, apertures – S.S.304). In order to further minimize reflections, the apertures and internal surfaces of the light baffle are coated with graphite (Electrodag 154). These two assemblies are mounted opposite one another and aligned to one another using an optical telescope across the interaction region.

References

1. Duncan, M. A. *Rev. Sci. Instrum.* **83**.4 (2012): 041101.

2. Siekmann, H., Lüder, C., Faehrmann, J., Lutz, H., Meiwes-Broer, K *Z. Phys. D Atom Mol. Cl.* **20**.1 (1991): 417-20.

3. Ganteför, G., Siekmann, H., Lutz, H. O., and Meiwes-Broer, K.-H. *Chem. Phys. Lett.* **165**.4 (1990): 293-96.

4. Yamashita, M., and Fenn, J. B. *J. Phys. Chem.* **88**.20 (1984): 4451-59.

5. Kebarle, P., and Tang, L. *Anal. Chem.* **65**.22 (1993): 972A-86A.

6. Fenn, J. B., Mann, M., Meng, C. K., Wong, S. F., and Whitehouse, C. M. *Mass Spectrom. Rev.* **9**.1 (1990): 37-70.

7. Fenn, J. B., Mann, M., Meng, C. K., Wong, S. F., and Whitehouse, C. M. *Science* **246**.4926 (1989): 64-71.

8. Wang, X.-B., and Wang, L.-S. *Rev. Sci. Instrum.* **79**.7 (2008): 073108.

9. Kamrath, M. Z., Relph, R. A., Guasco, T. L., Leavitt, C. M., and Johnson, M. A. *Int. J. Mass. Spectrom.* **300**.2-3 (2011): 91-98.

10. Wang, L.-S., Ding, C.-F., Wang, X.-B., and Barlow, S *Rev. Sci. Instrum.* **70**.4 (1999): 1957-66.

11. Jones, R. M., Gerlich, D., and Anderson, S. L. *Rev. Sci. Instrum.* **68**.9 (1997): 3357-62.

12. Jones, R. M., and Anderson, S. L. *Rev. Sci. Instrum.* **71**.11 (2000): 4335-37.

13. Gerlich, D. *Adv. Chem. Phys.* **82** (1992): 1-176.

14. Dawson, P. H.: Elsevier, 2013. Print.

15. Tosi, P., Fontana, G., Longano, S., Bassi, D *Int. J. Mass. Spectrom.* **93**.1 (1989): 95-105.

16. Tolmachev, A., Chernushevich, I., Dodonov, A., Standing, K *Nucl. Instrum. Methods Phys. Res. B* **124**.1 (1997): 112-19.

17. Chernushevich, I. V., and Thomson, B. A. *Anal. Chem.* **76**.6 (2004): 1754-60.

18. Zeman, H. *Rev. Sci. Instrum.* **48**.8 (1977): 1079-85.

19. Mahaffy, P., Lai, K. *J. Vac. Sci. Technol.* **8**.4 (1990): 3244-46.

20. Paul, W., and Steinwedel, H. *Z. Naturforsch. A* **8**.7 (1953): 448-50.

21. Marsh, B. M., Voss, J. M., and Garand, E. *J. Chem. Phys.* **143**.20 (2015): 204201.

22. Wiley, W., and McLaren, I. H *Rev. Sci. Instrum.* **26**.12 (1955): 1150-57.

23. de Heer, W. A., and Milani, P *Rev. Sci. Instrum.*. **62**.3 (1991): 670-77.

24. Cheshnovsky, O., Yang, S., Pettiette, C., Craycraft, M., Smalley R. *Rev. Sci. Instrum.* **58**.11 (1987): 2131-37.

25. Wang, L. S., Cheng, H. S., and Fan, J. *J. Chem. Phys.* **102**.24 (1995): 9480-93.

26. Kruit, P., and Read, F. *Meas. Sci. Technol.* **16**.4 (1983): 313.

27. Cheshnovsky, O., Yang, S., Pettiette, C., Craycraft, M., Liu, Y., and Smalley, R. *Chem. Phys. Lett.* **138**.2-3 (1987): 119-24.

Chapter III: $Mg(NH3)_{4-6}$ Triple Rydberg Anions

Evan Collins, Gaoxiang Liu, Sandy Ciborowski, Mary Marshall, Zhaoguo Zhu, Chalynette Martinez-Martinez, Kit H. Bowen,

Department of Chemistry, Johns Hopkins University, Baltimore, Maryland 21218, USA

J.V. Ortiz

Department of Chemistry and Biochemistry, Auburn University, Auburn, AL 36849, USA

III.1. INTRODUCTION

A range of species have been discovered with hydrogenic electrons that are Rydberg like surrounding a positively charged core. Rydberg radicals are neutral species with a radical Rydberg electron that are stable only in their excited states[1]. Double Rydberg anions consist of a singly charged positive core and two Rydberg type electrons denoted at $(X^+)^=$.[2] In addition the positively charged core of a double Rydberg anion is a closed shell stable cation.[3] The extension of this to a negative ion with three Rydberg like electrons would be called a triple Rydberg anions. A triple Rydberg anion would be an ion composed of a divalent positive core surrounded by three Rydberg like outer electrons.

Herzberg discovered the first Rydberg radical H_3 and shortly after the NH_4 radical.[4] The rational for their formation is the high stability of their cationic core. The first double Rydberg anion discovered was NH_4^- or more appropriately $(NH_4^+)^{=}$.[5] This species was discovered while taking the photoelectron spectra of $H^-(NH_3)$ after the identification of a low binding energy peak in the photoelectron spectra which varied in intensity over time relative to the $H^-(NH_3)$ peak. In addition to its low binding energy, the peak itself was very narrow suggesting a high Franck-Condon overlap. Based on these observations this

peak was found not to originate from $H^-(NH_3)$, and instead was identified as a signature of tetrahedral NH_4^- based on previous calculations by Ortiz and others showing it was a stable anion geometry.[6-10]

Further investigation of this peak as well as additional photoelectron spectra of the series $(N_nH_{3n+1})^-$ showed that n = 1-7 were also double Rydberg anions.[2, 11] Calculations from Ortiz furthered these claims.[12] Consistent low binding energy peaks are seen between 0.415 eV and 0.472 eV for each cluster in the series. These lowest electron binding energy (EBE) peaks are characteristic peaks seen in double Rydberg anions and originate from the Rydberg type electrons surrounding the positive core. Analyzing spectra from across this series of double Rydberg anions, this lowest binding energy peak is relatively unaffected by the addition of ammonia molecules as the binding energy is relatively constant over this range. In addition, the valence peak from solvated $H^-(NH_3)_n$ shows a solvation effect across the series, the peak shifts to higher EBE with increasing n, while the main double Rydberg anion peak does not. Solvated double Rydberg peaks are seen in addition to the principle double Rydberg peak, however they are shifted to higher EBE relative to the low EBE double Rydberg peak.

Analogous to a double Rydberg anion, a triple Rydberg anion would consist of a 2+ core surrounded by three weakly bound electrons. Similar to a double Rydberg anion, these three electrons would be delocalized from the 2+ core and relatively unaffected by the changes to this divalent core. Initial calculations by Ortiz indicated that $Mg(NH_3)_4^-$ might be a potential triple Rydberg anion. $Mg(NH_3)_4^{++}$ has also been previously observed in the gas phase indicating it might be stable enough to act as a core to form the triple Rydberg

anion. [13] In addition photoionization and theoretical calculations for neutral $Mg(NH_3)_n$ clusters have been reported.[14]

Here we report the discovery of a series of triple Rydberg anions, $Mg(NH3)_{4-6}$. We present photoelectron spectra of this cluster series and assign vertical detachment energies to the collected spectra.

III.2. EXPERIMENTAL

Helium carrier gas with a trace amount of ammonia mixed in was pulsed over a rotating magnesium rod. After a delay, the rod was ablated with 532 nm photons the 2nd harmonic of a Nd:YAG laser (10 Hz). This plasma mixed in the housing with the ammonia seeded He carrier gas then cooled generating the clusters of interest.

Anion photoelectron spectroscopy is conducted by crossing a mass-selected packet of negative ions with a fixed frequency photon beam and energy-analyzing the resultant photodetached electrons. These photoelectrons are governed by the energy-conserving relationship, $\nu = EBE + EKE$, where $h\nu$ is the photon energy, EBE is the electron binding energy, and EKE is the measured electron kinetic energy. The apparatus consists of a laser vaporization ion source, a time of flight mass spectrometer, and an anion photoelectron spectrometer. The anion photoelectron spectrometer is equipped with a magnetic bottle electron energy analyzer and an Nd:YAG laser. The magnetic bottle has a resolution of 50 meV at an EKE of 1 ev. These spectra were collected with the 3rd harmonic of the Nd:YAG, 335 nm (3.49 eV) photons. The anion spectrometer was calibrated against the transitions of Cu^-.

III.3. RESULTS

The mass spectrum of the cluster series is shown in Figure III.1. The series $Mg(NH_3)_{4\text{-}6}^-$ is clearly seen. A clean isotope pattern was obtained for n = 5 & 6, however for $Mg(NH_3)_4^-$ the isotope pattern is convoluted with an unknown contaminant and was also present in the photoelectron spectra. The isotope pattern for $Mg(NH_3)_4^-$ consists of four isotopes (92, 93, 94, 95 amu), three of which are of significant intensity to photodetach (92, 93 & 94 amu). Based on the relative intensities of these peaks and the expected isotope pattern, the 94 amu isotope was found to be pure $Mg(NH_3)_4^-$. For $Mg(NH_3)_4^-$ the 94 amu isotope was photodetached.

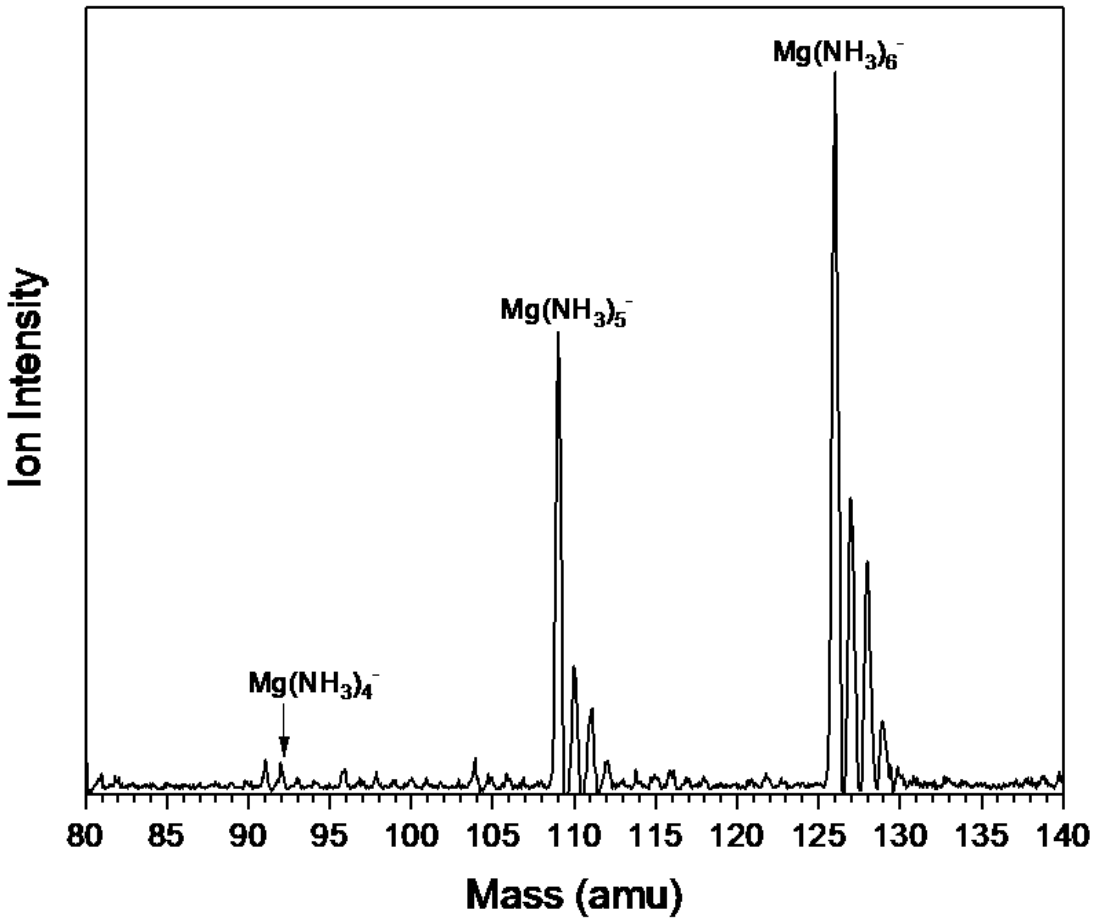

Figure III.1: Mass spectra of the $Mg(NH_3)_{4\text{-}6}$ series.

The photoelectron spectra for $Mg(NH_3)_n^-$ n = 4 -6 is shown in Figure III.2. A low binding energy peak appears in each spectrum. This peak has a VDE of 0.56 eV for $Mg(NH_3)_4^-$ and 0.58 eV for $Mg(NH_3)_5^-$ and $Mg(NH_3)_6^-$. In addition, there is a second low binding energy peak observed in the spectra across the series at 1.12 eV for n =4, 1.11 eV for n = 5 and 1.09 eV for n = 6. In each of the species, higher binding energy peaks are also present. The VDEs for the $Mg(NH_3)^-_{4\text{-}6}$ series are presented in Table III.1.

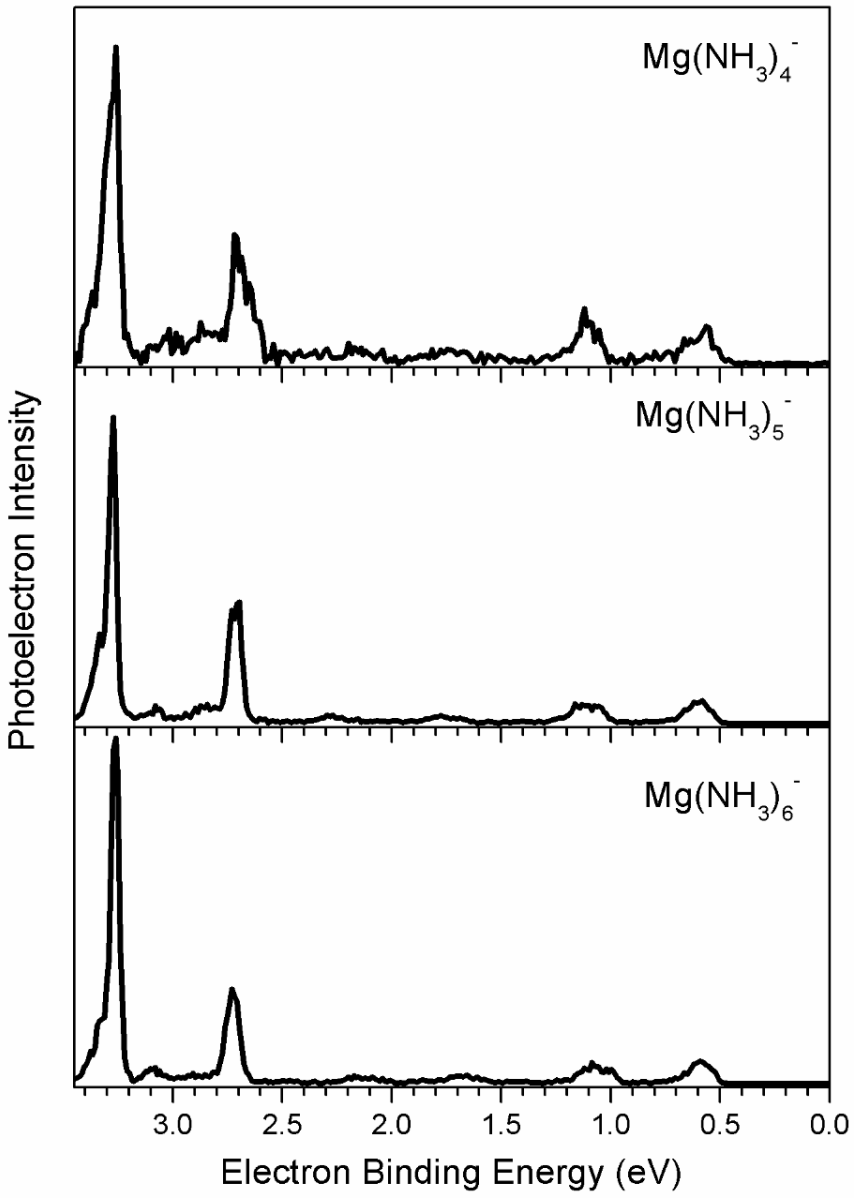

Figure III.2: Photoelectron spectra of the $Mg(NH_3)_{4\text{-}6}$ series.

Table III.1: Summary of experimentally observed VDEs for the $Mg(NH_3)_{4-6}$ series

	VDE 1 (eV)	VDE 2 (eV)	VDE 3 (eV)	VDE 4 (eV)
$Mg(NH3)_4^-$	0.56	1.12	2.72	3.26
$Mg(NH3)_5^-$	0.58	1.11	2.7	3.27
$Mg(NH3)_6^-$	0.58	1.09	2.73	3.26

III.4. DISCUSSION

Analyzing the photoelectron spectra in Figure III.3, several similarities to the double Rydberg anion system $(N_nH_{3n+1})^-$ for n = 1-7. These spectra for $Mg(NH_3)^-_{4-6}$ exhibit a low binding energy peak VDE between 0.56 eV and 0.58 eV. For the ammonia double Rydberg series this peak is seen between 0.472 eV and 0.415 eV. This indicates that these double and triple Rydberg anions both have similarly delocalized and diffuse states.

The lowest binding energy peak in both systems remains relatively unshifted as more ammonia units are added. This seems to indicate that electrons occupying these states are delocalized, as their binding energy is unaffected by changes to the composition and thus structure of the anion. It follows that this behavior observed in double Rydberg anion systems would also occur in triple Rydberg anion systems. In $Mg(NH_3)^-_{4-6}$ a second set of low binding energy peaks follows the same trend. The VDEs for these peaks in the spectra for $Mg(NH_3)^-_{4-6,}$ fall between 1.09 eV and 1.12 eV.

Preliminary calculations from Ortiz on $Mg(NH_3)_6^-$ indicate that the first three lowest binding energy peaks are likely from the triple Rydberg anion species. Ortiz has calculated that the first, second, and third peaks VDE should be 0.66 eV, 0.88 eV, and 1.54 eV respectively. The first peak matches well with the collected photoelectron

spectra. The next two VDEs differ from the observed peak by 0.1 – 0.2 eV. Ortiz is currently improving his calculations.

The intense higher binding energy peaks seen in $Mg(NH_3)^-_{4\text{-}6}$ at ~2.70 eV and ~3.26 eV are likely not from diffuse electrons from the triple Rydberg anion. Due to the high binding energy, it's unlikely these are electrons from the $Mg(NH_3)_n^{++}$ core. It's possible that these peaks originate from transitions from neutral $Mg(NH_3)_4$ as well as direct detachment from the anion to the cation.

A combined experimental and theoretical study on neutral $Mg(NH_3)_n$ reports the experimentally determined ionization energy (IE) for a range of clusters in this series and calculated IEs for a range of structures for each cluster.[14] For $Mg(NH_3)_4$ the experimental IE reported is 3.9 eV, and agrees with the calculation for a structure with two ammonia molecules within the first solvation shell and two in the outer shell.[14] However, the calculated structure for tetrahedral $Mg(NH_3)_4$ shows a theoretical vertical IE of 2.83 eV.[14] Assuming this calculation is reasonably accurate and the triple Rydberg anion $Mg(NH_3)_4^-$ has a tetrahedral structure, as in the double Rydberg anion NH_4^-, the photon energy used in this experiment would allow for both ionization of the neutral as well as direct detachment from the anion to the cation surface. This would explain the two intense high binding energy peaks observed at ~2.72 eV and ~3.26 eV in our spectra.

The ~2.72 eV electron binding energy (EBE) peak could originate from a two-photon process from the ionization of neutrals generated from photodetachment of the anion. This would be a two-photon process generating one electron with a binding energy of 2.72 eV. The spacing between the 2.72 eV and 3.26 eV is 0.54 eV is about the binding energy of the first electron observed in the spectrum 0.56 eV for $Mg(NH_3)_4^-$. Assuming

the 2.72 eV peak is from ionization of the neutral, this peak at 3.26 eV could be from direct detachment from the anion to the cation surface. This would be a one photon process generating two electrons with a binding energy of 3.26 eV. A qualitative potential energy diagram presenting this explanation is presented in Figure III.3 and an annotated spectrum in Figure III.4. In order to validate this theory we await Ortiz's calculations.

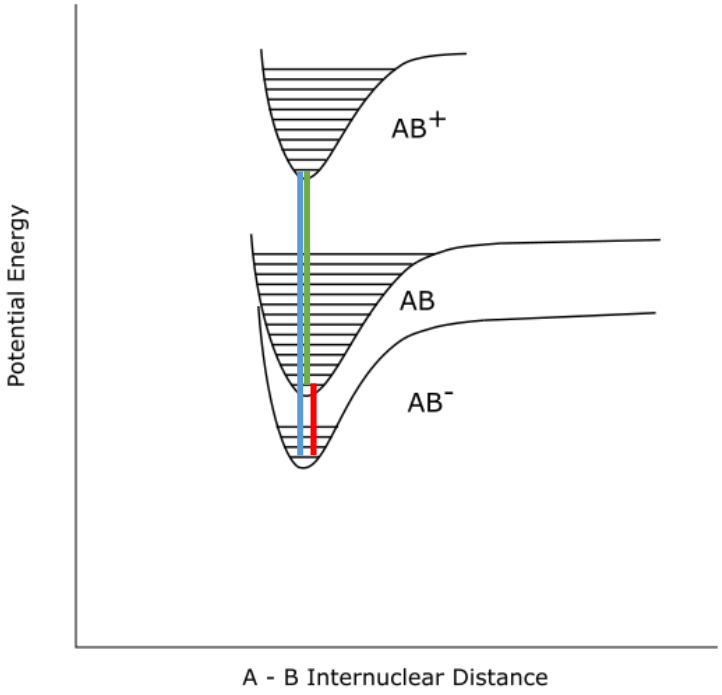

Figure III.3: Qualitative potential energy diagram showing possible origins of higher binding energy peaks observed in $Mg(NH_3)^-_4$. AB^- is the ground state anion, AB is the ground state neutral, and AB^+ is the cation. The red line denotes the transition from the anion to the neutral observed at 0.56 eV. The green line denotes the vertical ionization of the neutral, which could correspond to the peak observed at 2.72 eV. The blue line denotes the transition directly from the anion to the cation surface.

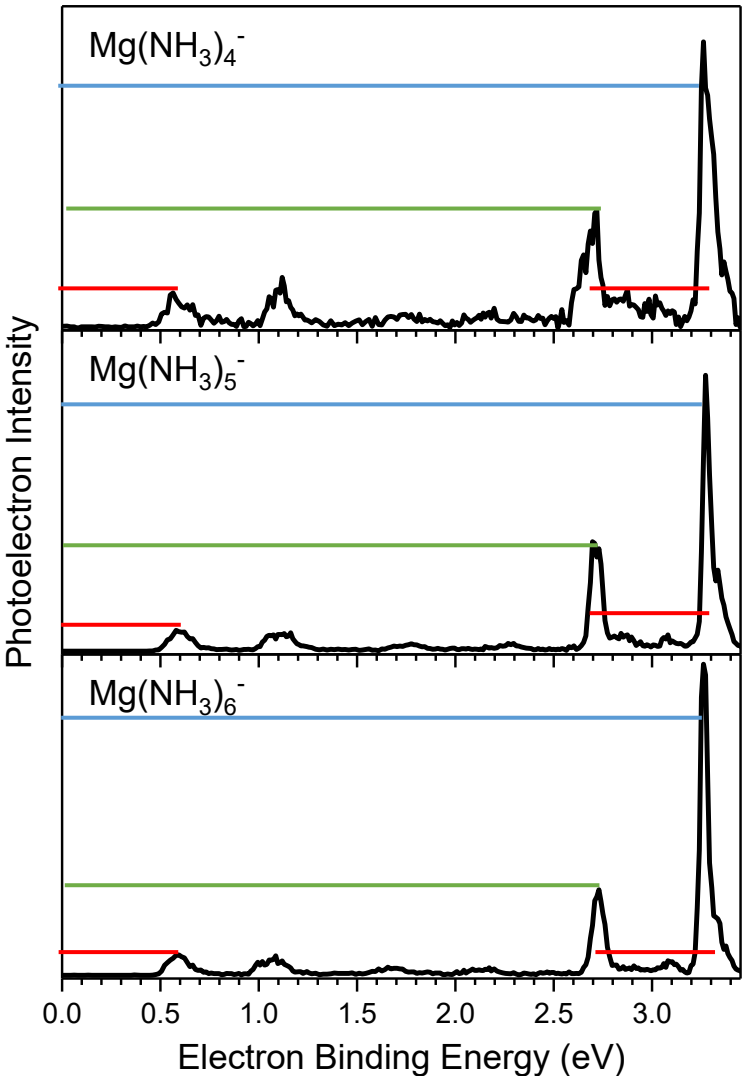

Figure III.4: Photoelectron spectra of $Mg(NH_3)^-_{4-6}$ annotated with lines correlating to transitions shown in Figure III.3. The red line is the VDE of the lowest EBE peak, likely originating from detachment of a diffuse electron. The green line denotes the transition potentially from ionization of the neutral. The blue line denotes the transition that may be from direct detachment from the anion to the cation surface. As can be seen in the diagram the peak from the blue transition and green transition are spaced by the red transition.

References

1. Velasco, A., Lavin, C., Martin, I., Melin, J., and Ortiz, J.V. *J. Chem. Phys.* **131**.2 (2009): 024104.

2. Xu, S.-J., Nilles, J., Hendricks, J., Lyapustina, S., and Bowen, K. *J. Chem. Phys.* **117**.12 (2002): 5742-47.

3. Hopper, H., Lococo, M., Dolgounitcheva, O., Zakrzewski, V., and Ortiz, J.V. *J. Am. Chem. Soc.* **122**.51 (2000): 12813-18.

4. Herzberg, G. *Faraday Discuss. Chem. Soc.* **71** (1981): 165-73.

5. Coe, J. V., Snodgrass, J., Freidhoff, C., McHugh, K., and Bowen, K. *J. Chem. Phys.* **83**.6 (1985): 3169-70.

6. Cardy, H., Larrieu, C., and Dargelos, A. *Chem. Phys. Lett.* **131**.6 (1986): 507-12.

7. Cremer, D., and Kraka, E. *J. Phys. Chem.* **90**.1 (1986): 33-40.

8. Gutowski, M., Simons, J., Hernandez, R., and Taylor, H. L. *J. Phys. Chem.* **92**.22 (1988): 6179-82.

9. Hirao, K., and Kawai, E. *J. Mol. Struct.* **149**.3-4 (1987): 391-94.

10. Ortiz, J.V. *J. Chem. Phys.* **87**.6 (1987): 3557-62.

11. Radisic, D., Stokes, S. T., and Bowen, K. *J. Chem. Phys.* **123**.1 (2005): 011101

12. Ortiz, J. V. *J. Chem. Phys.* **117**.12 (2002): 5748-56.

13. Wu, B., Duncombe, B. J., and Stace, A. J. *J. Phys. Chem. A* **110**.27 (2006): 8423-32.

14. Elhanine, M., Dukan, L., Maître, P., Breckenridge, W., Massick, S., and Soep, B. *J. Chem. Phys.*. **112**.24 (2000): 10912-25.

Chapter IV: Importance of Time Scale and Local Environment in Electron-Driven Proton Transfer. The Anion of Acetoacetic Acid

Angela Buonaugurio, Evan Collins, Xinxing Zhang, Jeremy Erb, Thomas Lectka, Kit H. Bowen

Department of Chemistry, Johns Hopkins University, Baltimore, Maryland 21218, USA

Zibo G. Keolopile

Department of Physics, University of Botswana, Private Bag 0022, Gaborone, Botswana

Maciej Gutowski

Institute of Chemical Sciences, School of Engineering and Physical Sciences, Heriot-Watt University, Edinburgh EH14 4AS, United Kingdom

Michael Allan

Department of Chemistry, University of Fribourg, chemin du Musée 9, Fribourg 1700, Switzerland

ABSTRACT

Anion photoelectron spectroscopy (PES) and electron energy-loss spectroscopy (EELS) probe different regions of the anionic potential energy surface. These complementary techniques provided information about anionic states of acetoacetic acid (AA). Electronic structure calculations facilitated the identification of the most stable tautomers and conformers for both neutral and anionic AA and determined their relative stabilities and excess electron binding energies. The most stable conformers of the neutral keto and enol tautomers differ by less than 1 kcal/mol in terms of electronic energies corrected for zero-point vibrations. Thermal effects favor these conformers of the keto tautomer, which do

not support an intramolecular hydrogen bond between the keto and the carboxylic groups. The valence anion displays a distinct minimum which results from proton transfer from the carboxylic to the keto group; thus, we name it an ol structure. The minimum is characterized by a short intramolecular hydrogen bond, a significant electron vertical detachment energy of 2.38 eV, but a modest adiabatic electron affinity of 0.33 eV. The valence anion was identified in the anion PES experiments, and the measured electron vertical detachment energy of 2.30 eV is in good agreement with our computational prediction. We conclude that binding an excess electron in a π^* valence orbital changes the localization of a proton in the fully relaxed structure of the AA^- anion. The results of EELS experiments do not provide evidence for an ultrarapid proton transfer in the lowest π^* resonance of AA^-, which would be capable of competing with electron autodetachment. This observation is consistent with our computational results, indicating that major gas-phase conformers and tautomers of neutral AA do not support the intramolecular hydrogen bond that would facilitate ultrarapid proton transfer and formation of the ol valence anion. This is confirmed by our vibrational EELS spectrum. Anions formed by vertical electron attachment to dominant neutrals undergo electron autodetachment with or without vibrational excitations but are unable to relax to the ol structure on a time scale fast enough to compete with autodetachment.

IV.1 INTRODUCTION

Proton motion coupled with electron transfer was identified long ago as the basic mechanism of bioenergetic conversion.[1] An extensive study of this class of reactions has recently been motivated by their importance in biological systems, e.g., damage of DNA and RNA by low-energy electrons involved in cancer radiotherapy,[2,3] protein redox

machines including photosystem II and ribonucleotide reductase.[4] There is also technological relevance in conversion and storage of solar energy through activation of small molecules such as water, methanol, and CO_2.[5] Finally, fabrication of micro-and nanoelectromechanical devices through electron beam lithography hinges on fundamental electron-driven processes.[6] A special subcategory of proton-coupled electron transfer is excess electron-induced proton transfer.[3,7]

Although gas-phase studies of excess electron-induced proton transfer in DNA and proteins are challenging because of the low vapor pressures of these molecules,[3,8] this difficulty has been significantly reduced in the cases of subunits of DNA, e.g.,

base pairs, nucleosides, and nucleotides, by the development of specialized, laser desorption/photoemission anion sources for bringing them into the gas phase as intact anions.[9–11] Nevertheless, it is still valuable to identify smaller model systems with greater vapor pressures, so that the fundamental chemical and physical aspects of (excess) electron-induced proton transfer can be studied.

Previously, we suggested that the dimer of formic acid might serve as a model system for intermolecular proton transfer induced by a π^* excess electron.[12] It displays many similarities with intermolecular proton transfer in anionic complexes of nucleic acid bases with weak acids.[13–15] Similarly, hydrogen-bonded complexes of ammonia and hydrogen halides served as model systems for intermolecular proton transfer induced by a σ excess electron.[16,17]

The electron-induced proton transfer in the formic acid dimer (Figure 1, top row) is manifested also by the differences of the results of electron energy-loss spectroscopy

(EELS) experiments on the monomer and dimer of formic acid.[18] The yield of very low energy electrons was found to be 20 times stronger in the dimer than in the monomer. The dramatic increase in the efficiency of the dimer to quasi-thermalize electrons arriving in the 1−2 eV energy range and captured in the lowest π* shape resonance was interpreted in terms of rapid intermolecular proton transfer that quenches the fast autodetachment channel. It was concluded that the phenomenon of electron-driven proton transfer can be ubiquitous and that it may be responsible for rapid slowing down of excess electrons.

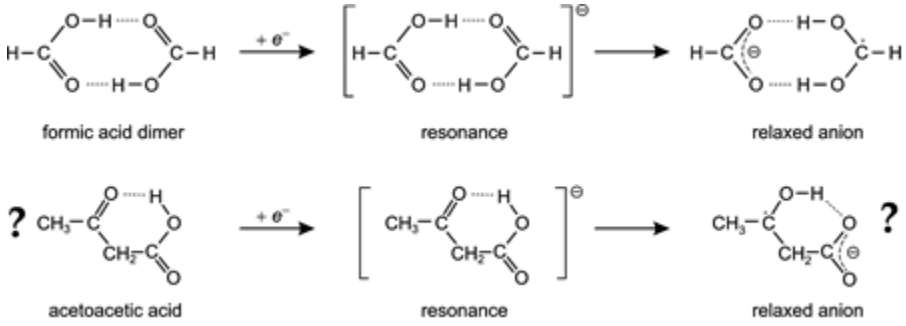

Figure IV.1: Electron-induced intermolecular proton transfer in the formic acid dimer[12,18,19] (top), and the hypothesized intramolecular proton transfer in the keto tautomer of acetoacetic acid (bottom). The feasibility of the latter process will be explored in this study for the tautomers of acetoacetic acid. On the basis of the formic acid results[18] we expect that the vertical electron attachment leads to a (shape) resonance, with the excess electron in the lowest π* orbital, which can then relax by an ultrarapid proton transfer, in competition with the very fast spontaneous electron detachment.

The relaxed anion of the formic acid dimer has now been experimentally characterized using Ar-tagged vibrational predissociation and electron autodetachment spectroscopies as well as anion photoelectron spectroscopy.[19] These results confirmed that excess electron attachment leads to a transfer of one of the protons across the H-bonded bridge. The study corroborated that the relaxed anion of formic acid dimer is composed of a largely intact formate anion attached to the dihydroxymethyl radical through a symmetrical, double O−H bonded bridge, see the top of Figure IV.1.

Much less information is available on intramolecular proton transfer induced by an excess electron, and the results are available primarily for low-vapor pressure molecules, e.g., nucleotides.[20] For example, the anion photoelectron spectrum of 2′-deoxyadenosine-5′-monophosphate[20] has been interpreted through intramolecular proton transfer from a hydroxyl group of the phosphate to the N3 position of the adenine.[21]

Here, we present computational and experimental results on neutral and anionic acetoacetic acid (AA), see Figure IV.1 (bottom row). Acetoacetic acid is the simplest beta-keto acid and is thermodynamically unstable with respect to the decomposition to acetone and CO2. However, an experimental half-life of 140 min has been reported for a water solution of AA at 37 °C.[22] Thus, the molecule can be probed experimentally provided care is taken to operate at low temperatures. Some computational information is available on the ketonic decarboxylation of AA.[23−25]

AA can exist in both the keto and the enol forms (labeled K and E here).[25,26] The keto−enol equilibrium was found to be strongly solvent dependent, with the keto form dominant in polar solvents. On the basis of ^{1}H NMR spectra it was suggested that a conformer of the keto form with an intramolecular hydrogen bond (K1 in Figure IV.2) is not dominant under any conditions, though keto tautomers dominate in polar solvents.[26] It was also suggested that an enol tautomer is present in less polar solvents, and it certainly exists as an internally hydrogen-bonded conformer, like E1. The enolization of the ketone group was found to be more favorable than the enolization of the carboxylic group by 11.3 kcal/mol at the MP2 level of theory.[25] Thus, our further discussion is focused on the keto and ketone enol tautomers, see Figure IV.2.

In this study, we explore AA in the gas phase and probe whether its keto and enol tautomers undergo intramolecular proton transfer driven by an excess electron attachment

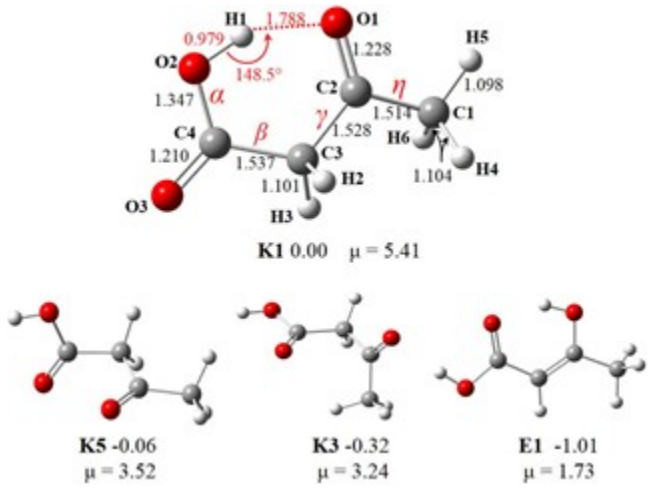

Figure IV.2: Molecular structures of neutral AA considered in this study. The relative CCSD(T)/ADZ energies corrected for MP2/ADZ zero-point energies (kcal/mol). Principal geometrical parameters (in Angstroms and degrees) were characterized at the CCSD/ADZ+DF level of theory. Bonds α, β, γ, η, and ε were rotated for conformational searches. Dipole moments, μ, determined at the CCSD level, are in Debyes

(Figures IV.1 (bottom) and IV.3). Upon formation of a suitable conformer, an intramolecular hydrogen bond might provide a bridge for ultrafast proton transfer. We use electronic structure methods to identify the most stable conformers of the keto and enol tautomers and to characterize the bound anionic states of AA, both valence and dipole bound. Anion photoelectron spectroscopy (PES) measurements probe the bound and relaxed anionic states of AA^- and test computational predictions. EELS measurements provide both vertical electron attachment energies for the (unrelaxed) π* states (resonances) of AA^- and the vibrational spectrum of neutral AA. On the basis of past experience with the dimer of formic acid,[18] particular attention is paid to the possibility of quasithermalization of electrons captured in the lowest π* shape resonance, indicative of an ultrarapid proton transfer.

IV.2 COMPUTATIONAL METHODS

The keto and enol tautomers and conformers of neutral AA as well as the valence-bound anion (Figures IV.2 and IV.3) were explored using our inhouse potential energy surface

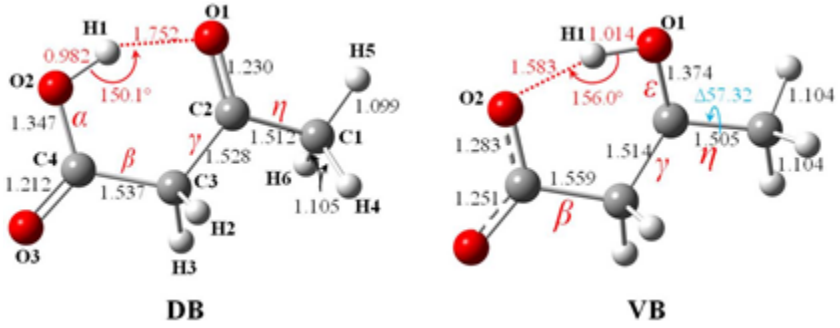

Figure IV.3: Molecular structures of valence-bound (VB) and dipole-bound (DB) anions of AA, considered in this study. Principal geometrical parameters (in Angstroms and degrees) were characterized at the CCSD/ADZ+DF level of theory. Bonds α, β, γ, η, and ε were rotated for conformational searches. The change, Δ, in the O1−C2−C1−H5 dihedral angle (blue) from the neutral K1 to the valence anion geometry is in degrees.

scanning tool (PESST).[27] When probing the conformational space of keto, the bond α was rotated with a step size of 180°. The bonds β and γ were rotated with a step size of 60°. The probed initial η values were 0° and 60°. All combinations of these rotatable bonds α, β, γ, and η resulted in 144 initial structures for screening purposes. Similarly, when probing the conformational space of enol, the bond γ was rotated with a step size of 60°. The bonds β, α, and ε were rotated with a step size of 180°. All combinations of these rotatable bonds resulted in 48 initial structures for screening purposes. The valence anion of AA favors the ol structure. When probing its conformational space, γ and ε were rotated with a step size of 60° and 180°, respectively. The initial β values were 0° and 90°, while those for η were 0° and 60°, yielding 42 initial structures.

We used the standard Dunning's aug-cc-pVDZ (ADZ)[28,29] basis set supplemented with extra low-exponent basis functions centered on the carbon of (−CH3) to describe the

diffuse charge distribution in the anionic dipole-bound state. The exponents αn of these basis functions were determined through $\alpha n = \alpha 0/q^n$, n = 1, 2, ..., initiated from the lowest exponent α0 of the s, p,or d functions in the standard ADZ basis set and advanced with q = 3.2.[30] We limited the extra diffuse set to 5 s,5 p, and 2 d functions.[31,32] We will use a label DF for these additional diffuse functions and ADZ+DF for the combined basis set.

The initial structures were prescreened at the density functional level of theory with the B3LYP exchange-correlation functional.[33–36] The minima contained within an energy range of 10 kcal/mol were reoptimized at the coupled-cluster singles and doubles (CCSD)[37] level of theory. Harmonic frequencies were routinely calculated at the MP2 level and for the most stable systems also at the CCSD level. The most accurate electronic energies were obtained at the coupled-cluster level with single, double, and noniterative triple excitations (CCSD(T)).[38] The Gibbs energies were based on the coupled cluster electronic energies corrected for zero-point vibration energies, thermal contributions to energy, pV terms, and entropy terms. These terms were calculated in the rigid rotor-harmonic oscillator approximation for T = 298 K and p = 1 atm. We also characterized barriers separating low-lying conformers of the neutral keto AA.

The vertical excess electron binding energies were calculated in two ways. In “indirect” approaches, the energy of the anion was subtracted from the energy of the neutral, and the procedure was executed at the SCF, MP2, CCSD, and CCSD(T) levels of theory. The vertical excess electron binding energy can be also calculated “directly”. Here we used the electron propagator theory (EPT) method with the P3 propagator[39] applicable to both electron detachment and attachment processes. We will use the term EPT (third) to refer

to the third-order electron binding energies. One can calculate the excess electron vertical binding energy as either the electron affinity (EA) of the neutral or the ionization potential (IP) of the anion.

The dipole-and valence-bound anions have minima corresponding to quite different molecular structures. The former results from a minor distortion of the neutral K1 keto, but the latter is better described as a conformer of the ol tautomer (Figure IV.3). Henceforth we will use DB and VB to refer to the dipole-and valence-bound anions, respectively. In order to illustrate the evolution of the DB and VB anionic states as a function of intramolecular proton transfer, we constructed a linear synchronous path, see eq S1 in the Supporting Information.

The energy of the anion M^- at a geometry G can be written as

$$E_M - (G) = E_M(G_M) + \Delta E_M(G) - EBE(G) \qquad \text{(Equation 1)}$$

where $E_M(G_M)$ is the energy of the neutral M at its optimal geometry G_M

$$\Delta E_M(G) = E_M(G) - E_M(G_M) \qquad \text{(Equation 2)}$$

represents an increase of the energy of the neutral M associated with its geometrical deformation from G_M to G, and EBE(G) is the vertical electron binding energy at the geometry G

$$EBE(G) = E_M(G) - E_M - (G) \qquad \text{(Equation 3)}$$

The values of EBE are positive for vertically bound anionic states and negative for resonances. The vertical electron affinity (VEA) is equivalent to $EBE(G_M)$. The vertical

detachment energy (VDE) is equivalent to EBE(G_{M^-}), and the electronic part of the adiabatic electron affinity is defined as

$$\mathrm{AEA} = \mathrm{E_M(G_M)} - \mathrm{E_{M^-}(G_{M^-})} \qquad \text{(Equation 4)}$$

where G_{M^-} the optimal geometry of the anion of M. Notice that

$$\mathrm{AEA} = -\Delta\mathrm{E_M(G_{M^-})} + \mathrm{EBE(G_{M^-})} = -\Delta\mathrm{E_M(G_{M^-})} + \mathrm{VDE} \qquad \text{(Equation 5)}$$

Further extensions of this notation are needed for G_{M^-}, as the anion might be either valence or dipole bound. In addition to G_M we will consider $G_{M^-_{dbs}}$ and $G_{M^-_{VB}}$, which are the lowest energy structures for the dipole-and valence-bound anions, respectively. We will also consider a quantity

$$\Delta\mathrm{E_{VB\rightarrow dbs}} = \mathrm{E_{M^-_{dbs}}}\left(\mathrm{G_{M^-_{VB}}}\right) - \mathrm{E_{M^-_{VB}}}\left(\mathrm{G_{M^-_{VB}}}\right) \qquad \text{(Equation 6)}$$

which is the vertical excitation energy from the valence-to the dipole-bound anion at the optimal valence anion geometry.

All electronic structure calculations reported in this study were performed with the Gaussian 2009 package.[40] The orbitals occupied by an excess electron were generated with the Visual Molecular Dynamics[41] package, and the contour values used in the plots were calculated with the OpenCubeMan[42] tool using a fraction of electron (Fe) density equal to 0.6. The GaussView[43] package was used to draw molecular structures.

IV.3 EXPERIMENTAL METHODS

IV.3.1 Synthesis of Acetoacetic Acid.

Our synthesis followed the protocol described in ref 44. Sodium hydroxide (0.16 mol) was added to aqueous ethyl acetoacetate (0.15 mol) on ice. The reaction was stirred and

allowed to react overnight. The resulting solution was saturated with ammonium sulfate. Sulfuric acid was then used to acidify the solution. The solution was extracted three times with diethyl ether (200 mL) and dried over magnesium sulfate. After removing the ether using a rotary evaporator and drying using a rotary vacuum pump, a yellowish gel of acetoacetic acid was obtained. Since batches of acetoacetic acid were readily subject to decomposition, care was taken to ensure that the solutions did not become warmer than 30 °C, and they were utilized in PES and EELS experiments as quickly as possible.

IV.3.2. Photoelectron Spectroscopy.

Anions of acetoacetic acid were generated by two different sources and their photoelectron spectra measured on two different types of anion photoelectron spectrometers. In one case, they were produced with a nozzle-ion source and their photoelectron spectra measured with a continuous anion photoelectron apparatus.[45] In the other case, the anions were generated with a photoinduced electron emission source, and their photoelectron spectra were measured with a pulsed anion photoelectron apparatus.[46] In both instruments, anion photoelectron spectroscopy was conducted by crossing a mass-selected beam of negative ions with a fixed-frequency photon beam and then energy analyzing the resultant photodetached electrons. This technique is governed by the energy conserving relationship hv = EKE + EBE, where hv is the photon energy, EKE is the measured electron kinetic energy, and EBE is the electron binding energy.

IV.3.2.1. Continuous Anion Photoelectron Spectrometer.

In this type of anion photoelectron spectrometer, the ion source and all of the other components operate continuously.[45] The ion source was a biased (−500 V), supersonic expansion nozzle-ion source in which the acetoacetic acid sample was placed inside its

stagnation chamber. There, due to the warming of the source by the adjacent hot filament, some of the sample evaporated and was expanded through a 25 μm diameter nozzle orifice into ~10^{-4} Torr vacuum along with argon gas which was maintained at a pressure of 1−2 atm in the source's stagnation chamber. Anions were formed by injecting low-energy electrons from a hot, even more negatively biased, thoriated iridium filament into the expanding jet, where a weak external magnetic field helped to form a microplasma. The nascent anions were then extracted into ion optics and mass selected by a 90° magnetic sector, mass spectrometer with a mass resolution of ~400. After mass selection, the beam of acetoacetic acid parent anions was crossed with an argon ion laser beam (operated intracavity), where electrons were photo-detached. These were then energy analyzed by a hemispherical electron energy analyzer operating at a resolution of 30 meV. The photoelectron spectra reported here were recorded with 2.54 eV photons and calibrated against the well-known photoelectron spectrum of O^-.[47]

IV.3.2.2. Pulsed Anion Photoelectron Spectrometer.

In this type of anion photoelectron spectrometer the ion source and all of the other components operate in a pulsed manner.[46] Anions were generated by the interaction of laser-generated photoelectrons with a pulsed jet of helium gas containing a small amount of acetoacetic acid vapor. The photoelectrons were produced by pulsed laser irradiation (Nd:YAG laser operating at 2.33 eV/photon) of a rotating, translating copper rod which was mounted inside a grounded housing having a laser beam entrance port, a pulsed gas valve, and an exit nozzle. A small amount of acetoacetic acid sample was placed inside the pulsed gas valve, and together with 4 atm of helium gas, its vapor was expanded in synchronization with the laser pulses. Photoemitted electrons attached to AA molecules

to form AA^- anions. These were entrained in the ensuing jet which was directed through a skimmer and a subsequent differential pumping chamber into the Wiley−McLaren extraction plates of a linear, time-of-flight mass spectrometer (mass resolution 500). After mass selection by a mass gate and deceleration via a momentum decelerator, the anions of interest were irradiated by a second pulsed laser beam (Nd:YAG laser operating at 3.49 eV/ photon), which photodetached electrons from them. The photo-detached electrons were then energy analyzed by a magnetic bottle, electron energy analyzer with a resolution of 35 meV at EKE = 1 eV. The photoelectron spectrum was calibrated against the well-known atomic lines of Cu^-.[48] The pulsed photoelectron spectrometer probed a wider range of electron binding energies than the continuous photoelectron spectrometer due to its use of higher energy photons.

IV.3.3. Electron Energy-Loss Spectroscopy.

The electron-impact spectrometer used in this study has been described in the work on the formic acid dimer[18] (and references cited therein). It uses hemispherical analyzers to prepare a beam with a narrow electron energy spread and to analyze energies of the scattered electrons. The measurements were performed at a scattering angle of 135°. The sample was kept in ice and evaporated through a needle valve to a 0.25 mm diameter effusive orifice kept at 30 °C. The resolution was about 20 meV in the energy-loss mode.

IV.4. COMPUTATIONAL RESULTS

IV.4.1. Neutral AA.

Neutral AA supports minima for the keto and enol tautomers (Figure IV.2). Our attempts to identify an ol minimum energy structure with H1 bound to O1 failed: the H1 proton either transferred back to O2 or the molecule broke into propen-2-ol and CO_2.[23] There are

six low-lying keto conformers (**K1−K6**) within an energy range of 1 kcal/mol. Their structures and the transition states separating them are presented in the Supporting Information, Figure S1. The enol conformers are presented there as well in Figure S2. The most stable E1 is separated from other enols by at least 4 kcal/mol. The minima of the neutral AA relevant for the further discussion (**K1, K3, K5, E1**) are presented in Figure IV.2.

The relative stability of **K1** with respect to **K3, K5**, and **E1** is summarized in Table IV.1. In terms of electronic energies, the enol **E1** is the most stable at all levels of theory

Table IV.1: Relative Stability (kcal/mol) of the Most Relevant Tautomers and Conformers of Neutral AA

str.	E_{elec}^{MP2}	E_{elec}^{CCSD}	$E_{elec}^{CCSD(T)}$	$E_{elec}^{CCSD(T)} + E_{0,vib}^{MP2}$	$E_{elec}^{CCSD(T)}$ + Gibbs
K1	0.00	0.00	0.00	0.00	0.00
K3	0.04	−0.41	0.01	−0.32	−0.98
K5	0.24	−0.13	0.28	−0.06	−0.82
E1	−2.85	−1.55	−1.91	−1.01	−0.20

by ca. 2 kcal/mol. The keto conformers are clustered within a narrow range of 0.3 kcal/mol, with **K1** being the most stable. With such small differences in electronic energies, the zero-point energies and thermal contributions to thermodynamic functions clearly matter. As was observed in the past, conformers with hydrogen bonds have higher zero-point vibrational energies despite significant red shifts of the proton donor stretching frequencies.[49,50] The same pattern is observed here, i.e., **E1** and **K1** have the highest zero-point vibrational corrections in the enol and keto families, respectively. The thermal contribution to the stability is dominated by entropic effects associated with very soft vibrational modes. Thus, again **E1** and **K1** are disfavored, and the most stable gaseous conformers at standard conditions are **K3** and **K5**, though the spread of Gibbs free

energies is very narrow, less than 1 kcal/mol. Our findings are consistent with the earlier liquid-phase ^{1}H NMR results of Grande and Rosenfeld.[26]

A simplified landscape of the potential energy surface for the keto conformers is illustrated in Figure IV.4. One could anticipate that the **K1** conformer would be particularly

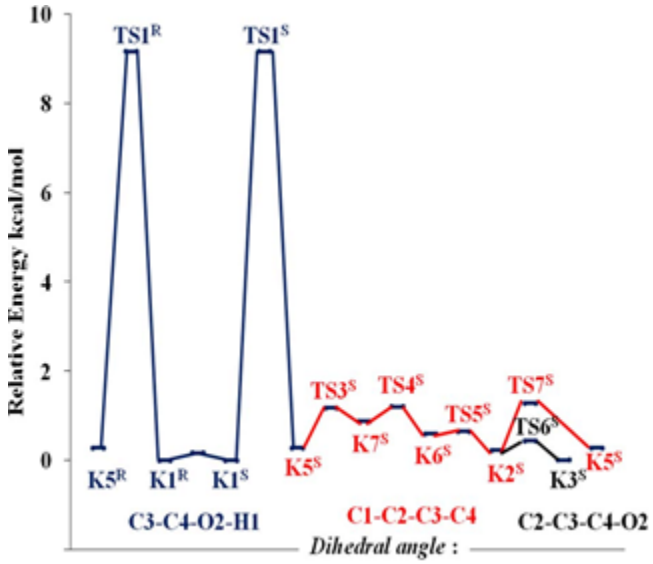

Figure IV.4: Energy profile connecting keto structures of AA. Energies (kcal/mol) were calculated at the CCSD(T)/ADZ level using the CCSD/ADZ geometries.

stable due to the intramolecular O2H1···O1 hydrogen bond, but the relative energies listed in Table IV.1 and Figure S1 indicate otherwise. **K1** is unique not so much in its stability but in the energy barrier (**TS1** at 9.2 kcal/mol) that separates it from **K5** and the remaining conformers. This barrier can be associated with breaking of the intramolecular hydrogen bond. The barriers separating the conformers **K2**−**K7** are much smaller and do not exceed 1.1 kcal/mol.

There are at least two factors that oppose the stabilizing effect of the intramolecular hydrogen bond in **K1**. First, **K1** is the most polar conformer, with a dipole moment

exceeding 5.4 D. The remaining conformers have dipole moments smaller by more than 1.8 D. High polarity typically increases the electronic energy of a neutral molecule by raising the energy of the highest occupied orbital. Second, formation of the O2H1···O1 hydrogen bond is associated with intramolecular strain. The results obtained with the Amber[51] force field, see Table S5, confirm this hypothesis. A sum of the angle bending, torsional and bond stretching terms is larger in **K1** than in, e.g., **K5**, by ca. 2.8 kcal/mol.

IV.4.2. Anionic AA.

K1 is the most promising conformer to host a dipole-bound anionic state in view of its competitive stability and dominant polarity (μ = 5.4 D). In addition to the dipole-bound state, AA can support a valence-bound anion. An overview of anionic states of AA is presented in Figure IV.5 using a set of geometries connecting the dipole-bound minimum, similar to the **K1** structure of the neutral, with the valence-bound anion minimum: $G_{M_{dbs}^-}$ with $G_{M_{VB}^-}$. The potential energy curve of the neutral is repulsive upon

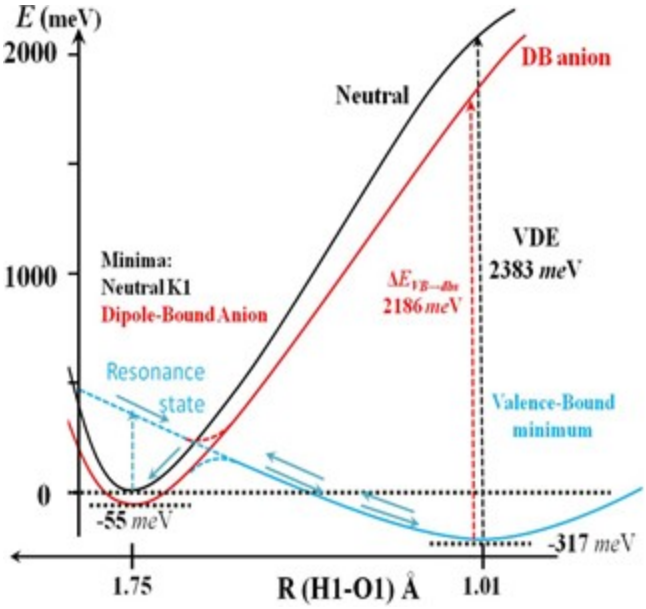

Figure IV.5: Energy profile depicting the neutral (black),dipole-bound (red), and valence (blue) anionic potential energy surfaces of AA. Energies (meV) computed at the CCSD(T)/ADZ+DF level. (Left) Dipole-bound anionic minimum and the local minimum of the neutral (K1). (Right) Global minimum of the valence anion.

transferring H1 from O2 to O1. The dipole moment of the neutral increases upon proton transfer from 5.4 to 10.0 D. Thus, the dipole-bound anion remains bound upon proton transfer. The valence anion is unbound at the minimum energy structure of the neutral; it can be probed as a resonance state with a very short finite lifetime in the EELS experiments (see section IV.5.2). The energy of the resonance quickly decreases upon intramolecular proton transfer, crosses the potential energy surface of the neutral, and undergoes an avoided crossing with the dipole-bound anion.

With H1 transferred from O2 to O1, the valence anion supports a minimum, which is characterized by a VDE of 2383 meV. The valence anion is adiabatically bound with respect to the neutral **K1** by 317 meV (in terms of electronic energies). A vertical electronic excitation energy from the valence-to the dipole-bound anionic state,

$\Delta E_{VB\rightarrow dbs}$, is 2186 meV. In future experiments, one might want to probe the molecular dynamics of AA^- upon this electronic excitation.

The singly occupied molecular orbitals in the DB and VB anions, each at its minimum energy structure, are illustrated in Figure IV.6. The former orbital is very diffuse and

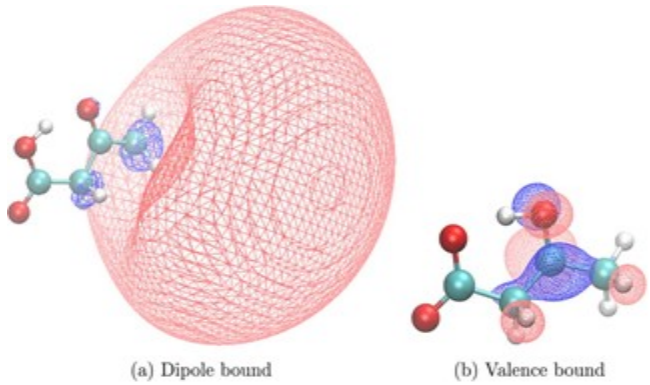

Figure IV.6: Orbital occupied by an excess electron in the DB and VB anions of AA plotted with a fraction of electron density (F_e) equal to 0.6.[42]

localized on the positive pole of the molecular dipole, which proves to be a hydrophobic group CH_3. The latter is a π orbital localized around the C2 atom, with bonding interactions involving the neighboring carbon atoms and an antibonding interaction between C2 and O1. The unpaired electron in the valence anion is localized in the vicinity of C2O1H, but the excess charge is localized on C4OO^-.

$G_{M_{dbs}^-}$ differs from G_M by shortening the O1···H1 distance by 0.036 Å, increasing the O1−H1−O2 angle by 1.6°, and an elongation of the O2−H1 distance by 0.003 Å, see Figures IV.2 and IV.3. Overall it is a small step toward proton transfer, a nascent zwitterionization. The dipole moment of neutral AA increases by 0.16 D upon these geometrical distortions, a typical increase for dipole-bound anionic states.

The vertical electron binding energies for the dipole-bound anionic state, obtained with indirect and direct methods, are reported in Table IV.2 for the G_M, $G_{M^-_{dbs}}$, and the $G_{M^-_{VB}}$ geometries.

Table IV.2: Adiabatic Electron Affinities (meV) of the DB and VB Anions Calculated at Different Levels of Theory with the CCSD-Optimized Geometries. All calculations with the ADZ+DF basis set

		EBE		
method		G_M	$G_{M^-_{dbs}}$	$G_{M^-_{VB}}$
indirect	SCF	24.06	26.89	127.68
	MP2	32.81	36.31	217.72
	CCSD	52.34	56.59	196.85
	CCSD(T)	52.19	56.55	197.04
direct EA	KT	21.59	24.33	113.30
	EPT third	43.63	47.46	245.07
direct IP	KT	26.32	29.78	135.79
	EPT third	45.27	50.45	247.84

Starting from "indirect" electron binding energies, the SCF contribution represents only 46−65% of the CCSD(T) results, illustrating the role of electron correlation effects in dipole-bound anionic states. The differences between the CCSD and the CCSD(T) results do not exceed 0.2 meV. The electron binding energies obtained in "direct" approaches start from the Koopmans' theorem estimations; thus, they neglect orbital relaxation and electron correlation effects. The differences between the KT and the SCF "indirect" results are small, indicating that orbital relaxation effects are minor for the dipole-bound anionic state. The EPT third-order results are in good agreement with the "indirect" CCSD(T) results. The role of the second-order dispersion interaction between the loosely bound electron and the electrons of AA is illustrated in Table S4.

Various estimations of adiabatic electron affinity for this anionic state are reported in Table IV.3. The CCSD(T) and CCSD results are very similar, approximately 54 meV, and the zero-point vibrational correction further stabilizes the anion by 3 meV. The

Table IV.3: Adiabatic Electron Affinities (meV) of the DB and VB Anions Calculated at Different Levels of Theory with the CCSD-Optimized Geometries. All calculations with the ADZ+DF basis set

	AEA (electronic)					ΔE_{vib}		AEA
	SCF	MP2	CCSD	CCSD(T)		CCSD		CCSD(T)
DB	8.6	38.88	54.15	54.56		2.63		57.19
VB	-182.82	286.26	289.55	317.02		17.27		334.29

decomposition of the electronic component of AEA into the $\Delta E_M(G_M-)$ and VDE terms (eq 5, Table IV.4) illustrates a very small geometrical distortion of the molecular framework upon the excess electron attachment and the dominant role of VDE.

Table IV.4: Electronic component (CCSD(T)/ADZ+DF) of AEA (meV) decomposed into the $\boldsymbol{\Delta E_M(G_M-)}$ and VDE terms.

	$-\Delta E_M(G_M-)$	VDE	AEA
DB	−1.99	56.55	54.56
VB	−2065.69	2382.71	317.02

In contrast to the neutral AA, which supports several low-lying minimum energy structures, the valence anion of AA supports one distinct global minimum illustrated on the right side of Figure IV.3. Other minima (local) are less stable by more than 12 kcal/mol and are characterized by negative values of AEA. They display VDEs exceeding 2.9 eV, thus much higher than the VDE of VB, see Table S6 and Figure S4. We also searched for valence anions associated with the enol structures. There were no electronically bound valence anions around the equilibrium structures of **E1** and **E3**. Even upon transferring the O1H proton to the carboxylic group, the valence anions

remained electronically unbound. Thus, from now on, our discussion will be limited to **VB** illustrated on the right side of Figure IV.3.

In the **VB** minimum, the H1 proton is bound to O1 and the O1H1···O2 hydrogen bond is very short, R(H1O2) = 1.583 Å. The intramolecular hydrogen bond is more linear than in the neutral or dipole-bound anion by 6−8°. When compared with the **K1** neutral, there is a significant elongation of the C2O1 distance by 0.146 Å and a shortening of C4O2 by 0.064 Å, consistent with a redistribution of double bonds upon tautomerization. Finally, the CH3 group is rotated by ca. 58° in comparison with **K1**.

The VDEs obtained using "indirect" methods and "direct" EPT span a reasonably narrow range of 2300−2600 meV (Table IV.5). The Koopmans' theorem EA and IP values are 713 and 4200 meV, respectively, while the indirect SCF value is 2400 meV, demonstrating that orbital relaxation effects are critically important for this anionic state. Electron correlation effects, on the other hand, do not contribute much to the VDE value. The anion should be readily formed in anion sources, because its adiabatic electron affinity is modest but positive, i.e., 334 meV, after inclusion of the zero-point vibrational

Table IV.5: Values of VDE (meV) for the Valance Anions of AA.

method		VDE
indirect	SCF	2400.48
	MP2	2347.34
	CCSD	2482.36
	CCSD(T)	2382.71
direct EA	KT	713.43
	EPT third	2304.34
direct IP	KT	4200.09
	EPT third	2602.50

correction (Table IV.3). The electronic contribution to AEA can be analyzed in terms of Equation 5 (Table IV.4). Proton transfer from O2 to O1 is accompanied by a significant increase of the energy of the neutral ($\Delta E_M(G_{M^-})$ = 2066 meV). This energy increase is, however, outweighed by the VDE of 2383 meV. The modest electronic contribution to AEA of 317 meV results from a cancellation of the $\Delta E_M\left(G_{M^-_{VB}}\right)$ and VDE terms.

IV.5. EXPERIMENTAL RESULTS

IV.5.1. Photoelectron Spectroscopy Results for AA^- and $(AA)_2^-$.

Parent anions of AA were prepared using two rather different anion source environments. Figure IV.7 presents a representative mass spectrum of the anions produced by our pulsed, laser photoemission source. In addition to AA^-, the spectrum shows $(AA{-}H_2O)^-$. Our preliminary computational results for several isomers of $(AA{-}H_2O)^-$ indicate that some of them are adiabatically bound with the VDEs exceeding 1.4 eV. Our complete results for the anions of $AA{-}H_2O$ will be presented in a future report. The mass spectrum also shows $(AA)_2^-$.

The photoelectron spectrum of the AA^- parent anion measured on our continuous photoelectron spectrometer and recorded with 2.54 eV photons is presented in Figure IV.8.

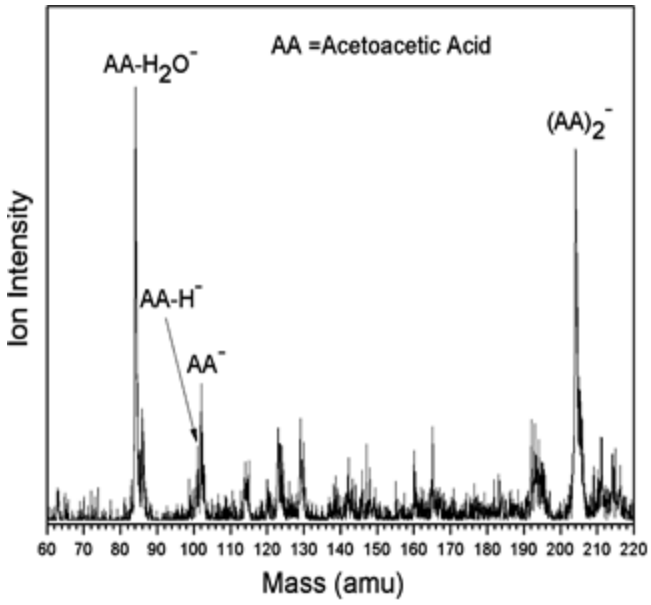

Figure IV.7: Mass spectrum of anions observed in these experiments.

This spectrum consists of a broad, featureless band with an onset at EBE ≈ 1.2 eV and an intensity maximum at EBE 2.04 eV. This latter quantity corresponds to the VDE of AA^-.

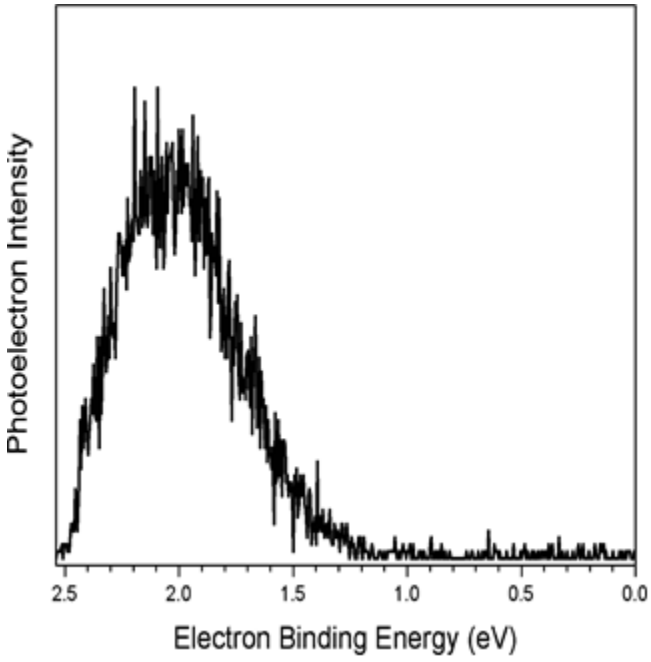

Figure IV.8: Photoelectron spectrum of the AA^- parent anion recorded with 2.54 eV photons on our continuous photoelectron spectrometer.

The calculated adiabatic electron affinity of 0.33 eV is much smaller than the onset, suggesting that the 0−0 transition has a diminishingly small intensity due to poor Franck−Condon overlap between the AA^- anion and its neutral counterpart. The calculated VDE of 2.38 eV is larger by 0.34 eV than the measured intensity maximum. The source of this discrepancy is discussed below.

The photoelectron spectrum of the AA^- parent anion measured on the pulsed photoelectron spectrometer and recorded with 3.49 eV photons is presented in Figure IV.9. This spectrum also consists of a broad, featureless band with an onset at EBE ≈ 1.2 eV but with an intensity maximum at EBE 2.30 eV. This latter quantity again

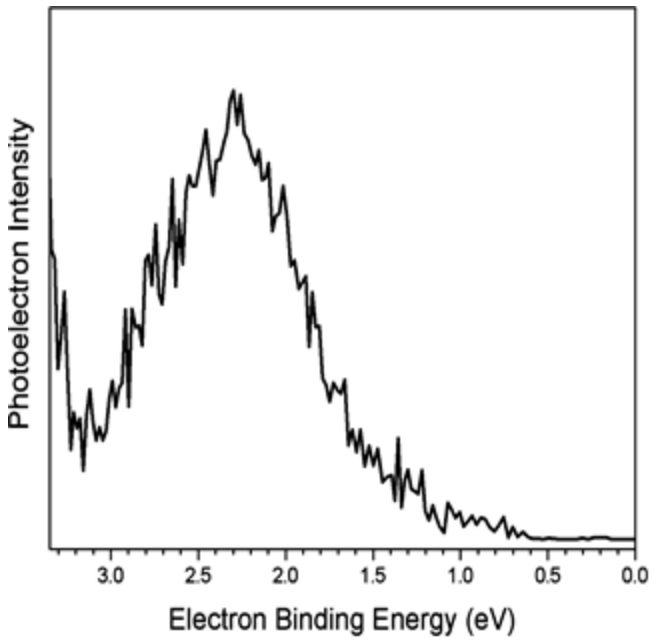

Figure IV.9: Photoelectron spectrum of the AA^- parent anion recorded with 3.49 photons on the pulsed photoelectron apparatus.

corresponds to the VDE of AA^-. This value of VDE is in good agreement with the calculated value of 2.38 eV. This spectrum does not display a pronounced intensity

increase in the 2.9−3.0 eV range, where the electron vertical detachment energies for the valence anions other than VB are predicted to appear (see Figure S4).

For the most part, the two photoelectron spectra are the same, indicating that both source environments produced the same parent AA^- species. The main difference lies in the slightly different VDE values obtained on different apparatuses. The difference between the two measured VDE values is attributed to the electron transmission function roll-off inherent for low kinetic energy (high EBE) electrons. This effect comes into play more strongly for a lower versus a higher photon energy, since a lower photon energy puts more of the spectrum in the low EKE region of the spectrum. On the continuous apparatus, whose photon energy was 2.54 eV/photon, this had the effect of attenuating the still rising photoelectron band, making its intensity maximum appear to occur at a slightly lower EBE value. By contrast, the pulsed apparatus, which utilized a photon energy of 3.49 eV/photon, was not significantly affected in this way. Thus, we believe that the more reliable value for the VDE of AA^- is 2.3 eV, close to that predicted by theory.

We also measured the photoelectron spectrum of the parent dimer anion, $(AA)_2^-$, and it is presented in Figure IV.10. This spectrum also exhibits a single broad band, and it has a similar width to that of the monomeric AA^-. Interestingly, its VDE value, at 1.7 eV, is considerably lower than that of the monomer, indicating that the additional AA molecule is not simply solvating AA^-, i.e., it is not a simple anion−molecule complex.

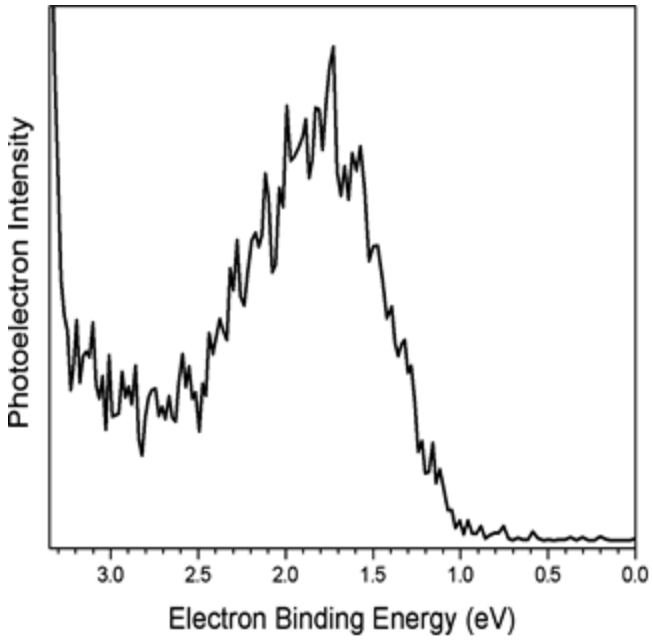

Figure IV.10: Photoelectron spectrum of $(AA)_2^-$ parent anion recorded with 3.49 eV photons on the pulsed photoelectron apparatus.

IV.5.2. Electron Energy-Loss Spectroscopy Results for AA.

Our electron energy-loss spectrum for AA is shown in Figure IV.11. The hypothetical processes induced by the attachment of an electron onto neutral **K1** are suitably visualized by the diagram in Figure 5. Vertical electron attachment, indicated by the vertical blue dashed arrow, transfers the nuclear wave packet to the repulsive part of the valence anion potential surface a resonance because it is subject to autodetachment. The present discussion concentrates on the lowest shape (i.e., not core excited) resonance with temporary occupation of the π_1^* orbital. The nuclear wave packet then starts to relax by sliding down the repulsive surface, in competition with rapid autodetachment. Detachment of an electron at an early stage of the relaxation leads to a vibrationally excited final state of the neutral molecule. Since the detachment rate during the initial relaxation of the nuclei is faster than the nuclear motion (this is indicated by the absence

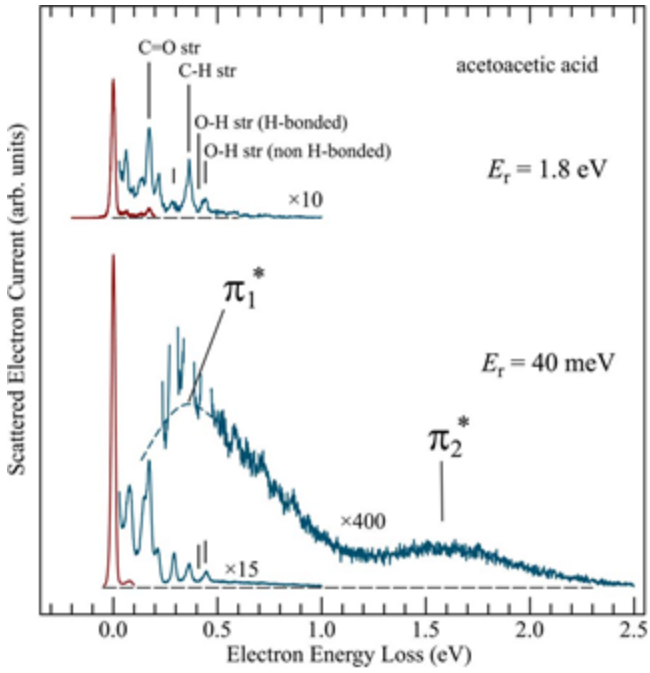

Figure IV.11: Spectra showing the yields of electrons with the specified residual energies E_r plotted as a function of energy loss.

of boomerang structure in the spectra),[52] this process leads to (i) excitation of primarily low quanta of the vibration and (ii) pronounced selectivity with respect to the modes, with those modes being primarily excited along which the anion potential has a large slope at the point of attachment. This process has been termed "specific" vibrational excitation[53] and gives rise to the sharp vibrational peaks on the left side of the spectra in Figure IV.11. A fraction of the nuclear wave packet survives until it reaches portions of the potential surface where the detachment is slow or the ion is even bound, allowing intramolecular vibrational redistribution (IVR) which "wipes out" the initial mode specificity, leading to the excitation of a quasi-continuum of high-lying vibrational levels, accompanied by detachment of a very slow electron. This process has been termed "unspecific" vibrational excitation[53] and gives rise to the structureless humps in the lower spectrum in Figure IV.11. One could also term the detachment in the initial phases of the

relaxation “nearly vertical” and in the later phases, after IVR, “nearly horizontal”. The latter process gives rise to the capacity of the resonances to quasi-thermalize the incident electrons. The “unspecific” vibrational excitation and the corresponding humps in the spectra showing the yield of very slow electrons at incident electron energies corresponding to resonances are found in all molecules larger than diatomic.[53] The effect is usually weak but becomes more pronounced for large molecules. The two humps in the lower spectrum in Figure IV.11 indicate a π_1^* (LUMO) resonance at 0.4 eV and a π_2^* (LUMO+1) resonance at 1.6 eV.

An interesting effect was observed in the formic acid dimer where the “unspecific” vibrational excitation band in the yield of quasi-thermal electrons was anomalously large, 20 times larger than in the monomer.[18] It was interpreted as a manifestation of a very fast intermolecular proton (or hydrogen) transfer in the resonance, which gave a competitive edge to relaxation over electron detachment, thus increasing the yield of the unspecific process.

It may be noted as a side remark that stretching of the O−H bond in the formic acid monomer yields $HCOO^-$ + H (dissociative electron attachment, DEA), the mechanism of which we studied recently.[54] The intermolecular (in the case of the formic acid dimer) and intramolecular (in the case of AA) proton transfer may be viewed as a “frustrated” DEA.

The question posed here is whether an anomalously high intensity of the “unspecific” vibrational excitation hump, linked to intramolecular proton transfer, is also observed in AA. The spectra in Figure IV.11 show that a hump is indeed observed, but to decide whether it may be called anomalously high requires at least an approximate quantitative consideration. For this purpose, we determined the ratio of the signals integrated under

the discrete narrow vibrational peaks (representative for the weakly relaxed specific process) and the structureless hump (representative for the fully relaxed unspecific process).

To bypass a problem given by the overlap of the unspecific and the specific energy ranges below 0.5 eV, the unspecific signal is extrapolated visually to low energies as indicated by the dashed curve in Figure IV.11. The shape of the extrapolated section is guided by the depths of the valleys between the specific vibrational peaks down to 0.25 eV and by the expected shape of a Franck−Condon band below that. The integral under the smooth band, including the extrapolated section, is taken as the unspecific contribution. The specific contribution is the integral under the total measured signal minus the unspecific contribution. Both integrals were taken between 0.035 and 1.2 eV. The result is that the integral under the structureless band is about 3 times less than the integral under the narrow structures. This can be compared to the formic acid dimer where the integral under the structureless band is about 3 times larger than the integral under the narrow structures. The intensity of the unspecific signal relative to the specific signal is thus 9 times smaller in AA when compared to formic acid dimer. The unspecific signal in AA is thus not anomalously high and cannot be taken as evidence for intramolecular proton transfer. The unspecific/specific ratio in AA is comparable, only marginally 2 times larger than that in the formic acid monomer (without intramolecular proton transfer). This would be expected for the “normal” (i.e., given by IVR and not by fast intramolecular transfer) unspecific signal which increases with increasing size of the molecule.

The capacity of the π_1^* resonance in AA to quasi-thermalize electrons is thus not large enough to provide positive evidence for an intramolecular proton transfer fast enough to compete with autodetachment. The anion photoelectron spectra and the calculations show beyond doubt that the equilibrium structure of the valence anion is proton transferred, however. The combined PES and EELS experimental evidence thus indicates that the electron-induced transfer occurs but slower than in formic acid dimer, so that it does not efficiently compete with the fast autodetachment. The reason may be that only a fraction of the target AA is in the H-bonded conformation suitable for fast proton transfer.

This is indicated by the computational results detailed in Table IV.1. The **K1** conformer, which is capable to relay H1, is thermodynamically disfavored. This conformer is also kinetically difficult to access from the more populated **K3** and **K5** conformers due to a high-barrier **TS1** (see Figure IV.4). Thus, a rotation of the O2H1 bond to make a H-bonded keto conformer is expected to be slow in comparison with electron autodetachment. In consequence, the temporary anion typically autodetaches before finding a refuge on the right side of Figure IV.5, where the anionic state is bound. Another neutral AA with a bridging hydrogen, **E1**, is expected to be more common than **K1** (Table IV.1), but it does not support an electronically bound valence anion either with or without a proton transferred from O1H to O3. Thus, the slope of the anion potential on the left side of Figure IV.5 is expected to be smaller than for **K1**, and there is no refuge where the anion would be electronically bound.

The above interpretation is consistent with the discrete vibrational energy-loss spectra on the left side of both traces in Figure IV.11, where nearly no intensity is observed for H-bonded O−H stretch. Our computational results confirm that the O− Hs engaged in

hydrogen bonds have lower frequencies (3433 (**K1**) and 3304 cm−1 (**E1**)) than those with free O−Hs (3731 (**K3**), 3736 (**K5**), and 3740 cm−1 (**E1**)). The low-frequency O−H stretches are not visible in the spectrum because **K1** and **E1** are minor constituents of the gas phase AA. Additionally, even if **E1** was present, its H-bonded O−H stretch would not be pronounced because the slope of the anion potential along the proton transfer coordinate is low at the point of electron attachment.

IV.6 DISCUSSION

The computational results indicate that the global minimum of the acetoacetic acid valence anion corresponds to an ol structure, with a proton transferred from the carboxylic to the keto group. We conclude that binding an excess electron on the π_1^* valence orbital changes the localization of the proton in acetoacetic acid, provided the anion becomes fully relaxed. The valence anion is characterized by a significant electron vertical detachment energy of 2383 meV but only a modest adiabatic electron affinity of 334 meV.

Parent anions of acetoacetic acid were successfully prepared using two different source environments. The photoelectron spectra consist of a broad, featureless band with an onset at an electron binding energy of ca. 1.2 eV. The intensity maximum recorded with 3.49 eV photons is at 2.30 eV, in good agreement with the computed VDE of 2.38 eV for the fully relaxed anion. The calculated adiabatic electron affinity of 0.33 eV is much smaller than the onset of the spectra, indicating that the 0−0 transition has a very small intensity due to poor Franck−Condon overlap. The electron energy-loss spectra do show a broad structureless band in the yield of quasi-thermalized electrons (40 meV) following

an electron attachment into the π_1^* resonance. This band indicates a rapid IVR process in the resonance, but in contrast to the formic acid dimer case the band is not anomalously strong and thus does not provide evidence of the IVR process being promoted by an ultrafast proton transfer in the resonance. We explain it as a consequence of the fact that only the **K1** conformer is prearranged to relay a proton across the H-bonded bridge. However, contrary to naive chemical intuition, this conformer is present in only a small fraction in the target gas of the energy-loss experiment. Evidence for the low population comes from the calculations and from the near absence of the H-bonded O−H stretch in the energy-loss spectra. The global minimum for the neutral formic acid dimer, on the other hand, is supported by a cyclic hydrogen bond, and thus, it is prearranged to transfer a proton upon an excess electron attachment.[18,19]

The agreement between the measured (2.30 eV) and the calculated (2.38 eV) values of VDE indicates that AA^- formed in the microplasma sources of the PES experiments is the fully relaxed valence-bound anion **VB**, with the −COOH proton transferred to the keto group. In these experiments the vapor of AA is expanded with a noble gas into vacuum and electrons are injected in the high-pressure portion of the jet. Three-body collisions (noble gas) are needed to cool hot, short-lived autodetaching species. A typical flight time to the mass selector and to the photodetachment region is 5−20 μs, depending on the mass of the anion and on the energy at which it was accelerated. Thus, the temporary species have roughly a 10 μs temporal window to undergo ion−molecule reactions, form larger clusters, and cool down. The occurrence of complex chemical transformations has indeed been demonstrated in our past studies on anions of nucleic acid bases.[55] The most stable valence anions are formed upon proton transfer from nitrogen to carbon atoms. The

barriers for unimolecular transformations were found to be prohibitively high, and dissociative electron attachment followed by ion−molecule reactions were invoked to justify formation of these unusual species.

Formation of AA^- in the microplasma source does not rely on the presence of **K1** in the expanding mixture of AA and the noble gas. The formation mechanism might be more complex than a simple electron attachment to AA followed by a rapid proton transfer. There is a temporal window of several microseconds for the anionic species to rotate the O2H1 bond and reach the H-bonded bridge structure, transfer the proton, cool down in the course of collisions with noble gas atoms, and relax into the lowest vibrational state of the global minimum of **VB**.

In contrast, the EELS experiments probe a distribution of neutral molecules in the gas phase. The H-bonded **K1** conformer is minor in the liquid phase,[26] and accessing it in the gas phase is obstructed by a transition state of 9.2 kcal/mol. Short-lived autodetaching anionic species have a temporal window comparable with the resonance lifetime, thus femtoseconds, to transfer a proton in unimolecular processes. A rotation of the O2H1 bond is too slow to reach the H-bonded bridge structure suited for relaying H1 to the keto group and sheltering the anion in the electronically bound region of the potential energy surface. As a result, the temporary anion of AA decays primarily through a “nearly vertical” autodetachment.

IV.7 SUMMARY

We searched for the most stable tautomers and conformers of the neutral and anionic acetoacetic acid using a potential energy surface scanning tool (PESST).[27] The neutral

AA supports minima for the keto and enol tautomers. Our CCSD(T) electronic energies corrected for zero-point vibrations and thermal contributions to the Gibbs free energy indicate that the keto conformers without the intramolecular hydrogen bond are more stable than the conformers with the intramolecular hydrogen bond (keto or enol). The spread of Gibbs free energies is, however, very narrow, less than 1 kcal/mol at standard conditions.

We paid particular attention to a keto conformer **K1** with the intramolecular hydrogen bond and thus susceptible to intramolecular carboxylic-to-keto proton transfer. It belongs to a grouping of the most stable conformers of the neutral AA and proved to be the most polar, with a dipole moment of 5.4 D. **K1** is separated from other keto conformers by a relatively high barrier exceeding 9 kcal/mol. The barriers separating other conformers are much smaller and do not exceed 1.1 kcal/mol. **K1** supports a dipole-bound anion with an electron vertical detachment energy of 57 meV. The dipole-bound anion remains bound upon the intramolecular carboxylic-to-keto proton transfer.

The valence anion of acetoacetic acid undergoes proton transfer upon an excess electron attachment. The distinct global minimum is supported by a short (H···O distance of 1.58 Å) intramolecular hydrogen bond between the hydroxy and carboxylate groups. The valence anion is not only vertically (2383 meV) but also adiabatically (334 meV) bound. The electronic excitation energy from the valence-to dipole-bound state is 2186 meV. Dynamics of the anion excited to the repulsive wall of the dipole-bound state can be explored in future experiments.

The photoelectron spectra from the continuous and pulsed photoelectron spectrometers were obtained with 2.54 and 3.49 eV photons, respectively. The spectrum obtained with

3.49 eV photons from the pulsed apparatus is more reliable and displays a broad, featureless band with an onset at an electron binding energy of ca. 1.2 eV and an intensity maximum at 2.30 eV. The reported spectra do not provide evidence for the dipole-bound anion. The photoelectron spectrum of the parent dimer anion of acetoacetic acid shows a vertical detachment energy at 1.7 eV, which is considerably lower than that of the monomer, indicating that the additional monomer is not simply solvating the monomeric anion.

The electron energy-loss spectrum of acetoacetic acid displays narrow vibrational peaks representative of "nearly vertical" electron detachments and structureless humps representative of "nearly horizontal" detachments. The ratio of signals integrated under the discrete vibrational peaks and the structureless hump do not provide evidence for an intramolecular proton transfer fast enough to compete with autodetachment. The reason is that the conformer capable to relay a proton, i.e., H-bonded **K1**, is thermodynamically disfavored and kinetically difficult to access from the more populated but non-H-bonded keto conformers. This is confirmed by the near absence of the H-bonded O−H stretch in the energy-loss spectra.

Our results expose the importance of time scale and local environment in electron-driven proton transfer. The micro-plasma sources of anions in the PES experiments offer a temporal window of several microseconds to reach a H-bonded bridge structure, transfer the proton, cool down the temporary anion in course of collisions with noble gas atoms, and settle in the lowest vibrational state of the anionic global minimum. EELS experiments, on the other hand, probe a distribution of neutral molecules in the gas phase. Short-lived autodetaching anionic species have a temporal window comparable with the

resonance lifetime, thus femtoseconds, to transfer a proton in unimolecular processes. This takes place in the formic acid dimer, because its global minimum is supported by a cyclic hydrogen bond and thus prearranged to relay a proton.[18,19] A H-bonded bridge is not available in the most stable conformers of neutral acetoacetic acid, and the temporary anion decays primarily through a "nearly vertical" autodetachment.

Before closing we comment on the electron-driven proton transfer scheme in acetoacetic acid illustrated in the bottom of Figure IV.1. The right-hand side of it is true; the fully relaxed valence anion has an ol structure, is adiabatically bound, and displays a significant vertical detachment energy of 2.3 eV. The left and central parts are problematic. The neutral **K1** would indeed facilitate proton transfer due to the intramolecular H-bond bridge. Unfortunately, this conformer is not dominant in the gas phase at standard conditions. The spread of Gibbs free energies of the keto and enol tautomers and their conformers is very narrow, less than 1 kcal/mol at standard conditions, and the determination of major constituents of the gas-phase AA would be challenging without a combinatorial/computational tool PESST.[27]

Supporting Information

All supporting information and figures are available on the ACS Publications website at DOI: 10.1021/jacs.5b08134.

REFERENCES

1. Chang, C. J., Chang, M. C., Damrauer, N. H., Nocera, D. G. Biochim. Biophys. Acta, Bioenerg. **1655**, 13−28. (2004).

2. Sanche, L. Eur. Phys. J. D **35**, 367−390, (2005).

3. Kumar, A., Sevilla, M. D. Chem. Rev. **110**, 7002−7023, (2010).

4. Dempsey, J. L., Winkler, J. R., Gray, H. B. Chem. Rev. **110**, 7024−7039, (2010).

5. Petek, H., Zhao, J. Chem. Rev. **110**, 7082−7099, (2010).

6. Utke, I., Hoffmann, P., Melngailis, J. J. Vac. Sci. Technol. B **26**, 1197−1276, (2008).

7. Hammes-Schiffer, S. Chem. Rev. **110**, 6937−6938, 2010.

8. Xu, S., Zheng, W., Radisic, D., Bowen, K. H. J. Chem. Phys. **122**, 091103, 2005.

9. Meijer, G., de Vries, M. S., Hunziker, H. E., Wendt, H. R. J. Chem. Phys. **92**, 7625−7635, (1990).

10. Hunig, I., Plu¨tzer, C., Seefeld, K. A., Löwenich, D., Nispel, M., Kleinermanns, K. Chem. Phys. Chem. **5**, 1257−1257, (2004).

11. Bald, I., Dabkowska, I., Illenberger, E. Angew. Chem., Int. Ed. **47**, 8518−8520, (2008).

12. Bachorz, R. A., Haran´czyk, M., Dabkowska, I., Rak, J., Gutowski, M. J. Chem. Phys. **122**, 204304, (2005).

13. Gutowski, M., Dabkowska, I., Rak, J., Xu, S., Nilles, J., Radisic, D., Bowen, K. H., Jr. Eur. Phys. J. D. **20**, 431−439, (2002).

14. Radisic, D., Bowen, K. H., Dabkowska, I., Storoniak, P., Rak, J., Gutowski, M. J. Am. Chem. Soc. 2005, 127, 6443−6450.

15. Haran´czyk, M., Rak, J., Gutowski, M., Radisic, D., Stokes, S. T., Bowen, K. H. J. Phys. Chem. B **109**, 13383−13391, (2005).

16. Eustis, S. N., Radisic, D., Bowen, K. H., Bachorz, R. A., Haran´czyk, M., Schenter, G. K., Gutowski, M. Science **319**, 936−939, (2008).

17. Eustis, S. N., Whiteside, A., Wang, D., Gutowski, M., Bowen, K. H. J. Phys. Chem. A **114**, 1357−1363, (2010).

18. Allan, M. Phys. Rev. Lett. **98**, 123201, (2007).

19. Gerardi, H. K., DeBlase, A. F., Leavitt, C. M., Su, X., Jordan, K. D., McCoy, A. B., Johnson, M. A. J. Chem. Phys. **136**, 134318, (2012).

20. Stokes, S. T., Grubisic, A., Li, X., Ko, Y. J., Bowen, K. H. J. Chem. Phys. **128**, 044314, (2008).

21. Kobyłecka, M., Gu, J., Rak, J., Leszczynski, J. J. Chem. Phys. **128**, 044315, (2008).

22. Hay, R. W., Bond, M. A. Aust. J. Chem. **20**, 1823−1828, (1967).

23. Huang, C.-L., Wu, C.-C., Lien, M.-H. J. Phys. Chem. A **101**, 7867−7873, (1997).

24. Pedersen, K. J. J. Am. Chem. Soc. **51**, 2098−2107, (1929).

25. Hoz, S., Kresge, A. J. J. Phys. Org. Chem. **10**, 182−186, (1997).

26. Grande, K. D., Rosenfeld, S. M. J. Org. Chem. **45**, 1626−1628, (1980).

27. Keolopile, Z. G., Gutowski, M., Haranczyk, M. J. Chem. Theory Comput. **9**, 4374−4381, (2013).

28. Dunning, T. H. J. Chem. Phys. **90**, 1007−1023, (1989).

29. Kendall, R. A., Dunning, T. H., Harrison, R. J. J. Chem. Phys. **96**, 6796−6806, (1992).

30. Gutowski, M., Simons, J. J. Chem. Phys. **93**, 3874−3880, (1990).

31. Gutowski, M., Jordan, K. D., Skurski, P. J. Phys. Chem. A **102**, 2624−2633, (1998).

32. Skurski, P., Gutowski, M., Simons, J. Int. J. Quantum Chem. **80**, 1024−1038, (2000).

33. Becke, A. D. J. Chem. Phys. **98**, 5648−5652, (1993).

34. Lee, C., Yang, W., Parr, R. G. Phys. Rev. B: Condens. Matter Mater. Phys. **37**, 785−789, (1988).

35. Vosko, S. H., Wilk, L., Nusair, M. Can. J. Phys. **58**, 1200−1211, (1980).

36. Stephens, P. J., Devlin, F. J., Chabalowski, C. F., Frisch, M. J. J. Phys. Chem. **98**, 11623−11627, (1994).

37. Purvis, G. D., III, Bartlett, R. J. J. Chem. Phys. **76**, 1910−1918, (1982).

38. Bartlett, R. J., Musiał, M. Rev. Mod. Phys. **79**, 291−352, (2007).

39. von Niessen, W., Schirmer, J., Cederbaum, L. Comput. Phys. Rep. **1**, 57−125, (1984).

40. Frisch, M. J., Trucks, G. W., Schlegel, H. B., Scuseria, G. E., Robb, M. A., Cheeseman, J. R., Scalmani, G., Barone, V., Mennucci, B., Petersson, G. A., Nakatsuji, H., Caricato, M., Li, X., Hratchian, H.P., Izmaylov, A. F., Bloino, J., Zheng, G.,

Sonnenberg, J. L., Hada, M., Ehara, M., Toyota, K., Fukuda, R., Hasegawa, J., Ishida, M., Nakajima, T., Honda, Y., Kitao, O., Nakai, H., Vreven, T., Montgomery, J. A.Jr., Peralta, J. E., Ogliaro, F., Bearpark, M., Heyd, J. J., Brothers, E., Kudin, K. N., Staroverov, V. N., Kobayashi, R., Normand, J., Raghavachari, K., Rendell, A. R., Burant, J. C., Iyengar, S. S., Tomasi, J., Cossi, M., Rega, N., Millam, J. M., Klene, M., Knox, J. E., Cross, J. B., Bakken, V., Adamo, C., Jaramillo, J., Gomperts, R., Stratmann, R. E., Yazyev, O., Austin, A. J., Cammi, R., Pomelli, C., Ochterski, J. W., Martin, R. L., Morokuma, K., Zakrzewski, V. G., Voth, G. A., Salvador, P., Dannenberg, J. J., Dapprich, S., Daniels, A. D., Farkas, O., Foresman, J. B., Ortiz, J. V., Cioslowski, J., Fox, D. J. Gaussian 09, Revision D.01, Gaussian Inc.: Wallingford, CT, (2009).

41. Humphrey, W., Dalke, A., Schulten, K. J. Mol. Graphics **14**, 33−38, (1996).

42. Haranczyk, M., Gutowski, M. J. Chem. Theory Comput. **4**, 689−693, (2008).

43. Dennington, R., Keith, T., Millam, J. GaussView, Version 5, Semichem Inc.: Shawnee Mission, KS, (2009).

44. Krueger, R. C. J. Am. Chem. Soc. **74**, 5536−5536, (1952).

45. Coe, J. V., Snodgrass, J. T., Freidhoff, C. B., McHugh, K. M., Bowen, K. H. J. Chem. Phys. **84**, 618−625, (1986).

46. Gerhards, M., Thomas, O. C., Nilles, J. M., Zheng, W.-J., Bowen, J. K. H. J. Chem. Phys. **116**, 10247−10252, (2002).

47. Neumark, D. M., Lykke, K. R., Andersen, T., Lineberger, W. C. Phys. Rev. A: At., Mol., Opt. Phys. **32**, 1890−1892, (1985).

48. Ho, J., Ervin, K. M., Lineberger, W. C. J. Chem. Phys. **93**, 6987−7002, (1990).

49. Rak, J., Skurski, P., Simons, J., Gutowski, M. J. Am. Chem. Soc. **123**, 11695−11707, (2001).

50. Keolopile, Z. G., Ryder, M. R., Gutowski, M. J. Phys. Chem. A **118**, 7385−7391, (2014).

51. Cornell, W. D., Cieplak, P., Bayly, C. I., Gould, I. R., Merz, K. M., Ferguson, D. M., Spellmeyer, D. C., Fox, T., Caldwell, J. W., Kollman, P. A. J. Am. Chem. Soc. **117**, 5179 −5197, (1995).

52. Birtwistle, D. T., Herzenberg, A. J. Phys. B: At. Mol. Phys. **4**, 53−70, (1971).

53. Allan, M. J. Electron Spectrosc. Relat. Phenom. **48**, 219−351, (1989).

54. Janečková, R., Kubala, D., May, O., Fedor, J., Allan, M. Phys. Rev. Lett. **111**, 213201, (2013).

55. Li, X., Bowen, K. H., Haranczyk, M., Bachorz, R. A., Mazurkiewicz, K., Rak, J., Gutowski, M. J. Chem. Phys. **127**, 174309, (2007).

Chapter V: Ascorbate

Evan Collins, Mary Marshall, Zhaoguo Zhu, Sara Marquez, Kit H. Bowen,
Department of Chemistry, Johns Hopkins University, Baltimore, Maryland 21218, USA

V.1. INTRODUCTION

Reactive oxygen species (ROS) or free radicals in biological systems are formed through a variety of mechanisms. These species are generated through a range of both normal metabolic processes as well as through interaction of tissues with UV and ionizing radiation.[1] These species are very reactive and in turn cause damage to tissue and have been associated with many diseases such as cancer and other degenerative diseases.[1,2]

Biological systems have several methods for removing highly ROS from the body. One of them is through radical scavengers. These scavengers or antioxidants are generally molecules with a lone pair of electrons. These scavengers react with ROS and give up an electron, neutralizing the ROS and themselves become a stable radical species.[1, 2] After forming a more stable radical, these species are then degraded through different established pathways. One radical scavenger is ascorbic acid, also known as vitamin C. Ascorbic Acid is an excellent radical scavenger due to its ability to react with a wide range of biologically relevant ROS.[1] Another radical scavenger, vitamin E, has previously been studied via photoelectron studies.[3]

Ascorbate ($AscH^-$) is one of the active antioxidant forms of vitamin C. The biologically relevant forms of ascorbic acid and it's derivates are shown in Figure VI.1. Ascorbic acid ($AscH_2$) is mostly singly deprotonated in the form of ascorbate at physiological pH, as the pKA of the most acidic hydrogen is 4.24.[4, 5] Ascorbate is classified as a donor

antioxidant. It's active as an antioxidant due to its ability to donate an electron from the lone pair generated by deprotonation (Scheme 1).[2, 4]

$$AscH^- + X^\bullet \rightarrow AscH^\bullet + X^- \qquad \text{(Scheme 1)}$$

This species is transient as the hydrogen has a pKa of -0.9 and will deprotonate rapidly (Scheme 2).[5].

$$AscH^\bullet \rightarrow Asc^{\bullet-} + H^+ \qquad \text{(Scheme 2)}$$

$Asc^{\bullet-}$ is a stable radical species that converts in biological systems into dihydroxyabsorbic acid (DHA) and also ascorbate (Scheme 3).[5]

$$2Asc^{\bullet-} + H^+ \rightarrow AscH^- + DHA \qquad \text{(Scheme 3)}$$

The doubly deprotonated form of ascorbic acid, Asc^{2-}, can also act as an antioxidant by transferring an electron to a free radical species. This forms the stable radial $Asc^{\bullet-}$, however Asc^{2-} is not present in high concentrations in biological systems. Through the photoelectron study of $AscH^-$ and Asc^{2-} we hope to study the energetics of this process. In conjunction with the use of theoretical calculations we also hope to be able to calculate structures for the these biologically relevant forms of ascorbic acid. Here we report anion photoelectron spectra of ascorbate ($AscH^-$) and Asc^{2-} generated by electrospray ionization.

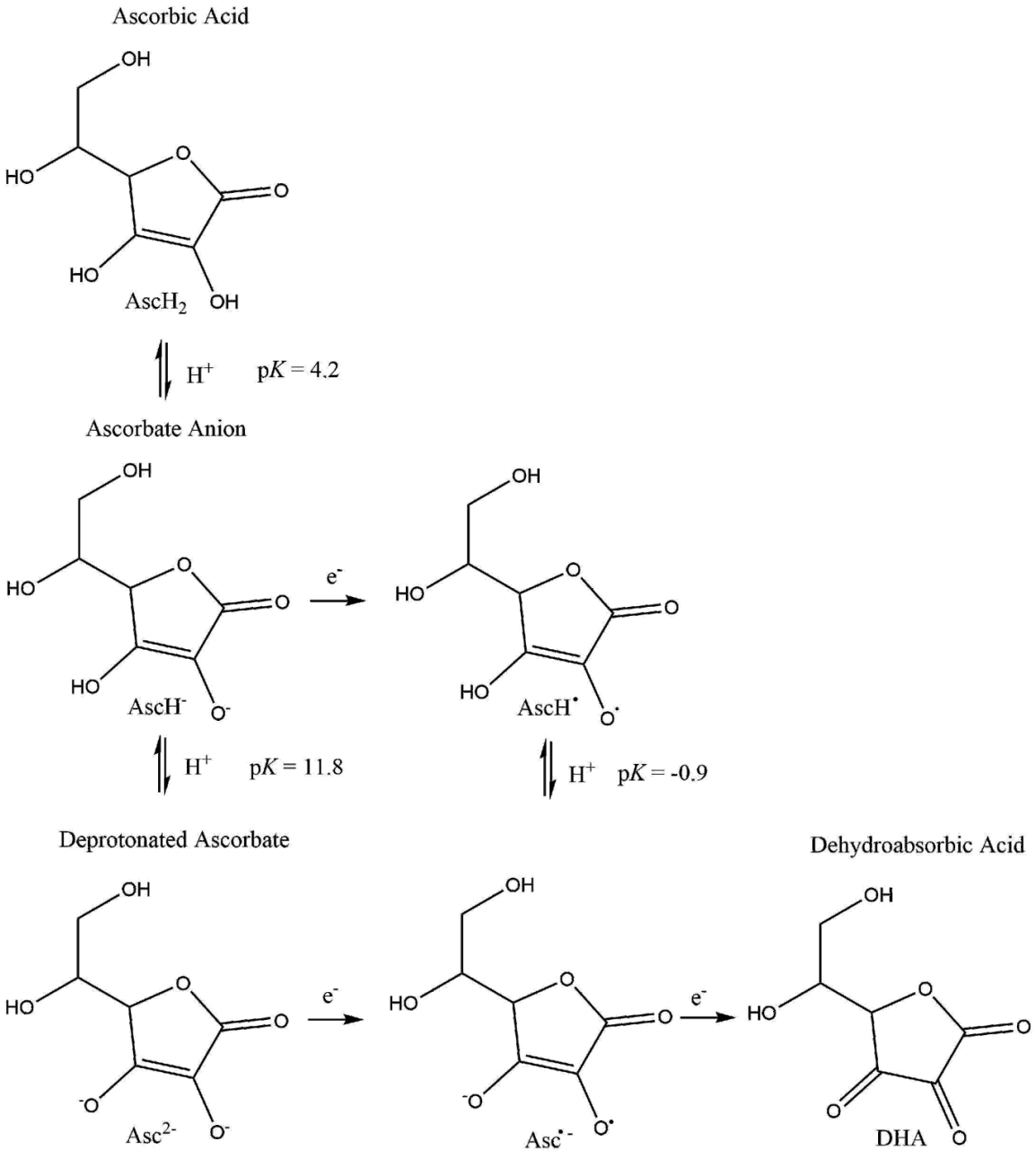

Figure V.1: Biologically relevant forms of ascorbic acid.

V.2. EXPERIMENTAL

Ascorbate and doubly deprotonated ascorbic acid (Asc^{2-}) were generated via electrospray ionization. Millimolar solutions of ascorbic acid in 3:1 ($MeOH:H_2O$) were prepared. This solution was then sprayed through a ~10 μm pulled silica capillary floated at negative 2 -

3 kilovolts into a humidity controlled ambient atmosphere. These ions then entered a stainless steel desolvation capillary heated to help desolvate the droplets formed via the ionization process. After exiting the capillary these ions were guided through differentially pumped chamber by ion guides to an ion trap. The ion trap is cooled by a LN_2 flow cryostat, cools the trap to a temperature of 77 K which is monitored via a silicon diode. A buffer gas of 20% H_2 in a balance of He to facilitate cooling of the ions.[6] Ions were then accumulated and cooled in the trap for 100 ms before being pulsed out of the trap into a time of flight mass spectrometer.

Anion photoelectron spectroscopy is conducted by crossing a mass-selected packet of negative ions with a fixed frequency photon beam and energy-analyzing the resultant photodetached electrons. These photoelectrons are governed by the energy-conserving relationship, $\nu = EBE + EKE$, where $h\nu$ is the photon energy, EBE is the electron binding energy, and EKE is the measured electron kinetic energy. The apparatus consists of a laser vaporization source, a time of flight mass spectrometer, momentum decelerator and an anion photoelectron spectrometer. The anion photoelectron spectrometer consists of an magnetic bottle electron energy analyzer and a Nd:YAG laser. The magnetic bottle has a resolution of 50 meV at an EKE of 1 ev. These spectra were collected with the 3rd and 4th harmonic of the Nd:YAG, 335 nm (3.49 eV) and 266 nm (4.66 eV) photons. The anion spectrometer was calibrated against the transitions of I^-. Photoelectron spectra were taken with the ion trap at room temperature as well as 77 K.

V.3. RESULTS

The mass spectrum from ESI of the ascorbic acid solution is shown in Figure V.1. The strongest peak in the spectrum is ascorbate or deprotonated ascorbic acid, annotated Asc-

H^-. Another species of interest seen in the mass spectrum is doubly deprotonated ascorbic acid denoted Asc^{2-}. By increasing the pH. the intensity of the doubly deprotonated peak can be increased. Additional peaks seen are likely fragments of AA or complexes of fragments, this may occur either during the ionization process or during transport through the ion guide system via collisions with background gas molecules.

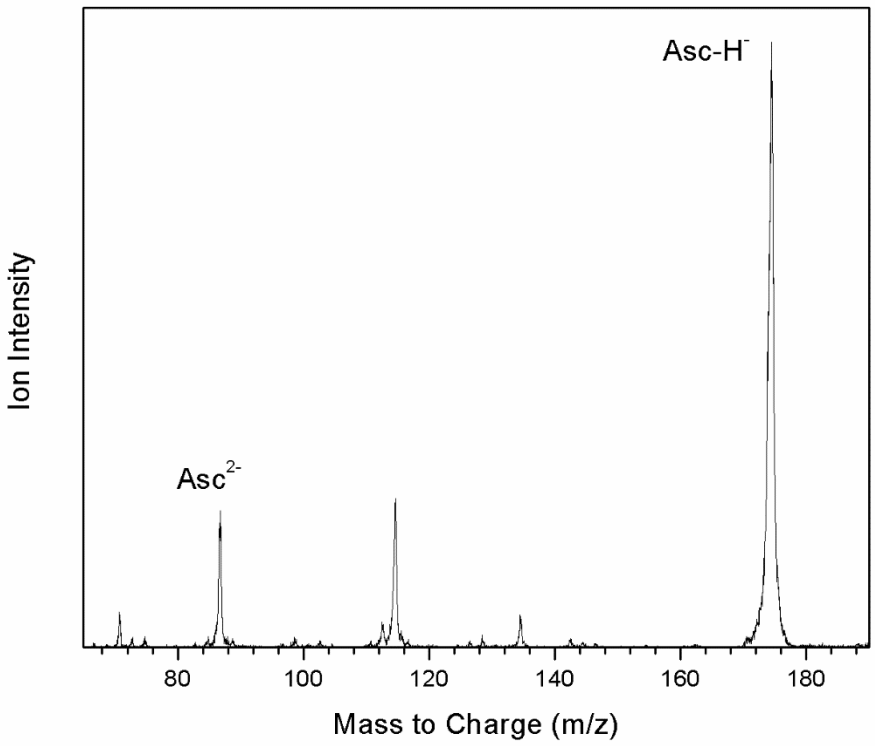

Figure V.2: Mass spectra of ascorbic acid solution generated by ESI.

Preliminary photoelectron spectra were taken of ascorbate ($AscH^-$) and dehydroascorbic acid (Asc^{2-}). The room temperature photoelectron spectra taken with the fourth harmonic of the YAG (4.66 eV) of ascorbate is shown in Figure V.3. From these preliminary

spectra the VDE of ascorbate is 3.9 eV. Since a photoelectron spectrum of cold ascorbate is unavailable, no electron affinity is reported.

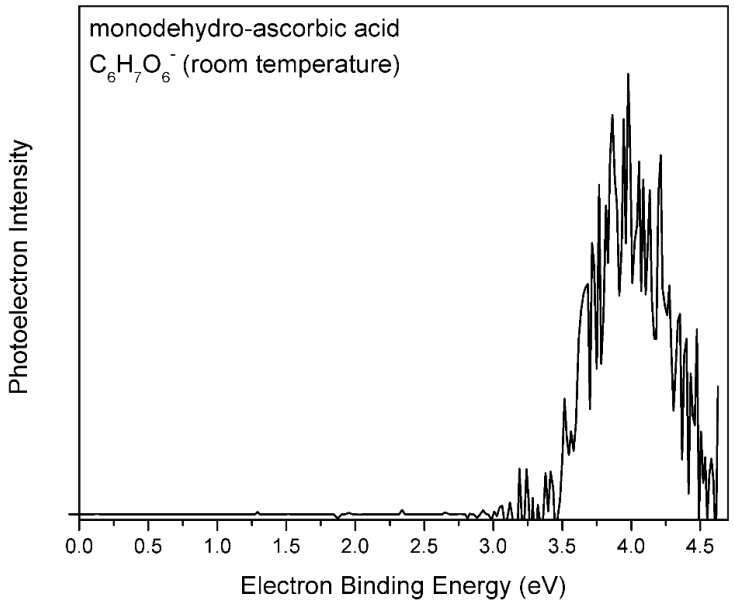

Figure V.3: Room temperature photoelectron spectra of ascorbate ($AscH^-$) taken with the fourth harmonic of the YAG (4.66 eV photon energy).

The preliminary photoelectron spectra of dehydroascorbic acid (Asc^{2-}) is presented in Figures V.4 & 5. These spectra were both taken with the third harmonic of the YAG (3.49 eV photon energy). The spectra in Figure VI.4 is with Asc^{2-} at room temperature and the spectra in Figure V.5 is taken while cooling the ions prior to photodetachment. Based on these two spectra, the VDE of Asc^{2-} is 2.75 eV. Upon cooling the resolution of the spectra slightly improves. Based on the cooled spectra, the onset for Asc^{2-} is 2.31 eV. In Figure V.6 the fourth harmonic (4.66 eV photon energy) spectra of Asc^{2-} is presented and higher binding energy spectral peaks are shown.

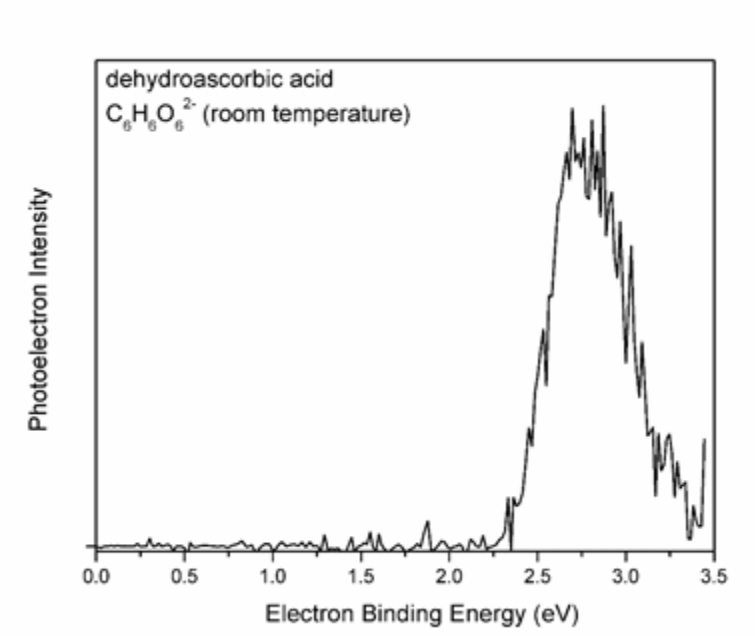

Figure V.4: Room temperature photoelectron spectra of dehydroascorbic acid (Asc^{2-}) taken with the third harmonic of the YAG (3.49 eV photon energy).

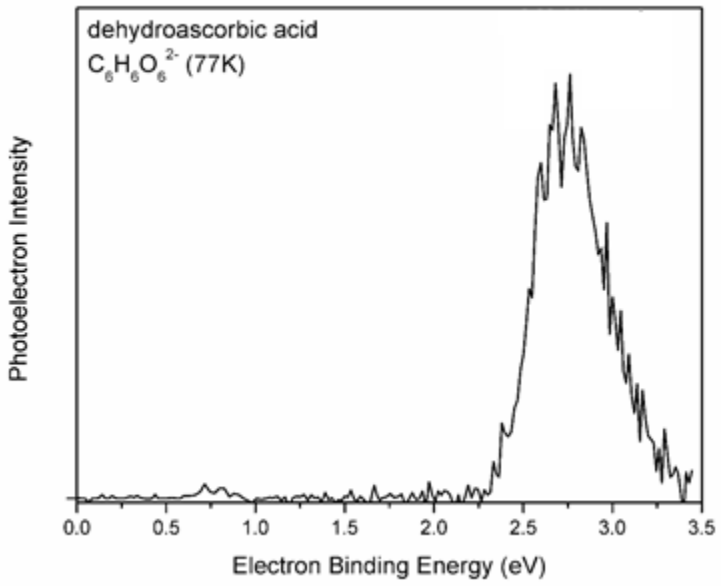

Figure V.5: Photoelectron spectra of cold (77K) dehydroascorbic acid (Asc^{2-}) taken with the third harmonic of the YAG (3.49 eV photon energy).

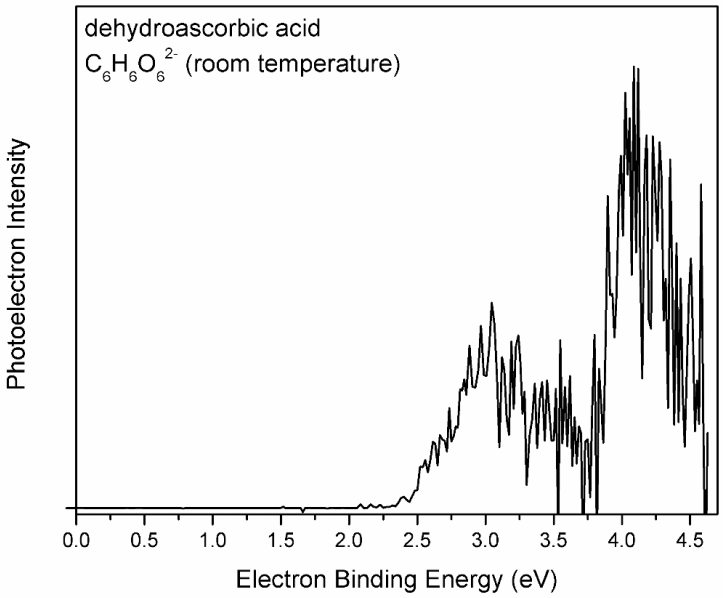

Figure V.6: Room temperature photoelectron spectra of dehydroascorbic acid (Asc^{2-}) taken with the fourth harmonic of the YAG (4.66 eV photon energy).

V.4. DISCUSSION

In order to further interpret these spectra, cooled spectra should be taken for both species with the 4th harmonic of the YAG. In addition, it would be interesting to see how water solvation affects the photoelectron spectra. Theoretical calculations for these spectra would allow for structures of the species to be elucidated. If further studies with water solvation were undertaken, it would show how these radicals were solvated.

References

1. Winterbourn, C. C. *Nat. Chem. Biol.* **4**.5 (2008): 278.

2. Nimse, S. B., and Pal, D. *RSC Adv.* **5**.35 (2015): 27986-8006.

3. Anstöter, C. S., West, C. W., Bull, J. N., and Verlet, J. R. *J. Phys. Chem. B* **120**.29 (2016): 7108-13.

4. Buettner, G. R., Schafer. "Ascorbate as an antioxidant" *Vitamin C: Function and biochemistry in animals and plants*, edited by Han Asard, et al., BIOS Scientific Publishers, 2004, pp. 173-88.

5. Du, J., Cullen, J. J., and Buettner, G. R. *Biochim. Biophys. Acta* **1826**.2 (2012): 443-57.

6. Wang, X.-B., and Wang, L.-S. J. *Rev. Sci. Instrum.* **79**.7 (2008): 073108.

Chapter VI : APPENDIX

VI.1. ION TRAP PULSING AND ELECTRONICS

The ion trap is operated by three separate electronics boxes. The ion trap RF power supply controls the RF waveform applied to the ion trap. From the front panel of the power supply one can control the peak to peak voltage of this RF waveform. This power supply has a lot of advanced features, however none of them are typically used. The ion trap is operated in “manual” mode. Meaning that the box simply provides the 1 MHZ rf to the center electrode of the trap and once sent a TTL pulse clamps that RF, attenuating that to zero This power supply should only be energized when the RF cable is connected to the ion trap. The ion trap and cable are part of the circuit. If the power supply is energized while disconnected it can be damaged.

There is a separate set of boxes that control the extraction pulses which eject ions from the trap. One of these boxes is a pulser box pictured below in Figure VI.1, and the second box supplies the previous box with 24 V, 5 V, and the TTL box via a DB-15 cable. The pulser box is a (DEI Model: PVM-4210) and produces two pulses, one positive and one negative, independently adjustable from 0 to +/-1000 V. Inside the pulser box there are two variable potentiometers that control the pulse voltage. These can be adjusted with a flat head screwdriver. One should be careful while adjusting these as there is high voltage present on the board and inside the enclosure. For negative ions, a extraction pulse of -50 V on the input endcap and a pulse of +20 V on the output endcap is used. For positive mode the voltages should be reversed with +50 V and -20 V on the input and output endcap respectively. By changing the width of the triggering pulse, the on time of the extraction pulse can be varied.

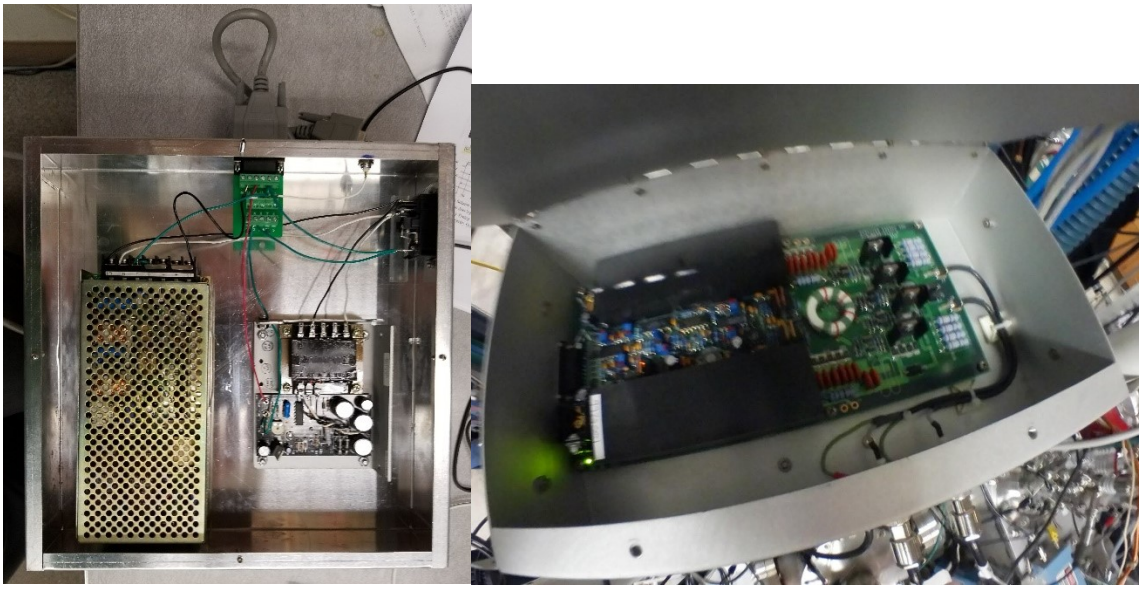

Figure VI.1: Power supply box for endcap pulser (Left). Endcap Pulser (Right).

VI.2. DRY SCROLL PUMP TO TURBO BACKED WET PUMP SWITCHOVER

Due to their orientation, with the high vacuum inlet facing down towards the chamber, the two turbo molecular pumps on Chamber 1 should be backed with a dry mechanical pump. These turbomolecular pumps on-top of Chamber 1 and the three turbos on the interaction region share a common foreline. Normally a small scroll pump (Varian IDP3) backs all five of these turbo molecular pumps. This backing pump is suitable for running any Chamber 0 source i.e. laser vaporization or the PACIS. However, when the buffer gas for the ion trap is added this small scroll pump is unable to keep up with the helium load and the foreline rises significantly. In order to keep both the foreline free of oil and increase the helium pumping speed, an additional rotary vane backed small turbomolecular pump has been added that can be switched over to when admitting buffer gas into the ion trap. A series of electrically actuated valves switches the turbo pumps from being backed by a dry scroll pump to being backed by the rotary vane backed turbo. Ideally a larger scroll pump capable of handling the helium gas load from the ion trap should be purchased. One should make sure to switch back to the scroll pump before leaving the instrument unattended.

VI.3. CRYOSTAT

The cryostat that holds the ion trap is a custom LT-4B liquid cryogen flow cryostat from Advanced Research Systems. At the bottom of the cryostat a custom copper flange has been added to mount the ion trap onto it. This flange also has a Lakeshore DT-670 silicon diode and a cartridge heater for temperature monitoring and control. The cryostat is mounted to a tilt adjuster allowing for it to be aligned in vacuum to compensate for contraction of the metal upon cooling. This assembly is then mounted to a cluster flange with several small ports for feedthroughs for various voltages and the buffer gas (Figure VI.2).

Figure VI.2: Pictures of the cryostat. Bare cryostat (Left), cryostat with ion trap and mount attached (Middle), assembled cryostat with heat shield (Right).

This system is currently set up for use with LN_2 and is fitted with a customized 15 liter LN_2 self-pressurizing dewar. The dewar and cryostat are connected via a transfer hose. The dewar and has been modified with additional pressure release valves from Advance Research Systems.

The system is operated by pressurizing the dewar, causing cryogen to flow from the dewar through the transfer line and into the cryostat to cool the copper base at the bottom. The flowrate of the LN_2 is controlled several ways. The pressure of the dewar can be regulated by the added check valves. The flow rate can also be regulated by a needle valve on the transfer line located on the end inserted into the cryostat. Additionally, the exhaust from both the transfer line as well as the cryostat is regulated through needle valves attached to flowmeters. It is critical to correctly regulate the flow of cryogen both for temperature control as well as operation of the vacuum system. If the flow is too high, it can freeze the exterior surface of the cryostat as well as the attached flanges and seals, potentially causing a vacuum leak.

For initial cool, down the dewar is pressurized to 10 P.S.I. and the needle valve in the transfer line is set to its fully open position, three turns after it starts threading onto the cryostat. The needle valves on the flow meters should also be set to be fully open. During this process, the temperature of the cryostat should be monitored via the silicon diode attached to the copper ion trap mount. In addition, the Chamber 1 pressure as well as visual confirmation that significant condensation of moisture onto the cryostat top is not occurring. When the temperature reaches 77K, the pressure of the dewar should be reduced to 2.5 P.S.I. The needle valve on the transfer hose should also be closed a few turns by rotating it clockwise. The needle valves on the flow meters should be reduced as

much as possible until the meters read a steady reading. Small adjustments to all of these flow control devices should be made to minimize the flow of LN_2 while maintaining the desired temperature. One should monitor the exterior of the cryostat periodically, as significant frosting of the exterior is a sign of too high an LN_2 flow rate.

The buffer gas used in the ion trap is a 20% H_2 mixture in an Helium balance. There is a separate gas manifold for handling this gas. The manifold is connected to the buffer gas cylinder through a regulator. There is also a vacuum pump, vent valve and shutoff vale the buffer gas flowing into the chamber. The flow of buffer gas into the chamber can be controlled via a combination of the pressure on the regulator for the mixture and through a leak valve. One should be careful not to pump directly on the mixture with the vacuum pump as it contains a significant amount of hydrogen. When it is necessary to pump the manifold with the mechanical pump, the procedure is make sure the buffer gas tank is isolated from the manifold, vent the manifold, and then evacuate the manifold.

The temperature controller for the cryostat is proprietary controller board provided to us by the Instrument Development Group. This board can control a cartridge heater as well as read the temperature of a silicon diode attached to it. The board is controlled by a computer with a Labview program. Commands are sent to the hardware using an ethernet card and network switch mounted inside the controller box. To do this, a software program from Lantronix is used to assign the IP address of the controller to a communications port (COM port). Commands are then sent to the card through that COM port.

VI.4. GENERAL PRACTICES FOR MAKING ESI SOLUTIONS AND EMITTER TIPS

Solutions for the electrospray are generally prepared in the 1-10 mM range. In order to facilitate this there is both an analytical balance and 20 – 200 µl pipettor available for use. If a solution is too concentrated, it tends to clog the desolvation capillary quickly. In addition, highly concentrated solutions could contaminate this capillary causing the species to be seen in the background when running other samples necessitating cleaning of the block and desolvation chamber.

The solvent system should be chosen to ensure solubility of the compound and a consistent ionization signal from the electrospray needle. Both methanol:water in 3:1 mixture by volume and pure acetonitrile work well for a range of species. Solvents should also be relatively pure as contaminants could be seen in the mass spectra.

The syringe for the ESI needle setup is a Hamilton 2.5 mL syringe with an 22 ga. needle. Onto this a Microtight union with a pulled silica needle mounted in it is attached. These needles are made by pulling peek covered 250 µm O.D. silica tubing under a butane torch and are then opened by cutting the end with a razor blade. The needle is then mounted in a syringe pump and the high-voltage lead attached to the metal needle. Generally a flow rate of 3 µl/minute has worked well.

VI.5. ESI STAND AND OPENING CHAMBERS

The ESI stand allows for the movement of the chambers that house the ion guides. As the ion guides are the length of the chamber, the chambers must be movable to access all of them. These chambers are mounted on Teflon bearings placed on a rail of extruded aluminum which allows the chambers to slide. One should do this with care and grab both sides of carriage the bearings are mounted on to.

To move these chambers, one must clear any obstructions from the rails allowing a clear path for the chambers to slide. The vacuum and electrical connections from the desolvation chamber should be disconnected. The bellows attaching the roots blower to the first quad chamber should be disconnected by detaching the flange connected to the Roots blower. The power supplies for the turbo molecular pumps on the second quadrupole chamber and the 90° bender chamber should be turned off by their ac power switch and the power connection and communication cable to the turbo disconnected. The RF power supplies should also be turned off and disconnected for safety reasons.

Care should be taken when separating the second quad chamber from the 90° bender chamber. The flange which holds both the second quadrupole and the 1st octopole is sandwiched between these two chambers and care should be taken to ensure it doesn't fall in the process of moving the 2nd quad chamber.

When moving the chambers, one should move the carriages that support the yolks holding the chambers evenly to prevent them from jamming. The chambers should move fairly smoothly. If one of the chambers is difficult to slide, one should inspect and ensure

none of the cables have become caught and that the moving chamber isn't impinging on another object.

I would not recommend removing or unbolting the flange holding the 90° bender as that would necessitate realignment as it is mounted on a rotatable Conflat flange. I would recommend parting the chambers connected to the 6-way cross chamber that houses the 90° as shown in the Figures VI.4 and VI.5. Some of the adapters bolted to this chamber are mounted on rotatable Conflat flanges. While tightly bolted they will not rotate, however if removed or loosened, they will rotate. Their alignment can be arduous and time consuming and in almost all cases can be avoided.

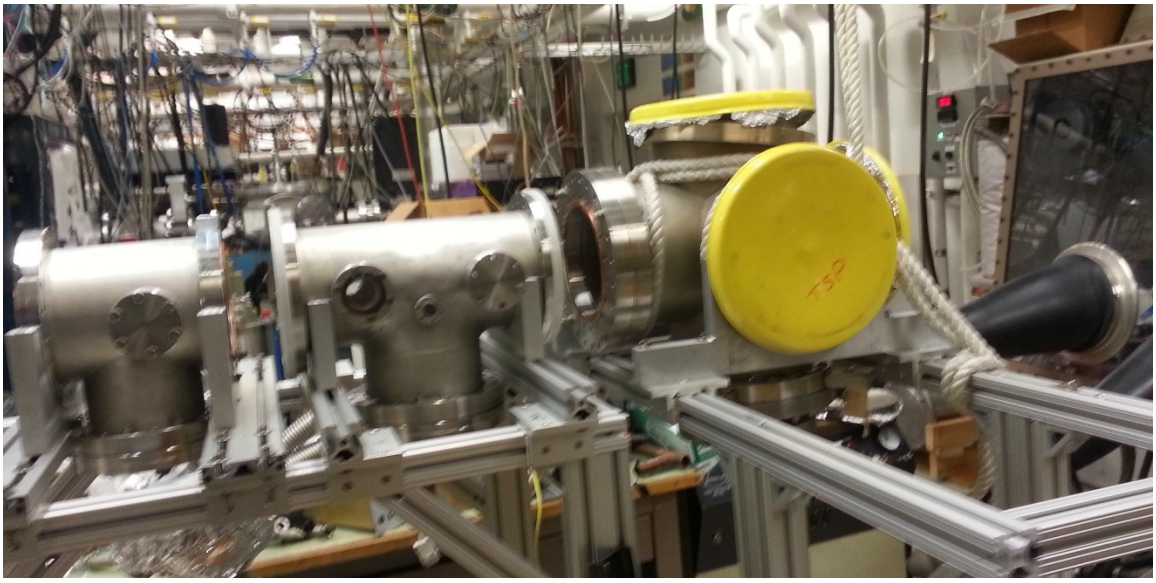

Figure VI.3: ESI stand with the three movable chambers mounted.

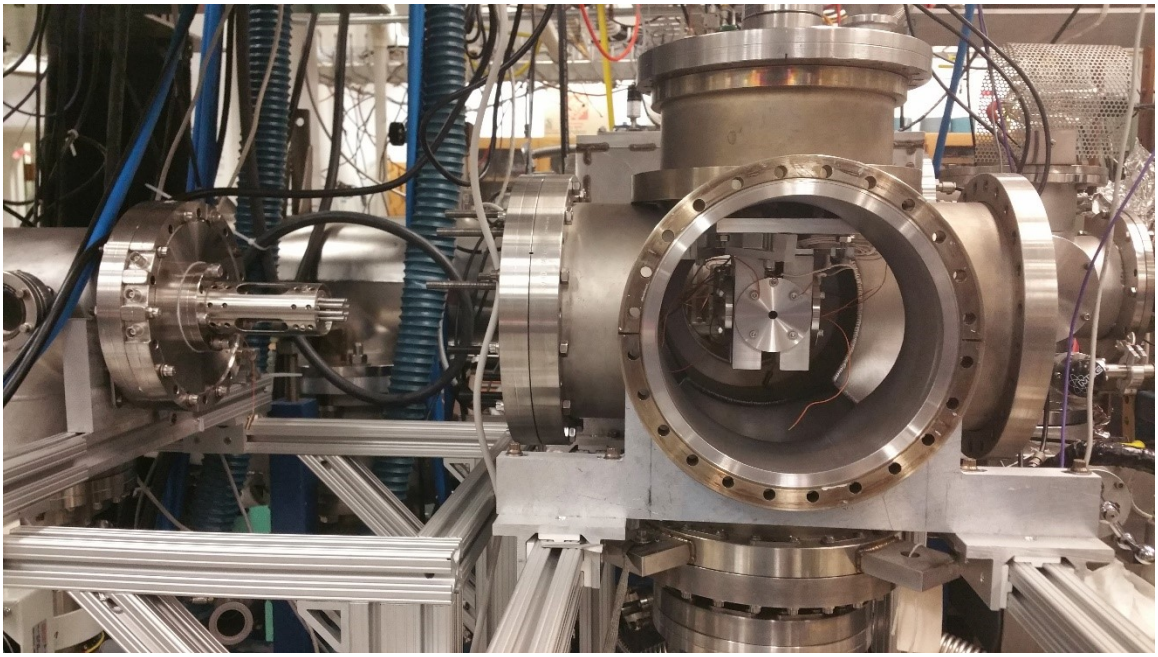

Figure VI.4: Front view of 90° bender chamber on ESI source with chambers separated.

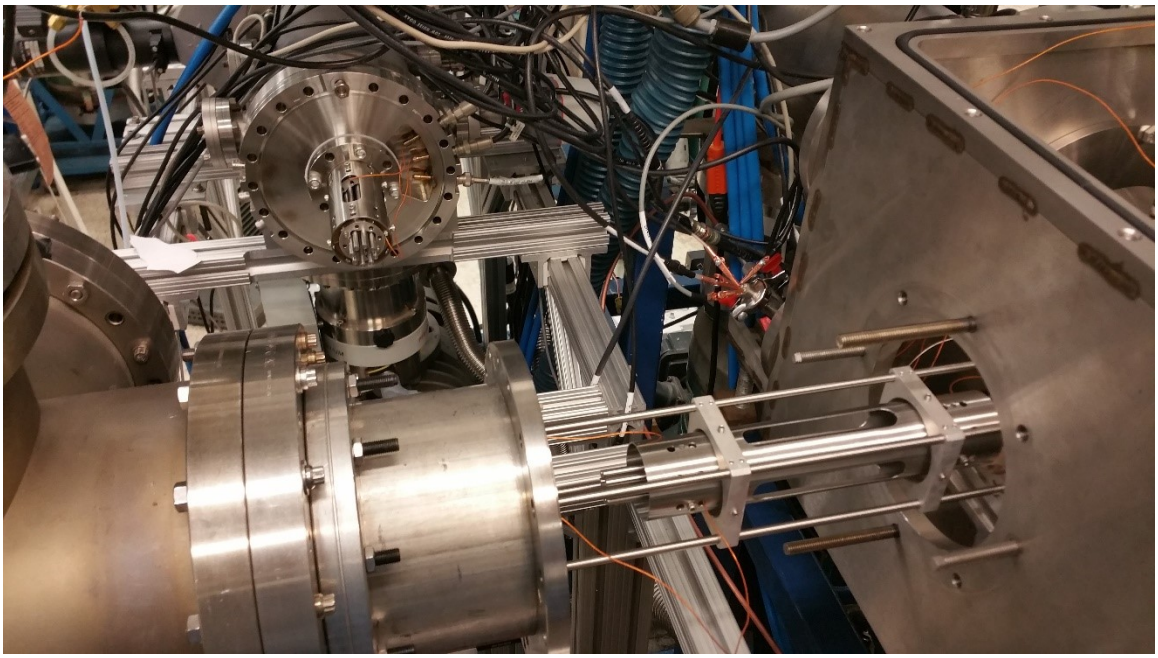

Figure VI.5: Back view of 90° bender chamber on ESI source with chambers separated.

Evan L. Collins

Evan.Collins@jhu.edu • 410-937-1245
727 W 40th Street Apt. 591, Baltimore, MD 21211

EXPERIMENTAL PHYSICAL CHEMIST

EDUCATION

Doctor of Philosophy Chemistry – The Johns Hopkins University (Baltimore, MD) January 2019
Master of Arts Chemistry – The Johns Hopkins University May 2014
Bachelor of Arts Chemical Engineering – The Johns Hopkins University May 2011
Bachelor of Arts Chemistry – Goucher College (Towson, MD) August 2010

RESEARCH EXPERIENCE

Johns Hopkins University-Department of Chemistry, Baltimore, MD August 2011 – January 2019
Graduate Research Assistant (Adviser: Prof. Kit H. Bowen)

- Interrogated properties of metal hydrides, metal clusters, Rydberg anions, and phenomena such as intra-molecular electron induced proton transfer in organic molecules using anion photoelectron spectroscopy and gas phase mass spectrometry.
- Designed and constructed a home-built electrospray ionization source (ESI) and differentially pumped ion guide system, coupled with a temperature controlled cryogenic ion trap. Integrated this source with a time-of-flight mass spectrometer and anion photoelectron spectrometer.

Army Research Laboratory – SEDD, Adelphi, MD June 2009 – August 2011
Research Assistant (Adviser: Jeffrey Read Ph.D.)

- Investigated lithium fluoride (LiF) formation in the cathodes of discharged Lithium Carbon monofluoride (Li/CFX) batteries via powder x-ray diffraction and scanning electron microscopy (SEM), correlated the effect with cathode swelling, and developed a model for LiF formation.

Goucher College – Department of Chemistry, Towson, MD June 2007 – June 2009
Undergraduate Research Assistant (Adviser: Prof. Scott Sibley)

- Used bovine insulin as a model for protein aggregation to mimic beta-amyloid plaque production.
- Studied the effect of the addition of small molecule inhibitors on protein aggregate production via time course UV/VIS Absorption spectroscopy, Attenuated Total Reflectance (ATR) infrared spectroscopy, and imaged resultant aggregate with atomic force microscopy (AFM).

TEACHING EXPERIENCE

The Johns Hopkins University August 2011 - May 2015
Teaching Assistant

- Introductory Chemistry Lecture
- Thermodynamics with Biophysical Applications Lecture
- Physical Chemistry I & II Laboratory

Goucher College August 2010 - Dec 2010
Adjunct Professor – General Chemistry Lab

- Supervised a section of 15 undergraduates, thorough laboratory experiments.
- Graded homework, quizzes and tests.

MENTORING EXPERIENCE

Graduate Student Mentor

- JHU Undergraduate in Bowen laboratory
  August 2015 – August 2018
- High school senior, Hopkins Extreme Materials Institute (HEMI)
  June 2017 – August 2017 Army Educational Outreach Program (AEOP) Student in Bowen laboratory
- High school senior from Baltimore Polytechnic Institute, in Bowen laboratory
  September 2014 – August 2016
- JHU Undergraduate in Bowen laboratory
  August 2012 – May 2014

SOFTWARE SKILLS

SolidWorks ● LabVIEW ● AutoCad Inventor ● Mathematica ● R ● SIMION ● Origin ● Gaussian

AWARDS

Mary Lydston Kilpatrick Fellowship - Department of Chemistry, The Johns Hopkins University
2016
Three month support plus a $1000 stipend supplement to be awarded to an outstanding advanced-year graduate student.

American Chemical Society Student Award - Maryland Section of the American Chemical Society
2009
Most Outstanding Undergraduate Chemistry Student at Goucher College.

CONFERENCE POSTERS

Posters

- 2016 Gordon Research Conference: Molecular & Ionic Clusters, Ventura, Ca, Jan 2016: "*Electron Induced Proton Transfer in the Anion of Acetoacetic Acid*"
- 2016 Gordon Research Seminar: Molecular & Ionic Clusters, Ventura, Ca, Jan 2016: "*Electron Induced Proton Transfer in the Anion of Acetoacetic Acid*"
- DTRA Technical Review, Springfield, Va, July 2013: *"Next Generation Energetic Materials: New Cluster Hydrides and Metastable Alloys of Aluminum in Very Low Oxidation States"*

PUBLICATIONS

7. "On the Importance of Time Scale and Local Environment in Electron-Driven Proton Transfer. The Anion of Acetoacetic Acid " Z. G. Keolopile, M. Gutowski, A. Buonaugurio, E. Collins, X. Zhang, J. Erb, T. Lectka, K. Bowen, and M. Allan, J. Am. Chem. Soc., 137, 14329–14340 (2015).

6. "The Alanate Anion, AlH4-: Photoelectron Spectrum and Computations", J.D. Graham, A. M. Buytendyk, X. Zhang, E. L. Collins, K. Boggavarapu, G. Gantefoer, B. W. Eichhorn, G. L. Gutsev, S. Behera, P. Jena, and K. H. Bowen, J. Phys. Chem. A, 118, 8158–8162 (2014)

5. "Photoelectron Spectra of the MgH− and MgD− Anions", A. Buytendyk, J. Graham, H. Wang, X. Zhang, E. Collins, Y. J. Ko, G. Gantefoer, B. Eichhorn, A. Regmi, K. Boggavarapu, K. H. Bowen, Int. J. of Mass Spectrom., 365-366, 140-142(2014)

4. In Search of Four-Atom Chiral Metal Clusters ", X. Zhang, B. Visser, M. Tschurl, E. Collins, Y. Wang, Q. Wang, Y. Li, Q. Sun, P. Jena, G. Gantefoer, U. Boesl, U. Heiz, and K. H. Bowen, J. Chem. Phys. 139, 111101 (2013)

3. “Negative ions of p-nitroaniline: Photodetachment, collisions, and ab initio calculations ", B. H. Smith, A. Buonaugurio, J. Chen, E. Collins, K. H. Bowen, R. N. Compton and T. Sommerfeld, J. Chem. Phys. 138, 234304 (2013)

2. “Photoelectron spectroscopy of the aluminum hydride anions: AlH2-, AlH3−, Al2H6−, Al3H9−, and Al4H12− ", X. Zhang, H. Wang, E. Collins, A. Lim, G. Ganteför, B. Kiran, H.Schnöckel, B. Eichhorn, and K.H. Bowen , J. Chem. Phys. 138, 124303 (2013)

1. "LiF Formation and Cathode Swelling in the Li/CFx Battery", J. Read, E. Collins, B. Piekarski, and S. Zhang, J. Electrochem. Soc., 158, A504 (2011)